Changes of air pollutant emissions in China during two clean air action periods derived from the newly developed Inversed Emission Inventory for Chinese Air Quality (CAQIEI)

Lei Kong[1,3], Xiao Tang[*,1,3], Zifa Wang[*,1,3,4], Jiang Zhu[1,2], Jianjun Li[5], Huangjian Wu[1,3], Qizhong Wu[6], Huansheng Chen[1,3], Lili Zhu[5], Wei Wang[5], Bing Liu[5], Qian Wang[7], Duohong Chen[8], Yuepeng Pan[1,3], Jie Li[1,3], Lin Wu[1,3], and Gregory R. Carmichael[9]

[1]State Key Laboratory of Atmospheric Boundary Layer Physics and Atmospheric Chemistry (LAPC), Institute of Atmospheric Physics, Chinese Academy of Sciences, Beijing 100029, China
[2]CAS-TWAS Center of Excellence for Climate and Environment Sciences (ICCES), Institute of Atmospheric Physics, Chinese Academy of Sciences, Beijing 100029, China
[3]College of Earth and Planetary Sciences, University of Chinese Academy of Sciences, Beijing 100049, China
[4]Center for Excellence in Regional Atmospheric Environment, Institute of Urban Environment, Chinese Academy of Sciences, Xiamen 361021, China
[5]China National Environmental Monitoring Centre, Beijing, 100012, China
[6] College of Global Change and Earth System Science, Faculty of Geographical Science, Beijing Normal University, Beijing 100875, China
[7]Shanghai Environmental Monitoring Centre, Shanghai, 200030, China
[8]Guangdong Ecological Environment Monitoring Centre, National Key Laboratory of Regional Air Quality Monitoring for Environmental Protection, Guangzhou 510308, China
[9]Center for Global and Regional Environmental Research, University of Iowa, Iowa City, IA 52242, USA

Correspondence to: Xiao Tang (tangxiao@mail.iap.ac.cn) and Zifa Wang (zifawang@mail.iap.ac.cn)

Abstract

A new long-term emission inventory called the Inversed Emission Inventory for Chinese Air Quality (CAQIEI) was developed in this study by assimilating surface observations from the China National Environmental Monitoring Centre (CNEMC) using the ensemble Kalman filter and the Nested Air Quality Prediction Modeling System. This inventory contains the constrained monthly emissions of NO_x, SO_2, CO, primary $PM_{2.5}$, primary PM_{10}, and NMVOCs in China from 2013 to 2020, with a horizontal resolution of 15 km × 15 km. This paper documents detailed descriptions of the assimilation system and the evaluation results for the emission inventory. The results suggest that CAQIEI can effectively reduce the biases in the *a priori* emission inventory, with the normalized mean biases ranging from −9.1% to 9.5% in the *a posteriori* simulation, which are significantly reduced from the biases in the *a priori* simulations (−45.6% to 93.8%). The calculated RMSEs (0.3 mg/m^3 for CO and 9.4–21.1 μg/m^3 for other species, on the monthly scale) and correlation coefficients (0.76–0.94) were also improved from the *a priori* simulations, demonstrating good performance of the data assimilation system. Based on CAQIEI, we estimated China's total emissions (including both natural and anthropogenic emissions) of the 6 species in 2015 to be as follows: 25.2 Tg of NO_x, 17.8 Tg of SO_2, 465.4 Tg of CO, 15.0 Tg of $PM_{2.5}$, 40.1 Tg of PM_{10}, and 46.0 Tg of NMVOCs. From 2015 to 2020, the total emissions reduced by 54.1% for SO_2, 44.4% for $PM_{2.5}$, 33.6% for PM_{10}, 35.7% for CO, and 15.1% for NO_x, but increased by 21.0% for NMVOCs. It is also estimated that the emission reductions were larger during 2018–2020 (from -26.6% to -4.5%) than during 2015–2017 (from -23.8% to 27.6%) for most species. Particularly, the total Chinese NO_x and NMVOC emissions were shown to increase during 2015–2017, especially over the Fenwei Plain area (FW) where the emissions of particulate matter (PM) also increased. The situation changed during 2018–2020 when the upward trends were contained and reversed to downward trends for both the total emissions of NO_x and NMVOC, and the PM emissions over FW. This suggests that the emission control policies may be improved in 2018–2020 action plan. We also compared the CAQIEI with other air pollutant emission inventories in China, which verified our inversion results in terms of total emissions of NO_x, SO_2 and NMVOCs, and more importantly identified the potential uncertainties in current emission inventories. Firstly, the CAQIEI suggested higher CO emissions in China, with CO emissions estimated by CAQIEI (426.8 Tg) being more than

45 twice the amount in previous inventories (120.7–237.7 Tg). Significantly higher emissions were also suggested over the

46 western and northeastern China for other air pollutants. Secondly, the CAQIEI suggested higher NMVOC emissions than

47 previous emission inventories by about 30.4–81.4% over the North China Plain (NCP) region but suggested lower NMVOC

48 emissions by about 27.6–0.0% over the Southeast China (SE) region. Thirdly, the CAQIEI suggested smaller emission

49 reduction rates during 2015–2018 than previous emission inventories for most species except of CO. Particularly, China's

50 NMVOC emissions were shown to have increased by 26.6% from 2015 to 2018, especially over the NCP (by 38.0%), northeast

51 China (by 38.3%), and central China (60.0%). These results provide us with new insight into the complex variations of the air

52 pollutant emissions in China during its two recent clean air actions, which has the potential to improve our understanding of

53 air pollutant emissions in China and their impacts on air quality. The whole datasets are available at

54 https://doi.org/10.57760/sciencedb.13151 (Kong et al., 2023).

1 Introduction

56   Air pollution is a serious environmental issue owing to its substantial impacts on human health, ecosystems, and climate

57 change (Von Schneidemesser et al., 2015; Cohen et al., 2017; Bobbink et al., 1998). According to the World Health

58 Organization, air pollution–induced strokes, lung cancer, and heart disease are causing millions of premature deaths worldwide

59 every year (WHO, 2016). The fine particulate matter ($PM_{2.5}$) in the atmosphere not only degrades visibility but also affects the

60 radiative forcing of the climate, both directly and indirectly (Martin et al., 2004). After removal from the atmosphere through

61 dry and wet deposition, air pollutants such as sulfur, nitrate, and ammonium contribute significantly to soil acidification,

62 eutrophication, and even biodiversity reduction (Krupa, 2003; Hernández et al., 2016).

63   China has experienced severe $PM_{2.5}$ pollution in recent decades, due to its large emissions of air pollutants associated

64 with rapid urbanization and high consumption of fossil fuels (Kan et al., 2012; Song et al., 2017). The annual concentrations

65 of $PM_{2.5}$ in 2013 reached 106, 67 and 47 $\mu g/m^3$ over the Beijing–Tianjin–Heibei, Yangtze River Delta, and Peral River Delta

66 region, respectively, which were all higher than China's national standard (35 $\mu g/m^3$), and 5–10 times higher than that of the

67 World Health Organization (10 $\mu g/m^3$). To tackle this problem, strict emission control policies (so-called "clean air action

68 plans") have been proposed by China's government, including the "Action Plan on the Prevention and Control of Air Pollution"

69 from 2013 to 2017 (hereinafter called the "2013–2017 action plan"), and the "Three-year Action Plan for Winning the Bule

70 Sky War" from 2018–2020 (hereinafter called the "2018–2020 action plan"). With the successful implementation of these two

71 action plans, the air quality was substantially improved in China, as evidenced in both observational and reanalysis datasets

72 (Li et al., 2020b; Zheng et al., 2017; Krotkov et al., 2016; Zhong et al., 2021; Li et al., 2017a; Kong et al., 2021). However,

73 with the deepening of air pollution control, unexpected changes have occurred in China, bringing about new challenges for the

74 mitigation of air pollution in the future. On the one hand, despite a significant decline in $PM_{2.5}$ concentrations in China, severe

75 haze still occasionally occurs during the wintertime (Zhou et al., 2022b; Li et al., 2017c). In addition, field measurements in

76 cities over different regions of China consistently show different responses of aerosol chemical compositions to the emission

77 control policies (Tang et al., 2021; Zhou et al., 2019; Wang et al., 2022; Zhang et al., 2020; Li et al., 2019a; Xu et al., 2019b;

78 Lei et al., 2021; Zhou et al., 2022a). Compared with other aerosol species that showed substantial decreases during the clean

79 air action plans, nitrate has shown a weaker response to the control measures, remaining at high levels and in some cases

80 having even increased slightly. As a result, nitrate is playing an increasingly important role in heavy haze episodes in winter,

81 and dominates the chemical composition of $PM_{2.5}$ (Fu et al., 2020; Xu et al., 2019a), leading to a rapid transition from sulphate-

82 to nitrate-driven aerosol pollution (Li et al., 2019a; Wang et al., 2019b). On the other hand, photochemical pollution has

83 deteriorated in China, with ozone (O_3) concentrations having increased substantially in eastern China during 2013–2017 (Li et

84 al., 2019b; Lu et al., 2018; Lu et al., 2020; Wang et al., 2020b).

85   These unexpected changes have raised considerable concern among the scientific community and policymakers regarding

86   the overall effects of the clean air action plans, and how to coordinate the control of $PM_{2.5}$ and O_3 pollution. Addressing this

87   problem requires a comprehensive understanding of the effects of the clean air action plans on the emissions of different air

88   pollutantschemical species. In this respect, previous studies have compiled several long-term air pollutant emission inventories

89   in China using the bottom-up approach – for example, the Multi-resolution Emission Inventory for China (MEIC) developed

90   by Tsinghua University for 2010–2020 (Zheng et al., 2018); the Air Benefit and Cost and Attainment Assessment System-

91   Emission Inventory version 2.0 (ABaCAS-EI v2.0) developed by Tsinghua University for 2005–2021 (Li et al., 2023); the

92   Regional Emission Inventory in Asia (REAS) for 1950–2015 developed by Kurokawa and Ohara (2020); the Emissions

93   Database for Global Atmospheric Research (EDGAR) for 1970–2018 developed by Jalkanen et al. (2012); the Hemispheric

94   Transport of Air Pollution (HTAP) Inventory for 2000–2018 developed by Crippa et al. (2023); and the Community Emissions

95   Data System (CEDS) Inventory for 1970–2019 developed by Mcduffie et al. (2020). These emission inventories have provided

96   the community with important insights into the long-term changes in the air pollutant emissions of different air pollutants in

97   China, thus playing an indispensable role in our understanding of the effects of the country's clean air action plans on emissions

98   and air quality. However, due to the lack of accurate activity data and emission factors, bottom-up emission inventories are

99   subject to large uncertainties, particularly during the clean air action periods when the activity data and emission factors

100   changed considerably and were difficult to track. Consequently, the estimated emission rates from different bottom-up

101   emission inventories could differ by more than a factor of 2 (Elguindi et al., 2020). For example, the estimated emissions for

102   the year 2010 from different bottom-up inventories were 104.9–194.5 Tg for carbon monoxide (CO), 15.6–25.4 Tg for nitrogen

103   oxides (NO_x), 22.9–27.0 Tg for non-methane volatile organic compounds (NMVOCs), 15.7–35.5 Tg for sulfur dioxide (SO_2),

104   1.28–2.34 Tg for black carbon (BC), and 2.78–4.66 Tg for organic carbon (OC), reflecting the large uncertainty in current

105   bottom-up estimates of air pollutant emissions in China, which hinders the proper assessment of the effects of the clean air

106   action plans.

107   Inverse modeling of multiple air pollutant emissions (i.e., a top-down approach) provides an attractive way to constrain

108   bottom-up emissions by reducing the discrepancy between the model and observation through the use of data assimilation.

109   Numerous studies have confirmed the effectiveness of such a top-down method in verifying bottom-up emission estimates and

110   reducing their uncertainties (e.g., Elbern et al., 2007; Henze et al., 2009; Miyazaki and Eskes, 2013; Tang et al., 2013; Koohkan

111   et al., 2013; Koukouli et al., 2018; Jiang et al., 2017; Muller et al., 2018; Paulot et al., 2014; Qu et al., 2017. Based on long-

112   term satellite observations, the top-down method has also been used to track the long-term variations of emissions. For example,

113   Zheng et al. (2019) estimated the global emissions of CO for the period 2000–2017 based on a multi-species atmospheric

114   Bayesian inversion approach; Qu et al. (2019) constrained global SO_2 emissions for the period 2005–2017 by assimilating

115   satellite retrievals of SO_2 columns using a hybrid 4DVar/mass balance emission inversion method; by assimilating satellite

116   observations of multiple species, Miyazaki et al. (2020b) simultaneously estimated global emissions of CO, NO_x, and SO_2 for

117   the period 2005–2018; and, most recently, a regional top-down estimation of $PM_{2.5}$ emissions in China during 2016–2020 was

118   carried out by Peng et al. (2023) by assimilating surface observations. These studies provide us with valuable clues for

119   evaluating bottom-up emissions and improving our knowledge on the changes in emissions of different species in China during

120   the clean air action plans. However, most of these studies focused on emission trends at the global scale, which involved the

121   use of coarse model resolutions (>1°) that may be insufficient to capture the spatial variability of emission variations at the

122   regional scale. Meanwhile, current long-term, top-down estimates mainly focus on single species and do not fully cover the

123   two clean air action periods in China. Indeed, to date, there are still no long-term, top-down estimates of major air pollutant

124   emissions in China that fully cover the two clean air action periods.

125   In a previous study performed by our group, we developed a high-resolution air quality reanalysis dataset over China

126   (CAQRA) for the period 2013–2020 to track the air quality trends in China during the clean air action periods (Kong et al.,

127   2021). In the present study, as a follow up to this work, we constrained the long-term emission trends of major air pollutants

128 in China for 2013–2020 (which will be extended in the future on a yearly basis) by assimilating surface observations of air

129 pollutants from the China National Environmental Monitoring Centre (CNEMC) using an ensemble Kalman filter and the

130 Nested Air Quality Prediction and Forecasting System (NAQPMS). In the following sections, we present detailed descriptions

131 of the chemical data assimilation, the evaluation results of the inversed emission inventory, and the estimated emission trends

132 of different air pollutants in China during the clean air action periods.

2 The chemical data assimilation system

134 We used the chemical data assimilation system (ChemDAS) developed by the Institute of Atmospheric Physics, Chinese

135 Academy of Sciences, to constrain the long-term emission changetrends of different air pollutants in China, which was used

136 in the development of CAQRA in our previous work (Kong et al., 2021). Since the chemical transport model (CTM) and the

137 observations used in the top-down estimation were the same as those used in CAQRA, we only briefly describe these two

138 components in the following two subsections, instead concentrating on providing a fuller description (in the third subsection)

139 of the inversion scheme in ChemDAS.

2.1 Chemical transport model

141 The NAQPMS model was used as the forecast model to represent the atmospheric chemistry in this study, and the Weather

142 Research and Forecasting (WRF) model was used as the meteorological model to provide the meteorological input data.

143 NAQPMS contains comprehensive modules for the emission, diffusion, transportation, deposition, and chemistry processes in

144 the atmosphere, and has been used in previous inversion studies (Tang et al., 2013; Kong et al., 2019; Wu et al., 2020a; Kong

145 et al., 2023). Detailed configurations of the different modules used in NAQPMS are available in these publications.

146 Figure 1 shows the domain of the inverse model, which is the same as that used in CAQRA, with a fine-scale horizontal

147 resolution of 15 km. The HTAPv2.2 emission inventory was used as the a priori estimate of anthropogenic emissions in China,

148 which includes emissions from the energy, industry, transport, residential, agriculture, air and ship sectors with a base year of

149 2010 (Janssens-Maenhout et al., 2015). It is a harmonized global emission inventory that comprises of different regional

150 gridded inventories. Within the region of China, the air pollutant emissions were mainly provided by the MEIC emission

151 inventory (Janssens-Maenhout et al., 2015). The a priori estimates of emissions from other sourcesinventory includes the

152 anthropogenic emissions obtained from the HTAP v2.2 emission inventory that provides the emissions from energy, industry,

153 transport, residential, agriculture, air and ship sectors with a base year of 2010 (Janssens Maenhout et al., 2015); biogenic

154 emissions obtained from the Monitoring Atmospheric Composition and Climate (MACC) project (Sindelarova et al., 2014);

155 biomass burning emissions obtained from the Global Fire Emissions Database (GFED), version 4 (Van Der Werf et al., 2010;

156 Randerson et al., 2017); soil and lightning NO_x emissions obtained from Yan et al. (2003) and Price et al. (1997); and marine

157 volatile organic compound emissions obtained from the POET database (Granier et al., 2005). The dust emissions were

158 calculated online in NAQPMS as a function of the relative humidity, frictional velocity, mineral particle size distribution, and

159 the surface roughness (Li et al., 2012), while the sea salt emissions were calculated using the scheme of Athanasopoulou et al.

160 (2008). Note that since we aimed to estimate the air pollutant emissions and their changes from the surface observation, we

161 did not consider the temporal variation in the a priori emission inventory., This would ensure that so that the top-down

162 estimated emission trends were only derived from the surface observations, without being influenced by the trends in the prior

163 emission inventory. In this way, our top-down estimation can serve as an independent estimation of the air pollutant emission

164 changes in China. MeanwhileIn addition, we used the constant diurnal variation of the emissions in this study due to the lack

165 of information on the diurnal variation of the emissions from different sectors, which is a potential limitation in our current

166 work. However, since the emission inversion was performed on the daily basis (Sect. 2.3.3), the diurnal variations of the

167 emission may not significantly influence the simulation results of the daily mean concentrations of air pollutants (less than 1

168 ppbv for SO$_2$, NO$_2$ and O$_3$) according to the sensitivity experiments conducted by Wang et al. (2010). The initial condition

169 was treated as clean air in NAQPMS, with a 2-week spin-up time. Top and boundary conditions were provided by the Model

170 for Ozone and Related Chemical Tracers (MOZART) (Brasseur et al., 1998; Hauglustaine et al., 1998) data products provided

171 by National Center for Atmospheric Research (NCAR). Note that since the MOZART data products were not available for

172 years after 2018, the multi-year average results from 2013 to 2017 were used for the simulations after 2018. Because most of

173 the model boundaries were set in the clean areas and are located at distance from China, we assumed that the differences in

174 boundary conditions would not significantly affect the modeling results over the China. To improve the performance of

175 meteorological simulation, a 36-h free run of the WRF model was conducted for each day by using the NCAR/NCEP 1°×1°

176 reanalysis data. The simulation results of the first 12 h were treated as the spin-up run, and the remaining 24 h were used to

177 provide the meteorological inputs for the NAQPMS model. The evaluation results for the WRF simulation are available in

178 Text S1 in the Supplement, which suggests acceptable performance of the WRF simulation for the inversion estimates (Table

179 S1).

2.2 Assimilated observations

181   The assimilated observational dataset in this study was the same as that used in CAQRA, which includes surface

182 concentrations of PM$_{2.5}$, PM$_{10}$ (coarse particulate matter), SO$_2$, NO$_2$ (nitrogen dioxide), CO, and O$_3$, from 2013 to 2020,

183 obtained from CNEMC (Fig. 1). Before the assimilation, outliers of the observations were filtered out by using an automatic

184 quality control method developed by Wu et al. (2018). Four types of outliers characterized by temporal and spatial

185 inconsistencies, instrument-induced low variances, periodic calibration exceptions, and lower PM$_{10}$ concentrations than those

186 of PM$_{2.5}$, were filtered out to prevent adverse impacts on the inversion process. As estimated in Kong et al. (2021), about 1.5%

187 of observational data were filtered out after quality control, but further assessment showed that it had few effects on the average

188 concentrations of different species, which were estimated to be less than 1 μg/m^3 for the gaseous air pollutants and less than

189 5 μg/m^3 for the particulate matter. Estimation of observation error is also important for~~to~~ the inversion of emissions since the

190 observational error and background errors determine the degree of adjustment to the emissions. The observational error

191 comprises the measurement error and the representativeness error induced by the different spatial scales that the model and

192 observations represent. The estimations of these two components of observational error were the same as those used in CAQRA,

193 detailed descriptions of which are available in Kong et al. (2021).

194   It should be noted that the number of observation sites were not constant throughout the whole inversion period, being

195 approximately 510 in 2013 and then increasing to 1436 in 2015. According to Fig. S1, the observation sites were mainly

196 concentrated in the megacity clusters ~~in China~~ (e.g., North China Plain, Yangtze River Delta and Pearl River Delta) and the

197 capital cities of each province in 2013. The number of observation sites continued to increase across the China in 2014 and

198 2015. In particular, many areas that were previously unobserved ~~in 2013~~ have added monitoring stations in 2014 and 2015,

199 which significantly increased the observation coverage of~~in~~ China and could lead to spurious trends in the top-down estimated

200 emissions. Figure 2 shows the changes in the observational coverage over different regions of China from 2013 to 2020

201 indicated by the ratio of areas that were influenced by observations to the total area of each region. ~~To investigate the potential~~

202 ~~impacts of this on the top-down estimations, the changes in the coverage of observations over different regions of China from~~

203 ~~2013 to 2020 were firstly calculated by the ratio of areas that were influenced by observations to the total area of each region~~

204 ~~(Fig. 2).~~ It can be clearly seen that the observational coverage increased from 2013 to 2015 with the expansion of the air quality

205 monitoring network in China, and became stable after 2015. However, the influence of the variation in the number of

206 observation sites varied among different regions. Over the North China Plain (NCP) region, the observational coverage was

207 approximately 90% in 2013, and reached 100% in 2014, suggesting that the variation in the observation sites may have little

208 influence on the estimated emission changes ~~in emissions~~ there. A similar conclusion can be drawn for the Southeast China

209 (SE) region, where the observational coverage was about 75% in 2013 and reached 100% in 2015. Elsewhere, in the other four

210 regions, the influence of the variation in observation sites is expected to be larger because of the low observational coverage

211 in both 2013 and 2014. For example, the observational coverage over the Northwest China (NW) region was less than 10% in

212 2013, but increased to about 60% in 2015. To better illustrate the impact of changes in observational coverage on the inversions,

213 ~~a~~the sensitivity analysis of the emission increments with the fixed observation sites or varying observation sites is performed

214 in this study (Text S2~~1~~ and Fig. S2). It shows that the additional emission increments caused by the increases of observation

215 sites would weaken the decreasing trends estimated in the fixed-site scenario for the emissions of $PM_{2.5}$, NO_x and NMVOC

216 and even lead to increasing trends for the emissions of PM_{10} and CO. In contrast, the increases of observation sites would

217 enhance the decreasing trends of SO_2 estimated in the fixed-site scenario. Such different behaviors are mainly related to the

218 different sign of the emission increment of different species as we illustrated in Text S2~~1~~. These results highlighted the

219 significant influences of the site differences on the estimated emissions and their trends, which should be noted by the potential

220 users. Therefore, in order to reduce this influence on the estimated emission trends, in our following analysis we mainly

221 analyze~~present~~ the emission trends after 2015, when the observational coverage had stabilized in all regions.

2.3 Data assimilation algorithm

223 We used the modified EnKF coupled with state augmentation method to constrain the long-term emissions of different

224 air pollutants. EnKF is an advanced data assimilation method ~~originally~~ proposed by Evensen (1994) that features ~~representing

225 the background error covariance matrix with a stochastic ensemble of model realizations. Through the use of ensemble

226 simulations, it has the ability to consider the indirect relationship between the emissions and chemical concentrations caused

227 by the complex physical and chemical processes in the atmosphere. It also allows for the estimation of flow-dependent

228 emission–concentration relationships that vary in time and space depending on the atmospheric conditions. The modified

229 EnKF is an offline application of the EnKF method that works by decoupling the analysis step from the ensemble simulation,

230 which has benefits in the reuse of costly ensemble simulations and makes high-resolution long-term inversion affordable (Wu

231 et al., 2020a). In this method, the ensemble simulation was performed firstly with the perturbed emissions, and then the

232 observations were assimilated to constrain the emissions (Wu et al., 2020a). The state augmentation method is a commonly

233 used parameter estimation method (Tandeo et al., 2020) in which the air pollutant emissions are taken as the state variable and

234 are updated according to the error covariance between the emissions and the concentrations of related species.

2.3.1 State variable and ensemble generations

236 The state variable used in this study was chosen following our previous multi-species inversion study (Kong et al., 2023),

237 which included the scaling factors for the emissions of fine-mode unspeciated aerosol (PMF), coarse-mode unspeciated aerosol

238 (PMC), BC, OC, NO_x, SO_2, CO, and NMVOC, as well as the chemical concentrations of $PM_{2.5}$, $PM_{10-2.5}$ (PM_{10} minus $PM_{2.5}$),

239 NO_2, SO_2, CO, and daily maximum 8-h O_3 (MDA8h O_3), which are formulated as follows:

240 $\boldsymbol{x} = [\boldsymbol{c}, \ \boldsymbol{\beta}]^T,$ (1)

241 $\boldsymbol{c} = [\mathbf{PM_{2.5}}, \mathbf{PM_{10-2.5}}, \ \mathbf{NO_2}, \ \mathbf{SO_2}, \mathbf{CO}, \ \mathbf{MDA8h \ O_3}],$ (2)

242 $\boldsymbol{\beta} = [\boldsymbol{\beta_{PMF}}, \ \boldsymbol{\beta_{PMC}}, \ \boldsymbol{\beta_{BC}}, \ \boldsymbol{\beta_{OC}}, \boldsymbol{\beta_{NO_x}}, \boldsymbol{\beta_{SO_2}}, \boldsymbol{\beta_{CO}}, \boldsymbol{\beta_{NMVOC}}],$ (3)

243 where $\boldsymbol{x}$ denotes the vector of the state variable, $\boldsymbol{c}$ denotes the vector of the chemical concentrations of different species, and

244 $\boldsymbol{\beta}$ denotes the vector of the scaling factors for the emissions of different species. Note that although the chemical concentration

245 variables are included in the state variable, they are not optimized simultaneously with the emission in the analysis step and

246 are only used to estimate the covariance between the emission and concentrations. Detailed descriptions of the state variables

247 are available in Table 1.

248 The ensemble of the scaling factors for different species was generated independently using the same method of Kong et

249 al. (2021), which has a medium size of 50 and considers the uncertainties of major air pollutant emissions in China, including

250 SO_2, NO_x, CO, NMVOCs, ammonia, PM_{10}, $PM_{2.5}$, BC, and OC. The uncertainties of these species were considered to be 12%,

251 31%, 70%, 68%, 53%, 132%, 130%, 208% and 258%, respectively according to the estimates of Li et al. (2017b) and Streets

252 et al. (2003). Note that in this study we did not perturb the emissions of different sectors to reduce the degrees of freedom in

253 the ill-posed inverse estimation problem. Instead, we only perturbed the total emissions of different species. Therefore, only

254 the total emissions of different species were constrained in this study. The ensemble of the chemical concentrations was then

255 generated through an ensemble simulation based on NAQPMS and the perturbed emissions calculated by multiplying the *a*

256 *priori* emissions by the ensemble of the scaling factors. This treatment implicitly assumes that the uncertainty in the chemical

257 concentration is mainly caused by the emission uncertainty. This makes sense on a monthly or yearly basis, considering that

258 substantial changes in emissions are expected to have taken place during the clean air action plans, which are subject to large

259 uncertainty. However, the lack of consideration of other error sources, such as those of the meteorological simulation and the

260 model itself, may lead to underestimation of the background error covariance and ~~overcorrection of the~~ emissions adjustment,

261 which is a potential limitation of this study. In addition, the dust and sea salt emissions were not perturbed and constrained in

262 this study, and thus the errors in the simulated fine and coarse dust emissions would influence the inversion of $PM_{2.5}$ and PM_{10}

263 emissions. As a result, the top-down estimated $PM_{2.5}$ and PM_{10} emissions will contain errors in the simulated dust and sea salt

264 emissions. Particularly, we did not consider the emissions of coarse dust during the inversion process since there is large

265 uncertainty in the simulated coarse dust emissions by current dust emission schemes (Zeng et al., 2020; Kang et al., 2011).

266 The ~~we found~~ large errors in the simulated coarse dust concentration ~~that~~ could ~~have~~ significantly influenced the inversion

267 results of PM_{10} emissions. For example, the simulated coarse dust concentration could sometimes be several orders of

268 magnitude higher than the observed PM_{10} concentration, leading to too low values of the inverse PM_{10} emissions

269 (approximately 0) over the regions that were not the typical dust source regions but were influenced by the transportation of

270 coarse dust. Therefore, we only used simulated PM_{10} concentrations from other sources in the inversion of PM_{10} emissions to

271 avoid the influences of the too large errors in simulated. ~~Consequently~~This is also similar to assume that the coarse dust

272 emission is equal to zero during the assimilation.~~,~~ However, in this way, the top-down estimated PM_{10} emissions in this study

273 would comprise all coarse dust emissions which should be noted by potential users. A detailed description of the ensemble

274 generation is available in Kong et al. (2021).

2.3.2 Inversion algorithm

276 We used a deterministic form of EnKF (DEnKF) proposed by Sakov and Oke (2008) to update the scaling factors of the

277 emissions of different species, which is formulated as follows:

278 $$\overline{x^a} = \overline{x^b} + \mathbf{K}(y^o - \mathbf{H}\overline{x^b}), \tag{4}$$

279 $$\mathbf{X}^a = \mathbf{X}^b - \frac{1}{2}\mathbf{KHX}^b \tag{5}$$

280 $$\mathbf{K} = \lambda \mathbf{B}_e^b \mathbf{H}^T (\mathbf{H}\lambda \mathbf{B}_e^b \mathbf{H}^T + \mathbf{R})^{-1}, \tag{6}$$

281 $$\mathbf{B}_e^b = \frac{1}{N-1}\sum_{i=1}^{N} X_i^b (X_i^b)^T, \tag{7}$$

282 $$\overline{x^b} = \frac{1}{N}\sum_{i=1}^{N} x_i^b ; X_i^b = x_i^b - \overline{x^b}, \tag{8}$$

283 where $\overline{x}$ denotes the ensemble mean of the state variable; the superscript **b** and **a** respectively denote the *a priori* and *a*

284 *posteriori* estimate; $\mathbf{X}^a$ is the analysed anomalies that can be used to calculate the uncertainty of the a posteriori emissions. **K**

285 is the Kalman gain matrix; $\mathbf{B}_e^b$ is the background error covariance matrix calculated by the background perturbation X^b; y^o is

286 the vector of the observation and **R** is the observation error covariance matrix; **H** is the linear observation operator, which

287 maps the model space to the observation space; λ is the inflation factor used to compensate for the underestimation of the

288 background error caused by the limited ensemble size and unaccounted error sources, which is calculated using the method of

289 Wang and Bishop (2003),

290 $$\lambda = \frac{(\mathbf{R}^{-1/2}d)^T \mathbf{R}^{-1/2}d - p}{trace\{\mathbf{R}^{-1/2}\mathbf{H}\mathbf{B}_e^b(\mathbf{R}^{-1/2}\mathbf{H})^T\}} \tag{9}$$

291 $$\boldsymbol{d} = \boldsymbol{y^o} - \mathbf{H}\overline{\boldsymbol{x^b}} \qquad (10)$$

292 where $\boldsymbol{d}$ is the observation innovation and $\boldsymbol{p}$ is the number of observations. Table S2~~1~~ summarized the calculated average

293 value (standard deviation) of the used inflation factor for different species. It shows that the inflation factor over the east China

294 (including NCP and SE region) was generally round 1.0, suggesting that the original ensemble can well represent the simulation

295 errors of the different air pollutants over these regions. The inflation factor is larger over the western China (including SW,

296 NW and Central regions), especially for PM_{10} (36.0–78.1) and SO_2 (7.8–176.1), suggesting that the original ensemble may

297 underestimate the simulation errors of the air pollutants. This is associated with the large biases in the simulated air pollutant

298 concentrations over there and reflect that the emission uncertainties assumed in our studies may be underestimated over these

299 regions. This also highlighted the importance of the use of inflation method during the inversion, otherwise it would lead to

300 filter divergency caused by the underestimations of the background error covariance.

301   In order to reduce the influence of the spurious correlations on the performance of data assimilation, the EnKF was

302 performed locally in this study in that the analysis was calculated grid by grid with the assumption that only measurements

303 located within a certain distance (cutoff radius) from a grid point would influence the analysis results of this grid. The use of

304 this local analysis method also allowed the inflation factor to be calculated locally and to vary in time and space, which can

305 help characterize the spatiotemporal variations of errors as we illustrated above. Similar to in Kong et al. (2021) and Kong et

306 al. (2023), the cutoff radius was chosen as 180 km for each species based on the wind speed and the lifespan of the species

307 (Feng et al., 2020). The same local scheme with a buffer area was also employed during the inversion to alleviate the

308 discontinuities in the updated state caused by the cut-off radius. A detailed description of the local analysis scheme is available

309 in Kong et al. (2021).

310   Table 1 summarizes the corresponding relationships between the emissions and chemical concentrations. Similar to ~~in~~

311 Ma et al. (2019) and Miyazaki et al. (2012), we did not consider the inter-species correlation during the assimilation~~,~~ to prevent

312 the spurious correlations between non- or weakly related variables. In most cases, observations of one particular species were

313 only allowed to adjust the emissions of the same species. The assimilation of $PM_{2.5}$ mass observation was more complicated

314 as there are multiple error sources in the simulated mass concentrations of $PM_{2.5}$, not only from primary emission, but also

315 from secondary production. In this study, the $PM_{2.5}$ mass observation was used to constrain the emissions of PMF, BC and OC

316 but not used to constrain the emissions of its precursors to avoid the spurious correlations and nonlinear chemistry effects,

317 which is similar to the scheme used in Ma et al. (2019). This is feasible since the emissions of primary $PM_{2.5}$ (i.e., PMF, BC

318 and OC) and the emissions of $PM_{2.5}$ precursors (e.g., SO_2, NO_2) were perturbed independently in our method, thus the

319 contributions of primary $PM_{2.5}$ emission and the secondary $PM_{2.5}$ productions to the $PM_{2.5}$ mass could be isolated through the

320 use of ensemble simulations. Meanwhile, the use of iteration inversion method (which will be introduced later) can further

321 reduce the influence of the errors in the precursors' emissions on the inversion of primary $PM_{2.5}$ emission, because~~since~~ the

322 errors of its precursors' emission would be constrained by their own observations during the iterations. However, the lack of

323 assimilation of speciated $PM_{2.5}$ observations may lead to uncertainties in the estimated emissions of PMF, BC and OC, which

324 is a potential limitation in current work. For example, if the a priori simulated $PM_{2.5}$ equals the observations, the emissions of

325 PMF, BC and OC would not be adjusted by using the current method. However, in such cases, there may still be ~~discrepancies~~

326 errors in the proportions of the emissions of different $PM_{2.5}$ components. To adjust the emissions of PMC, we used the

327 observations of $PM_{10-2.5}$ to avoid the potential cross-correlations between $PM_{2.5}$ and PM_{10} (Peng et al., 2018; Ma et al., 2019).

328 For the NO_x emissions, although the O_3 concentration are chemically related to the NO_x emissions, we did not use the O_3

329 concentrations to constrain the NO_x emission in this study since there is nonlinear relationship between the O_3 concentration

330 and NO_x emission which would lead to wrong adjustment of NO_x emissions (Tang et al., 2016).

331   The inversion of NMVOC emission is more difficult than other species due to the lack of long-term nationwide NMVOC

332 observations and the strong chemical activity. Previous studies usually assimilated the satellite observations of formaldehyde

333 and glyoxal to constrain the NMVOC emissions, such as Cao et al. (2018) and Stavrakou et al. (2015). However, these

334 inversion studies are hindered by the NO$_x$-VOC-O$_3$ chemistry and the inherent uncertainty in the satellite observations of

335 formaldehyde and glyoxal. Considering the strong chemical relationship between the O$_3$ and NMVOC, some pioneer studies

336 have also explored the method of assimilating ground-level O$_3$ concentrations to constrain the NMVOC emissions (Ma et al.,

337 2019; Xing et al., 2020), and demonstrated the effectiveness of this approach. For example, Ma et al. (2019) found that the

338 assimilation of O$_3$ concentration could adjust the NMVOC emissions in the direction resembling the bottom-up inventories,

339 and the forecast skill of O$_3$ concentrations were also improved, indicating that the constrained NMVOC emissions are improved

340 relative to their a priori. Inspired by these studies, we have made an attempt to constrain the NMVOC emissions based on the

341 MDA8h O$_3$. The use of MDA8h O$_3$ rather than the daily mean O$_3$ concentration is to avoid the effects of the nighttime O$_3$

342 chemistry. For example, the simulation errors in the titration effects of NO$_x$ may influence the simulated O$_3$ concentrations

343 during nighttime and affect the inversion results of NMVOC. An important issue that should be noted when using the MDA8h

344 O$_3$ to constrain the NMVOC emission is the nonlinear interactions among NO$_x$, NMVOC and O$_3$. On the one hand, the O$_3$

345 concentrations are dependent not only on the NMVOC emissions but also on the NO$_x$ emissions. The errors in the a priori

346 emissions of NO$_x$ would also contribute to the simulation errors of O$_3$, and deteriorate the inversion of NMVOC. The iteration

347 inversion scheme could help deal with this issue as the errors in the NO$_x$ emissions will be constrained by the NO$_2$ observations

348 in the next iteration, which can reduce the influences of errors in the NO$_x$ emission on the inversion of NMVOC emission

349 based on MDA8h O$_3$ concentrations. This is in fact similar to the approach used by Xing et al. (2020) who firstly constrained

350 the NO$_x$ emissions based on observations of NO$_2$, and then constrained the NMVOC emissions based on O$_3$ concentrations.

351 Also, in Feng et al. (2024), the NO$_2$ observations were simultaneously assimilated to constrain the NO$_x$ emissions to account

352 for the influences of errors in NO$_x$ emissions on the NMVOC emissions, suggesting that the iteratively nonlinear joint inversion

353 of NOx and NMVOCs is an effective way to address the intricate relationship among VOC-NO$_x$-O$_3$ (Feng et al., 2024).

354 Similarly, the errors in the CO emissions which may be significant according to our following analysis are also constrained in

355 a similar way to reduce the potential influences on the inversion of NMVOC emission. On the other hand, the emission

356 adjustments of NMVOC may exhibit bidirectionality dependent on the VOC-limited or NO$_x$-limited regimes. According to

357 Fig. 3, the NMVOC emissions were adjusted in alignment with the direction of the O$_3$ errors, suggesting a VOC-limited regime

358 over urban areas in China, given that the O$_3$ observation sites are predominantly situated in the urban areas. This agrees with

359 Ren et al. (2022) who diagnosed the NO$_x$-VOC-O$_3$ sensitivity based on the satellite retrievals and found that the VOC-limited

360 regimes are mainly located in the urban areas in China. This suggests that the relationship between the O$_3$ concentrations and

361 VOC emissions could be reasonably reflected by our inversion system, providing the feasibility in utilizing the O$_3$ observations

362 to constrain the VOC emissions. Note that due to the lack observations of the VOC components, we only optimize the gross

363 emissions of the VOC during the assimilation.

364 As we illustrated before, there exists nonlinear effects in the atmospheric chemistry which could influence the inversion

365 results of different species. In addition, since we did not consider the temporal variations in the a priori emissions, it was

366 expected that there would be significant biases in the a priori emissions for the years after 2013, as substantial changes in

367 emissions were expected owing to the implementation of strict emission control measures. Such bias in the a priori emissions

368 does not conform to the unbiased hypothesisassumption of the EnKF that the a priori estimate is unbiased, which could thus

369 lead to incomplete adjustments of the a priori emissions and degrade the performance of the data assimilation (Dee and Da

370 Silva, 1998). To address these issues, an iteration inversion scheme was employed in this study, which has been used previously

371 in Kong et al. (2023). The main idea of the iteration inversion scheme is to preserve the background perturbation $\mathbf{X^b}$ but to

372 update the ensemble mean of the state variable $\overline{\mathbf{x^b}}$ based on the inversion results of the kth iteration and corresponding the

373 model simulations driven by the inversion results of the kth iteration. ThereforeAccording to this, a new single model

374 simulation is required to be conducted by using the a posteriori emission from the previous iteration as the input to update the

375 ensemble mean of the original ensemble. This enables the observational information and the adjusted emissions to be promptly

376 incorporated into the model, thereby providing feedback for the adjustments of emission in the next iteration. However, we

377 did not reassemble the ensemble simulation for each iteration due to the expensive computational cost of the ensemble

378 simulation. Therefore, in each iteration calculation, the ensemble perturbation that were used to calculate the background error

379 covariance matrix remains the same with only the ensemble mean being updated based on the inversion results of the previous

380 iteration. The state variable used in the $(k + 1)$th inversions is then formulated as follows:

381 $$x_i^{b,k+1} = \left[c^k + c_i^e - \bar{c^e}, \beta^k + \beta_i^e - \overline{\beta^e} \right]^T, \tag{11}$$

382 where c^k represents the model simulations ~~using~~ driven by the inversed emissions of the kth iteration, c_i^e represents the ith

383 member of ensemble simulations with an ensemble mean of $\bar{c^e}$, β^k represents the updated scaling factors at the kth iteration,

384 and β_i^e represents the ith member of the ensemble of scaling factors with a mean value of $\overline{\beta^e}$. In each iteration, all emissions

385 are updated simultaneously and t~~T~~wo rounds of iteration were conducted in this study based on our previous inversion study

386 to maintain a balance between the inversion performance and the computational cost of the long-term inversions (Kong et al.,

387 2023).

2.3.3 Setup of inversion estimation

389 Based on this inversion scheme, we ~~firstly~~ constrained the daily emissions of PMF, PMC, BC, OC, NO$_x$, SO$_2$, CO, and

390 NMVOCs, from 2013 to 2020, based on the daily averaged observations of PM$_{2.5}$, PM$_{10-2.5}$, NO$_2$, CO, and MDA8h O$_3$.

391 However, due the lack of enough speciated PM$_{2.5}$ observation, the model performance driven by the inverse emission for the

392 BC, OC and primary unspeciated PM$_{2.5}$ have not been thoroughly evaluated. It is thus currently unclear for the quality of the

393 inverse emissions of BC, OC and primary unspeciated PM$_{2.5}$. Also, the lack of speciated PM$_{2.5}$ observations could lead to

394 uncertainties in the estimated emissions of PMF, BC, and OC as we mentioned before. Considering this, similar to in Kong et

395 al. (2023), although we made attempt to estimate the emissions of BC, OC and primary unspeciated PM$_{2.5}$, we have reservations

396 about their inversion results and only provide the emissions of PM$_{2.5}$ (PMC+BC+OC) and PM10 (PM$_{2.5}$ + PMC) in current

397 stage. In future, we will collect more speciated PM$_{2.5}$ observations to comprehensively quantify the accuracy of their inversion

398 results, after which the emissions of these species would be released. Meanwhile, the speciated PM$_{2.5}$ observations could be

399 assimilated under the current inversion framework. This could provide us with further constrains on the emissions of BC, OC

400 and primary PM$_{2.5}$. ~~similar to in Kong et al. (2023), we only provide the emissions of PM$_{2.5}$ (PMF+BC+OC) and PM$_{10}$~~

401 ~~(PM$_{2.5}$+PMF) for the aerosol species since the lack of speciated PM$_{2.5}$ observations would lead to uncertainties in the estimated~~

402 ~~emissions of PMF, BC, and OC as we mentioned before.~~ Meanwhile, as mentioned in subsection 2.3.1, the meteorological and

403 model uncertainty were not considered in the ensemble simulation. Thus, the errors in the meteorological simulation would

404 cause fluctuations in the daily emissions that ~~could~~ contaminate the inversion results and are difficult to isolate from the

405 inherent variations of emissions (Tang et al., 2013). Considering this, the daily emissions were averaged to monthly values to

406 reduce the influences of random model errors after the assimilation.

3 Performance of the chemical data assimilation system

3.1 Analysis of OmF and emission increment

409 The observation-minus-forecast (OmF) and emission increment (*a posteriori* emission minus *a priori* emission) were

410 firstly analyzed to demonstrate the performance of the data assimilation. As shown in Fig. 3, the *a priori* simulation generally

411 underestimated the PM$_{2.5}$ concentrations over the NCP, SE and SW regions (positive OmF values) during 2013–2014, but

412 overestimated the PM$_{2.5}$ concentrations from 2016, reflecting the effects of the emission control measures during these years.

413 In the NE, NW and central China (hereafter, "Central") regions, obvious underestimation of the PM$_{2.5}$ concentration was found

414 (positive OmF values) throughout almost the entire assimilation period. Similarly, the OmF values of PM$_{10}$ were positive

415 throughout the whole assimilation period over all regions of China. In contrast, the OmF values for SO$_2$ were negative for most

regions, and the negative OmF values over the NCP region became larger as the years progressed, which reflects the effects of the emission control measures. The OmF for NO_2 reveals a seasonal variation over the NCP and SE regions, with ~~negative~~negative values during summer and ~~positive~~positive values during winter, while there were obvious positive OmF values over the NE, SW, NW and Central regions. In terms of CO, large positive OmF values were found over all regions of China, and there were decreasing trends in the OmF values of CO over different regions of China associated with the emission control policies during these years. The OmF values for O_3 were positive over most regions of China, except the NW region. These results provide us with valuable information on the potential deficiencies in the *a priori* emissions. However, since our inversion method did not differentiate between anthropogenic and natural emissions, the biases in the model simulation may also be attributable to the errors in natural emissions such as dust, especially over the major dust-source areas of China (e.g., the NW and Central regions). In addition, the effects of emission control were not considered in the *a priori* emissions, which is another important contributor to the errors in the model simulation for the later years. Thus, the emission increments calculated by the assimilation should reflect the combined effects of errors in the anthropogenic and natural emissions, as well as the emission control.

The calculated emission increments were consistent with the OmF values for all species, which indicates that the data assimilation method can probably constrain the emissions based on the observations. According to Fig. 3, the emission increments were positive for $PM_{2.5}$ over the NE, NW and Central regions, for NO_2 over the NE, SW, NW and Central regions, and for PM_{10}, CO and NMVOC over almost all regions throughout the assimilation period. In contrast, the emission increments were negative for the SO_2 emissions for most cases. Consistent with the OmF values, the emission increments were positive for $PM_{2.5}$ over the NCP, SE and SW regions during 2013–2014, but became negative from 2016 owing to the implementation of strict emission control measures. The emission increments for NO_x also showed significant seasonal variation over the NCP and SE regions, being positive during winter and negative during summer. The *a posteriori* biases for the model simulations of different species were also plotted to assess the performance of the data assimilation. It can be clearly seen that the biases were substantially reduced for all species, and the calculated root-mean-square error (RMSE) reduced by 23.2–52.8% for $PM_{2.5}$, 19.9–37.8% for PM_{10}, 36.4–77.3% for SO_2, 18.3–25.2% for NO_2, 29.9–40.5% for CO, and 4.4–26.1% for O_3 over the different regions of China, suggesting a good performance of the data assimilation system.

3.2 Evaluation of the inversion results

Table 2 shows the calculated evaluation statistics for the inversion at different temporal scales. It can be clearly seen that the model simulation with the *a posteriori* emission inventory reproduced well the magnitude and temporal variations of the different air pollutants in China, with calculated correlation coefficients of approximately 0.77, 0.72, 0.64, 0.67, 0.69 and 0.71, and normalized mean biases of approximately 4.5%, −4.6%, −9.0%, −3.9%, −8.8% and 9.5%, for the hourly concentrations of $PM_{2.5}$, PM_{10}, SO_2, NO_2, CO and O_3, respectively. Moreover, the *a posteriori* model simulation achieved comparable accuracy with the air quality reanalysis data we developed in Kong et al. (2021) in terms of the RMSE, which was 32.4 $\mu g \cdot m^{-3}$, 53.1 $\mu g \cdot m^{-3}$, 24.9 $\mu g \cdot m^{-3}$, 19.9 $\mu g \cdot m^{-3}$, 0.56 $mg \cdot m^{-3}$ and 34.9 $\mu g \cdot m^{-3}$, respectively, for these species at the hourly scale. At the daily, monthly and yearly scales, the constrained model simulation performed better, with RMSEs of about 9.1–20.0 $\mu g \cdot m^{-3}$ ($PM_{2.5}$), 18.5–31.6 $\mu g \cdot m^{-3}$ (PM_{10}), 11.5–16.0 $\mu g \cdot m^{-3}$ (SO_2), 8.1–12.8 $\mu g \cdot m^{-3}$ (NO_2), 0.28–0.39 $mg \cdot m^{-3}$ (CO), and 14.2–26.1 $\mu g \cdot m^{-3}$ (O_3), which were respectively reduced by 56.7–67.3%, 49.2–52.1%, 68.8–72.8%, 36.3–39.8%, 47.0–58.0%, and 22.9–30.5% compared to the RMSEs of the *a priori* simulations. We also compared the model performance driven by the inverse inventory with that driven by more recent bottom-up inventories (MEIC and HTAPv3) by taking the simulation results of year 2020 as an example to give us a more objective understanding of the accuracy of the inverse emission inventory. It shows that the inverse emission generally achieves better performance in simulating the air pollutant concentrations in China than the MEIC and HTAPv3 (Table S3). It is also encouraging to find that the model performance driven by CAQIEI and MEIC-HTAPv3 is similar for $PM_{2.5}$, PM_{10}, and SO_2 over the NCP, NE, SE and SW regions, both significantly improved from the a priori emission

458 inventory. This suggest that both the top-down and recent bottom-up emission inventories have good performance in capturing

459 the emission changes of these species over these regions and they yield consistent estimations. Detailed information on the

460 configurations of the model simulation results driven by MEIC-HTAPv3 and the comparisons results are available in Text S3.

461 All tThese validation results confirmconfirm the good performance of the data assimilation method and suggest that the

462 inversed emissions inventory has the capability to reasonably represent the magnitude and long-term trends of the air pollutant

463 emissions in China during 2013–2020.

4 Results

465 Based on the top-down estimation, the gridded emissions for $PM_{2.5}$, PM_{10}, SO_2, CO, NO_x and NMVOCs over China from

466 2013 to 2020 were developed into what we have called the Inversed Emissions Inventory for Chinese Air Quality (CAQIEI).

467 In the following sections, we first analyze the magnitude and seasonality of the air pollutant emissions in China by taking 2015

468 as a reference year when the number of observation sites became stable. After that, the changes in emissions of different air

469 pollutants from 2015 to 2020 are analyzed and compared between the two clean air action plans in China. Note that due to the

470 impacts of the changes in observation coverage, it is difficult to estimate the overall emission reduction rates during the 2013–

471 2017 action plan by using our inversion results. The emission change rates during 2015–2017 were then sampled in this study

472 to assess the mitigation effects during the 2013–2017 action plan and to be compared with the emission change rates during

473 2018–2020. Finally, CAQIEI is compared to the previous bottom-up and top-down emission inventories to validate our top-

474 down estimation and identify the potential uncertainties in the current understanding of China's air pollutant emissions.

4.1 Top-down estimated Chinese air pollutant emissions in 2015

476 The top-down estimated emissions of different species in 2015 are as follows: 25.2 Tg of NO_x, 17.8 Tg of SO_2, 465.4 Tg

477 of CO, 15.0 Tg of $PM_{2.5}$, 40.1 Tg of PM_{10}, and 46.0 Tg of NMVOCs. Note that these values not only contain anthropogenic

478 emissions but also natural (e.g., dust and biogenic NMVOC) emissions. Thus, the top-down estimated emissions of PM and

479 NMVOCs were higher than those estimated by previous studies, as we mention in the following sections. Emission maps of

480 all species in 2015 are shown in Fig. 4, and the calculated emissions of different species over different regions are presented

481 in Table 3. According to Fig. 4, higher air pollutant emissions are widely distributed in the megacity clusters (e.g., NCP,

482 Yangtze River Delta and Pearl River Delta) and the developed cities in China, reflecting the influences of human activities.

483 NCP was the region with the largest emission intensity of air pollutants in China, contributing 5.1 Tg of NO_x, 3.5 Tg of SO_2,

484 82.2 Tg of CO, 2.7 Tg of $PM_{2.5}$, 8.7 Tg of PM_{10} and 9.0 Tg of NMVOCs to the total emissions in China. The inversion results

485 also demonstrate the contribution of natural sources to the air pollutant emissions, such as the soil NO_x emissions and the

486 biogenic NMVOC emission distributed in the Tibet Plateau region. In general, the majority of air pollutant emissions were

487 located in eastern China (including the NCP, NE and SE regions), where the economy is relatively well developed, which in

488 total accounted for 66.0% of NO_x, 60.9% of SO_2, 57.5% of CO, 60.4% of $PM_{2.5}$, 60.5% of PM_{10}, and 67.8% of NMVOC

489 emissions in China. However, although the GDP of western China (including the SW, NW and Central regions) is less than

490 one third that of eastern China, the top-down estimation indicates that the air pollutant emissions in western China could have

491 accounted for about 32.2–42.5% of the total emissions, which reflects the low emission control levels over these regions.

492 Figure 5 shows the monthly variations of air pollutant emissions in China for year 2015. The monthly profile of NO_x

493 emissions was relatively flat among the six species. SO_2 and CO showed higher emissions during wintertime because of the

494 enhanced residential emissions associated with higher coal consumption for heating during that time of year. Meanwhile, the

495 emission factor for CO from vehicles in winter was also higher than in other seasons, due to additional emissions from the

496 cold-start process (Kurokawa et al., 2013; Li et al., 2017b). $PM_{2.5}$ and PM_{10} had higher emissions during winter and spring,

497 which, on the one hand was due to the enhanced emissions from the residential and industrial sectors during wintertime (Li et

498 al., 2017b), whilst on the other hand was due to the enhanced dust emissions during the spring season (Fan et al., 2021).

499 Emissions of NMVOCs exhibited strong monthly variations, with higher emissions mainly in summer because of the enhanced

500 NMVOC emissions from biogenic sources.

501 **4.2 Top-down estimated emission changes of different air pollutants**

502 **4.2.1 Emission changes of particular matter**

503   Figure 6 shows the top-down estimated emission changes of $PM_{2.5}$ and PM_{10} over China during two clean air action

504 periods. Both $PM_{2.5}$ and PM_{10} emissions decreased substantially, by 44.3% and 21.2% respectively, from 2013 to 2020. On

505 the contrary, the top-down estimates showed increases of $PM_{2.5}$ and PM_{10} emissions in 2014 and 2015, but this would be a

506 spurious trend caused by the changes of observation sites as we discussed in Text S2~~1~~. Therefore, the emissions in 2013 and

507 2014 were discarded to prevent the spurious trends. According to Fig. 6, the $PM_{2.5}$ emissions decreased by 14.5% from 2015

508 (15.0 Tg) to 2017 (12.8 Tg), and the reduction in emissions was roughly uniform throughout the period, which was about 8%

509 compared to previous years. The PM_{10} emissions showed a smaller reduction rate (−7.2%) than that of $PM_{2.5}$, decreasing from

510 40.1 Tg in 2015 to 37.2 Tg in 2017. Compared with the emission reduction rate during 2015–2017, both $PM_{2.5}$ and PM_{10}

511 showed larger emission reduction rates during 2018–2020, estimated to be 27.2% and 25.5%, respectively. The emission

512 reductions in each year were also larger, especially for PM_{10}. For example, $PM_{2.5}$ and PM_{10} emissions reduced by about 19.3%

513 and 14.0% in 2019 compared to 2018. This may have been due to that in addition to the strict controls imposed on the industrial

514 and power sectors during the 2013–2017 action period, the residential emissions have been strengthened during the 2018–

515 2020 action period. In particular, "coal-to-electricity" and "coal-to-gas" strategies were vigorously implemented in northern

516 China during the 2018–2020 action to reduce coal consumption and related air pollutant emissions (Liu et al., 2016; Wang et

517 al., 2020a). Thus, our inversion results confirm the effectiveness of the controls on residential emissions in terms of reducing

518 the emissions of $PM_{2.5}$ and PM_{10}. In addition, the control of non-point sources, such as blowing-dust emissions, was also

519 strengthened during the 2018–2020 action period, which is consistent with the faster reduction of PM_{10} emissions during 2018–

520 2020. The annual trends of $PM_{2.5}$ and PM_{10} emissions were also calculated in China using the Mann–Kendall trend test and

521 the Theil–Sen trend estimation method, the results of which are summarized in Table 4. The calculation of emission trends can

522 help extend the existing emission datasets forward in time to produce up-to-date products. The top-down estimated trends of

523 $PM_{2.5}$ and PM_{10} emissions were −1.4 and −2.6 Tg/year during 2015–2020, attributable to the strict emission control measures

524 imposed during the two clean air action plans. As mentioned, the decreasing trends were larger during 2018–2020 (−1.5 and

525 −4.6 Tg/year) than during 2015–2017 (−1.1 and −1.5 Tg/year).

526   On the regional scale (Fig. S3), it can be clearly seen that the $PM_{2.5}$ emissions decreased consistently over all regions, by

527 59.8% in NCP, 49.6% in SE, 39.5% in NE, 35.8% in SW, 33.2% in NW, and 41.0% in Central, from 2015 to 2020. The NCP

528 region showed the largest reduction in emissions among the six regions, with its emission reduction rate being almost larger

529 than 10% in each year. This is consistent with the strictest emission control policies having been imposed over the NCP region.

530 The SE region showed a similar emission reduction~~s in emissions~~ to the NCP region, with its emission reduction rate being

531 larger than 10% in most years. Obvious increases of $PM_{2.5}$ emissions could be found over the NW region from 2013 to 2015

532 owing to the increase in the number of observation sites in those years. After 2015, $PM_{2.5}$ emissions generally decreased over

533 the NW region, while there was a slight rebound in $PM_{2.5}$ emissions in 2016 and 2018, possibly due to the influences of the

534 errors in fine dust emission. The Central region showed different characteristics of emission changes to the other regions

535 insofar as it showed little change in $PM_{2.5}$ emissions during 2015–2018 but large reductions in 2019. This may be consistent

536 with the control of emissions over the Fenwei Plain area (the part of the Central region where the emission intensity is largest)

537 being weak during the 2013–2017 action plan but strengthened during the 2018–2020 action plan. In terms of the $PM_{2.5}$

538 emission trends over the different regions, the calculated $PM_{2.5}$ emission trends were about −0.32 Tg/year in NCP, −0.32

Tg/year in SE, −0.24 Tg/year in NE, −0.21 Tg/year in SW, −0.09 Tg/year in NW, and −0.15 Tg/year in Central, from 2015 to 2020.

The changes of PM_{10} emissions were generally similar to those of $PM_{2.5}$, i.e., with decreases in all regions from 2015 to 2020 (Fig. S4). The top-down estimated PM_{10} emission reductions from 2015 to 2020 were about 3.5 Tg (40.0%) in NCP, 2.6 Tg (35.5%) in SE, 3.0 Tg (36.6%) in NE, 2.0 Tg (35.9%) in SW, 1.0 Tg (25.3%) in NW, and 1.3 Tg (21.6%) in Central; and the calculated trends were about −0.64 Tg/yr, −0.52 Tg/yr, −0.51 Tg/yr, −0.40 Tg/yr, −0.20 Tg/yr, and −0.27 Tg/yr, respectively. However, due to the influences of the changes in the number of observation sites, the PM_{10} emissions over the NE, SW and NW regions increased substantially from 2013 to 2015, while they decreased in almost all years after 2015. Different from the other regions, the Central region showed increases in PM_{10} emissions from 2015 to 2018, by about 0.92 Tg (14.9%), but substantial decreases in 2019 and 2020. The result also shows that most PM_{10} emission reductions were achieved during the 2018–2020 action plan. According to CAQIEI, the PM_{10} emissions decreased by 0.64–2.3 Tg (17.4–31.8%) from 2018 to 2020, which accounted for 48.4–169.0% of the total reduction in emissions from 2015 to 2020. This again emphasizes the effectiveness of the control of blowing-dust emissions during the 2018–2020 action plan.

4.2.2 Emission changes of gaseous air pollutants

4.2.2.1 SO_2 and CO

Figure 7 shows the emission changes of different gaseous air pollutants in China from 2013 to 2020. Similar to the PM emissions, SO_2 and CO emissions decreased continuously during the two action plan periods, with top-down estimated emission reductions of about 9.6 Tg (54.1%) and 166.3 Tg (35.7%) for SO_2 and CO from 2015 to 2020, respectively. Meanwhile, both SO_2 and CO showed a significant decreasing trend from 2015 to 2020, with estimated trends of approximately −2.1 Tg/yr and −36.0 Tg/yr, respectively (Table 5). The reductions in SO_2 and CO emissions are closely consistent with the strict emission control measures imposed during the action plan periods, such as the phasing out of outdated industrial capacity and high-emitting factories, the strengthening of emission standards for industry and the power sector, the elimination of small coal-fired industrial boilers, and the replacement of coal with cleaner energies, which reflects the effectiveness of the emission control measures during the two action plan periods. Reductions of SO_2 emission were generally steady during the two action plan periods, which were approximately 4.2 Tg (23.8%) from 2015 to 2017 and 2.5 Tg (23.5%) from 2018 to 2020. However, CO showed a different emission reduction rate during the two action plan periods, with its emission reductions (67.1 Tg, 18.3%) during 2018–2020 being larger than those (45.6 Tg, 9.8%) during 2015–2017. This contrast may reflect the different emission control policies during the two clean air action periods, as well as the different emission distributions among the sectors between SO_2 and CO. According to the estimates of Zheng et al. (2018), the share of emissions from the industrial and power sector for SO_2 (77%) is nearly double that for CO (39%). Thus, the smaller reduction of CO emissions than that of SO_2 during 2015–2017 provides evidence that the 2013–2017 action plan mainly focused on controlling the emissions from the industrial and power sectors. During the 2018–2020 action plan, strict control measures targeted on the residential and transportation sectors were also implemented, which together account for 61% of CO emissions but only 23% of SO_2 emissions. As a result, CO showed a larger emission reduction rate during 2018–2020, while the emission reduction rate for SO_2 was similar to that during 2015–2017. The calculated trends of SO_2 and CO emissions during the two action plans are presented in Table 4, which are −2.1 Tg/yr and −1.3 Tg/yr for SO_2, and −22.8 Tg/yr and −33.5 Tg/yr for CO, respectively.

The reduction of SO_2 and CO emissions was also evident on the regional scale (Fig. S5 and S6). According to the top-down estimation, the reduction of SO_2 emissions ranged from 0.44 to 2.42 Tg (41.7–69.9%) from 2015 to 2020, with the NCP region exhibiting the largest reductions. The calculated decreasing trend of SO_2 emissions was also significant over all regions, ranging from −0.08 Tg/yr over the NW region to −0.57 Tg/yr over the NCP region (Table 5). With regards to the emission reduction rate during the different action plans, the results suggest that the emission reduction rate of SO_2 was higher during 2015 – 2017 (by 20.8–39.8%) than that during 2018–2020 (16.6–29.0%) over the NCP, SE, NE and SW regions. This may

581 have been because, after the strict emission controls imposed upon industry and power plants during the 2013–2017 action

582 plan, the room for further reductions in SO_2 emissions become smaller during the 2018–2020 action plan over these regions.

583 Although residential and vehicle emissions were controlled more strictly during the 2018–2020 action plan, in total they

584 account for ~20% of anthropogenic SO_2 emissions in China (Zheng et al., 2018). Thus, the enhanced reductions in SO_2

585 emissions from the residential and transportation sectors may not have been able to fully compensate for the weakened

586 reductions from the industrial and power sectors, leading to a smaller SO_2 emission reduction rate over these regions. In

587 contrast, the SO_2 emission reduction rate during 2018–2020 (31.1–34.8%) was higher than that during 2015–2017 (14.1–

588 20.4%) over the NW and Central regions. This may have been due to the fact that the emission controls over the NW and

589 Central regions were relatively weak during the 2013–2017 action plan (as also evidenced by the emission reduction rates of

590 other species) owing to its less-developed economy. During the 2018–2020 action plan, the emission controls over these two

591 regions were strengthened, which led to their higher emission reduction rates. Accordingly, the enhanced SO_2 emission

592 reduction rates over the NW and Central regions compensated for the weakened reduction rates over the other regions, leading

593 to a steady SO_2 emission reduction rate on the national scale.

594 The reductions of CO emissions from 2015 to 2020 were approximately 14.9–42.3 Tg (21.6–51.4%) over the different

595 regions of China, with significant decreasing trends ranging from −3.0 to −8.7 Tg/yr (Fig. S6 and Table 5). Consistent with

596 the comparisons of national CO emission reduction rates between the two action plans, the emission reduction rates during

597 2015–2017 (4.4–24.6%) were estimated to be smaller than those during 2018–2020 (12.2–24.6%) over all the different regions

598 except the Central region, where the CO emission reduction rate was similar during the two action plans (Fig. S6).

599 **4.2.2.2 NO_x and NMVOCs**

600 The top-down estimated NO_x and NMVOC emissions showed different changes to the other four species, by increasing

601 during 2015–2017 but declining during 2018–2020. Specifically, NO_x emissions increased slightly by 5.9% from 2015 (25.2

602 Tg) to 2017 (26.6 Tg), with a non-significant increasing trend of 0.74 Tg/yr. Then, NO_x emissions began to decrease in 2018,

603 with a top-down estimated emission reduction and calculated trend of approximately 3.1 Tg (12.7%) and −1.6 Tg/yr,

604 respectively, from 2018 to 2020. NMVOCs showed stronger emission increases than did NO_x, with top-down estimated

605 emission increases of approximately 12.7 Tg (27.6%) and a calculated emission trend of about 6.3 Tg/yr from 2015 to 2017.

606 Similar to NO_x, NMVOC emissions began to decrease after 2018, with a top-down estimated reduction of approximately 2.6

607 Tg (−4.4%) from 2018 to 2020, and a calculated trend of about −1.3 Tg/yr.

608 The increases of NO_x and NMVOC emissions during 2015–2017 suggest that the 2013–2017 action plan may not have

609 achieved desirable mitigation effects on these two species. For NO_x emissions, the upward trend may have been associated

610 with the following factors. On the one hand, vehicle exhaust is one of the most important sources of NO_x in China, accounting

611 for 31% of all NO_x emissions nationally (Zheng et al., 2018). From 2013 to 2017, the number of vehicles in China continued

612 to increase and reached 310 million in 2017, approximately 33.5% higher than in 2013 (MEE, 2017), which led to increases

613 of NO_x emissions from vehicles in China. On the other hand, although the 2013–2017 action plan was effective in reducing

614 the NO_x emissions from coal-fired power plants by promoting denitrification facilities and an ultra-low emission standard, the

615 mitigation impacts on industrial NO_x emissions may have been relatively small. For example, Wang et al. (2019a) compiled a

616 unit-based emissions inventory for China's iron and steel industry from 2010 to 2015, based on detailed survey results of

617 approximately 4900 production facilities in mainland China. They found that there were almost no NO_x control measures in

618 China's iron and steel industry during 2010–2015, resulting in a 12.4% increase in China's NO_x emissions from the iron and

619 steel industry in 2015 compared to 2010. In addition, although the penetration rate of denitrification facilities in China's cement

620 industry reached 92% in 2015, the actual operating rate of denitrification facilities in the cement industry was not desirable,

621 due to the lack of online emission monitoring systems. According to the research results of the Ministry of Ecology and

622 Environment, 800, 1300, and 1400 cement production kilns were equipped with selective non-catalytic denitrification facilities

from 2013 to 2015, but the actual operating rates were only 51%, 54% and 73%, respectively (Liu et al., 2021). In addition, the new precalciner kilns used in the cement industry have a higher NO_x emission factor, such that the shift from traditional vertical kilns to precalciner kilns has to some extent increased the cement industry's emissions of NO_x (Liu et al., 2021). Thus, there is evidence that the mitigation effects of the industrial control measures on NO_x emissions may not be as significant as expected. Overall, the increased number of vehicles may have offset the emission mitigation effects brought about by the control of power plants, and the mitigation effects of controlling industrial NO_x emissions were also undesirable. Consequently, NO_x emissions in China may not have decreased, and even increased slightly, during the 2013–2017 action plan. Figure S7 further shows the changes in NO_x emissions over different regions of China, revealing that NO_x emissions over the NCP, SE, NE and SW regions were roughly unchanged (by less than 5%) from 2015 to 2017, while they increased over NW (18.6%) and Central (17.5%). This is consistent with previous results and indicates that NO_x emissions may have increased over the NW and Central regions, possibly due to their increased human activities and weak emission controls.

In terms of NMVOC emissions, since the inversion results did not differentiate between anthropogenic and biogenic sources, the changes in NMVOC emissions may have been related to both anthropogenic and biogenic emissions. With respect to anthropogenic emissions, previous bottom-up studies have suggested that China's NMVOC emissions did not decline during the 2013–2017 action plan, due to the lack of effective control measures on the chemical industry and solvent use (Zheng et al., 2018; Li et al., 2019c). According to the estimates of Li et al. (2019c), China's NMVOC emissions from solvent use increased by 11.1% in 2017 compared to those in 2015. Meanwhile, the increase in the number of vehicles in China may also have led to an increase in NMVOC emissions from transportation. Thus, the increases of NMVOC emission during 2015– 2017 estimated by our inversion inventory may be related to the increases in anthropogenic NMVOC emissions from the chemical industry, solvent use, and vehicles. For the trends of biogenic NMVOC emissions, the CAMS global emission inventory shows that there were only little changes in the biogenic NMVOC emissions in China from 2013 to 2018 (Sect. 4.3.3), suggesting little contributions of the biogenic sources to the increased NMVOC emission in China. Figure S8 further shows the changes in NMVOC emissions over different regions of China, which suggests consistent increases in NMVOC emissions from 2015 to 2017 over different regions. According to the top-down estimations, NMVOC emissions increased by 30.5%, 25.2%, 18.5%, 10.9%, 50.5% and 63.1% over the NCP, SE, NE, SW, NW and Central regions, respectively. Again, the NW and Central regions exhibited the largest emission increases among the six regions, which is consistent with their elevated levels of human activity and weak emission controls.

The decrease in NO_x and NMVOC emissions after 2018 suggests that the emission control strategy of the Chinese government had reached a point of optimization. The 2018–2020 action plan not only strengthened the controls over the industrial and power sectors, but also the transportation sector, especially for diesel vehicles with high NO_x emissions. For example, the Chinese government released the "Action Plan for the Control of Diesel Trucks", and vigorously promoted an adjustment of the transportation structure of China by gradually improving the availability of rail transport. As a result, there was a downward trend in NO_x emissions in China. The top-down estimated reductions of NO_x emissions were approximately 0.81 Tg (17.2%) over NCP, 0.98 Tg (14.0%) over SE, 0.37 Tg (9.4%) over NE, 0.51 Tg (12.2%) over SW, 0.13 Tg (11.0%) over NW, and 0.32 Tg (9.2%) over Central (Fig. S7). The decrease in NMVOC emissions after 2018 may on the one hand have been related to the strengthening of vehicle controls during the 2018–2020 action plan, whilst on the other hand it may have been related to the promotion of clean heating plans in the northern region, which reduced the emissions of NMVOCs from residential sources. However, the decreases in NMVOC emissions were smaller than those in NO_x, which were estimated to be 0.84 Tg (6.9%) over NCP, 0.47 Tg (2.8%) over SE, 0.98 Tg (10.1%) over NE, and 0.53 Tg (14.1%) over NW (Fig. S6). Different from other regions, the NMVOC emissions over the SW and Central regions remained almost unchanged during the 2018–2020 action plan (Fig. S8).

4.2.3 Changes in the distribution pattern of emissions in China

Due to the different emission control intensities over the different regions of China, the emission distribution patterns of the different species may also have been altered, which could have influenced the distributions of air pollution in China. Based on CAQIEI, we further investigated the emission distribution patterns, as well as their changes, during the two action plans. Maps of the emission changes of different species during 2015–2017 and 2018–2020 are presented in Fig. 8. The shares of emissions in 2015, 2017 and 2020 by each subregion of China are also presented (Fig. 9). It can be seen that the emission changes during the 2015–2017 were more heterogenous than those during 2018–2020. The air pollutant emissions after the 2018–2020 action plan showed consistent reductions over most regions of China, while there were obvious emission increases detected from 2015 to 2017. This is consistent with the different emission control effects during the two clean air action plans as mentioned in previous sections. Due to its strictest emission control policies, the NCP region showed consistent emission reductions of SO_2, NO_x, CO, $PM_{2.5}$ and PM_{10} during the two clean air action plans. Accordingly, the shares of emissions in the NCP region continued to decrease during the two action plan periods (Fig. 9). For example, the share of SO_2 emissions in the NCP region decreased from 19.4% to 15.4% during the period of 2015–2017, and from 15.4% to 12.7% during the 2018–2020 action plan. In contrast, NMVOC emissions increased obviously over the NCP region from 2015 to 2017, and decreased during 2018–2020. However, its share did not change significantly, being roughly 20% throughout both periods. As for other regions, increases of SO_2, NO_x, $PM_{2.5}$, PM_{10} and NMVOC emissions during 2015–2017 could be found over the Central region. More specifically, the emission increases were mainly located in the Fenwei Plain area of the Central region, which was due to the fact that this area was not included as a key region of emission controls during the 2013–2017 action plan. However, the Fenwei Plain area was added as a key emission control region during the 2018–2020 action plan, which is consistent with the emission reductions for these species over the Central region (Fig. 8). As a result, the shares of SO_2 and $PM_{2.5}$ emissions in the Central region increased during 2015–2017 but decreased during 2018–2020 (Fig. 9). However, the shares of NO_x, PM_{10} and NMVOC emissions continued to increase over the Central region during the two clean air action plans, which suggests larger roles of air pollutant emissions in that region. In contrast, the share of CO emissions in the Central region continued to decrease in the two action plans, from 17.7% in 2015 to 13.4% in 2020.

In terms of the shares of emissions in eastern and western China, the top-down estimation suggests an increased share of NO_x, $PM_{2.5}$, PM_{10} and NMVOC emissions in western China after the two clean air action plans (Fig. 9), which indicates slower emission reductions for these species in western China. However, the share of CO emissions in western China was reduced after the two clean air action plans. Although the share of SO_2 emissions in western China increased during 2015–2017, it turned to a decrease during 2018–2020.

4.3 Comparisons with different emission inventories

In this section, the CAQIEI is compared with the previous long-term bottom-up and top-down emission inventories in China to validate our inversion results and provide the clues for the potential uncertainty in the current air pollutant emission inventories. The bottom-up emission inventories used in the comparison include MEIC (Zheng et al., 2018), ABaCAS (Li et al., 2023), HTAPv3 (Crippa et al., 2023), EDGARv6 (Jalkanen et al., 2012) and CEDS (Mcduffie et al., 2020), while the top-down emission inventory is obtained from the updated Tropospheric Chemistry Reanalysis (TCR-2) (Miyazaki et al., 2020b). However, it is difficult to directly compare our inversion results with these emission inventories considering that the inversion emission includes both anthropogenic and natural emissions. To better compare our inversion results with previous inventories, the natural emission sources, including soil NO_x emissions and biogenic emissions obtained from the CAMS global emission inventory (https://ads.atmosphere.copernicus.eu/cdsapp#!/dataset/cams-global-emission-inventories?tab=overview; last accessed 26 July 2023) and the biomass burning emissions obtained from the Global Fire Assimilation System (GFAS) (Kaiser et al., 2012) are taken as a reference to account for the influences of natural sources. The CAMS and GFAS emission inventory

705 are used because they are state-of-art natural emission inventories and can provide us with independent long-term estimations

706 of natural emissions. Since the latest year of most emission inventories is 2018, the comparisons were conducted between 2015

707 and 2018. Note that due to the complexity in the estimations of natural sources, significant uncertainty exists in the estimated

708 natural emissions. As a result, the comparison results would be sensitive to the used natural emission inventories, especially

709 for the species with large amount of natural emission, such as the NMVOC and particulate matter. Therefore, it should be

710 aware of that the comparison conducted here and the derived implications are on the basis of the natural emissions estimated

711 by CAMS and GFAS. In addition, the natural dust emissions are not considered in the comparisons, which would influence

712 the comparisons of the PM emissions.

713 **4.3.1 Magnitude**

714 **4.3.1.1 NO$_x$**

715   Figure 10 shows the average emissions of different air pollutants in China during 2015–2018 obtained from CAQIEI and

716 the previous emission inventories plus the natural sources we considered. Comparisons of the emission estimations on the

717 regional scale and gridded scale are also presented (Fig. 11 and Fig. S9). The results show that the CAQIEI has slightly higher

718 NO$_x$ emissions in China than the other inventories. Considering that CAQIEI includes both anthropogenic and natural sources,

719 this discrepancy could be explained by the natural NO$_x$ sources. According to the estimations of CAMS and GFAS, the soil

720 and biomass-burning NO$_x$ emissions are approximately 1.9 and 0.08 Tg/yr, which explains well the higher NO$_x$ emissions

721 given by CAQIEI. After consideration of the natural sources, MEIC, HTAPv3 and EDGARv6 agree well with our inversion

722 results on the national scale, with their differences within 1.0–7.4%. The NO$_x$ emission estimated by ABaCAS, CEDS and

723 TCR-2 are slightly lower than CAQIEI and other emission inventories. However, the differences between CAQIEI and these

724 inventories were found to range from 15.9% to 21.3%, which is within the previous estimated uncertainties of NO$_x$ emissions

725 in China (Kurokawa and Ohara, 2020; Li et al., 2017b; Li et al., 2023). These results suggest that the total NO$_x$ emissions in

726 CAQIEI are generally consistent with the current estimations of the anthropogenic and natural NO$_x$ emissions in China. On

727 the regional scale, the top-down estimated NO$_x$ emissions show good agreement with the previous emission inventories over

728 the NCP and SE regions, with their differences ranging from 1.0%–26.8%, suggesting good consistency in the estimations of

729 NO$_x$ emissions over these two regions. This makes sense because NCP and SE are the two most developed regions in China,

730 and where surveys and research on emissions are most sufficient. The differences are larger over the other regions. In the NE

731 region, CAQIEI has higher NO$_x$ emissions than the other inventories by 5–70%, suggesting higher anthropogenic or biomass-

732 burning emissions over there. The estimations made by MEIC, CEDS and TRC-2 are closer to our estimates, with their

733 differences being approximately 5.4–23.3%, while the differences are larger for ABaCAS, HTAPv3 and EDGARv6 (36.7–

734 70.0%). Over the SW and Central regions, there are large diversity in the previous emission inventories with estimations by

735 HTAPv3 and EDGARv6 almost double those of MEIC, ABaCAS, CEDS and TCR-2. The CAQIEI suggests a midst estimation

736 which is within the range of previous emission inventories. In the NW region, CAQIEI is consistently higher than other

737 inventories, by 22.7–64.2%, which suggests a potential missing source of the NO$_x$ emissions over this region.

738 **4.3.1.2 SO$_2$**

739   For SO$_2$ emissions, since natural sources contribute little (only about 0.02 Tg/yr) to them in China, the discrepancies

740 between CAQIEI and previous emission inventories are mainly attributable to the differences in anthropogenic emissions. As

741 shown in Fig. 10, CAQIEI agrees well with HTAPv3 and CEDS on the national scale, with their differences being

742 approximately ±2%, but is higher than MEIC, ABaCAS and TCR-2 by 17.4–32.9%. In contrast, EDGARv6 may have a

743 positive bias in its estimated SO$_2$ emissions, which are roughly double those of CAQIEI and other inventories. On the regional

744 scale, our results agree well with MEIC, ABaCAS, HTAPv3, CEDS and TCR-2 over the NCP region, with their differences

745 ranging from 1.0 to 18.1%. In the SE region, CAQIEI suggest lower SO$_2$ emissions than previous emission inventories, except

746 TCR-2. The differences are relatively smaller for the MEIC and ABaCAS inventories by around −15%, but larger for HTAPv3,

747 EDGARv6 and CEDS (ranging from −47.3% to −113.2%). In contrast, CAQIEI suggests higher SO_2 emissions than all

748 previous emission inventories over the NE region by about 14.8–132.0%, indicating a possible missing sources over there.

749 Similarly, the CAQIEI and HTAPv3 suggests higher SO_2 emissions than the MEIC, ABaCAS, CEDS and TCR-2 by 27.0–

750 75.6% in the NW region, and by 44.3–77.7% in the Central region.

4.3.1.3 CO

752   For CO emissions, CAQIEI is substantially higher than the previous emission inventories, with the estimated CO

753 emissions of CAQIEI being about three times higher than the bottom-up inventories and more than double those of the top-

754 down estimates made by TCR-2. According to GFAS, the average rate of CO biomass-burning emissions in China from 2015

755 to 2018 was about 3.4 Tg/yr. Yin et al. (2019), based on MODIS fire radiative energy data, also estimated China's CO biomass-

756 burning emissions to be about 5.0 (2.3–7.8) Tg/yr. The biogenic CO emissions obtained from the CAMS global emission

757 inventory were approximately 2.3 Tg/yr. According to these estimates, natural CO emissions in China have a magnitude of

758 about 10^1, which is rather small compared with anthropogenic sources, and cannot explain the large discrepancies between

759 CAQIEI and other inventories. Thus, the CAQIEI suggest much higher anthropogenic CO emissions in China than the existing

760 emission inventories. In fact, the potential underestimation of CO anthropogenic emissions has been investigated in previous

761 studies and is regarded as the main reason for the negative bias in global or hemispheric CO simulations (Stein et al., 2014;

762 Gaubert et al., 2020). Regionally, Kong et al. (2020) compared a suite of 13 modeling results from six different CTMs—

763 namely, NAQPMS, CMAQ, WRF-Chem, NU-WRF, NHM-Chem and GEOS-Chem—with observations over the NCP and

764 Pearl River Delta regions under the framework of the Model Inter-Comparison Study for Asia III (MICS-Asia III), and found

765 consistent negative biases in the CO simulations of all models, pointing toward potential underestimations of CO emissions in

766 China. Previous inversion studies have also reported higher a posteriori CO emissions than their *a priori* emission inventories

767 (Bergamaschi et al., 2000; Miyazaki et al., 2012; Petron et al., 2002; Petron et al., 2004; Tang et al., 2013; Gaubert et al., 2020).

768 For example, the constrained CO emissions reported by Gaubert et al. (2020) are 80% higher than the CEDS over the northern

769 China. Our inversion results are consistent with these inversion studies, suggesting higher anthropogenic CO emissions in

770 China. However, direct evidence in support of such high CO emissions in China reported by our study is still limited currently.

771 Thus, we compiled more inversion results within the period of 2013–2020 from previous studies to further validate our

772 inversion results, which are summarized in Table 6. It can be clearly seen that there are large differences in the estimated CO

773 emissions between the inversion results based on surface observations and those based on satellite data. Our inversion results

774 are consistent with the results of Feng et al. (2020), with China's CO emissions in December 2017 estimated at approximately

775 1500.0 kt/day and 1388.1 kt/day, respectively. In addition, Feng et al. (2020) used the CMAQ model to constrain CO emissions,

776 which is different from the model we used. This may indicate that the model uncertainty would not significantly influence the

777 inversion results of CO emissions. However, the top-down estimated CO emissions based on satellite data (163.6–553.4 kt/day)

778 are much lower than those based on surface observations, although they are all higher than their *a priori* emissions. The lower

779 CO emission estimations based on satellite data assimilation may be attributable to the lower sensitivities of satellite data to

780 surface concentrations, suggesting that the assimilation of satellite data alone may not be adequate to correct the negative

781 biases in the *a priori* emissions. This deficiency has also been revealed by Miyazaki et al. (2020b), who found undercorrected

782 surface CO emissions in the extratropic of the Northern Hemisphere in TCR-2. However, the assimilation of surface

783 observations can be influenced by the uncertainties in the modeled vertical mixing, which could lead to the uncertainties in the

784 inversed CO emissions based on surface observations. Therefore, the inversed CO emissions in CAQIEI could be partly

785 supported by previous inversion studies based on surface observations, but more evidence is still needed to justify the

786 magnitude of the inversed CO emissions. Besides anthropogenic sources, the chemical production of CO via oxidation of

787 methane (CH_4) and NMVOCs, as well as the CO sinks via the hydroxyl radical (OH) reaction, also influence the simulation

788 of CO (Stein et al., 2014; Gaubert et al., 2020; Müller et al., 2018). Due to the important role of OH in the chemical production
789 and sinks of CO, the inversion of CO emissions is sensitive to the modeled OH abundance and the emissions of CH_4 and
790 NMVOCs. According to the estimation of Müller et al. (2018), the magnitude of inversed CO emissions in China could differ
791 by more than 40% when different levels of OH concentrations are used in the model. Thus, the much higher estimations of
792 CO emissions in our inversion results may also be partly explained by the underestimation of CO chemical production or the
793 overestimation of the CO sink.

4.3.1.4 PM$_{2.5}$

795   In terms of $PM_{2.5}$, the CAQIEI suggests higher emissions than ABaCAS, HTAPv3 and EDGARv6 by about 20%, and by
796 47.7% than MEIC on the national scale. Larger discrepancies mainly occur in the NE and NW regions, where CAQIEI is about
797 27.2–114.9% and 83.2–143.2% higher than the previous inventories. The differences in the estimated $PM_{2.5}$ emissions may be
798 related to the uncertainties in the biomass-burning or anthropogenic sources in the NE region (Wu et al., 2020b), while in the
799 NW region, the errors in the fine-dust emissions may also contribute to the differences in the estimated $PM_{2.5}$ emissions there.
800 The differences in the estimated $PM_{2.5}$ emissions are relatively smaller in the NCP and SE regions, ranging from −18.9% to
801 20.4%, suggesting better agreement in the estimated $PM_{2.5}$ emissions over these two regions. In the SW region, CAQIEI is
802 closer to HTAPv3 and EDGARv6, with their differences being about 6.3% and −9.5% respectively, and is higher than MEIC
803 and ABaCAS by 54.2% and 28.6%, suggesting higher uncertainty in the estimated $PM_{2.5}$ emissions over there.

4.3.1.5 PM$_{10}$

805   For PM_{10} emissions, it is difficult to directly compare CAQIEI with previous emission inventories since CAQIEI not only
806 contains anthropogenic and biomass-burning emissions, but also coarse-dust emissions. As a result, the estimated emissions
807 of PM_{10} by CAQIEI are substantially higher than those by previous inventories, especially over the NW, Central and NE
808 regions (Fig. 11), which are the typical natural windblown dust-source regions in China (Zeng et al., 2020). Besides the
809 naturally windblown dust of arid desert regions (Prospero et al., 2002), large amounts of coarse-dust emissions also stem from
810 anthropogenic sources, including anthropogenic fugitive, combustion and industrial dust from urban sources (AFCID) (Philip
811 et al., 2017), and anthropogenic windblown dust from human-disturbed soils due to changes in land-use practices, deforestation
812 and agriculture (Tegen et al., 1996). Therefore, although the other regions are not typical natural windblown dust-source
813 regions in China, there are still high levels of coarse -dust emissions from anthropogenic sources there (also called "urban
814 dust"), which may be the main reason for the large deviation in the estimated PM_{10} emissions between CAQIEI and previous
815 inventories. On the one hand, although AFCID is included in MEIC, ABaCAS, HTAPv3 and EDGARv6, it is difficult for
816 current bottom-up emission inventories to completely represent fugitive sources (Philip et al., 2017). On the other hand, the
817 anthropogenic windblown dust emissions haves not been included in current bottom-up emission inventories, which is an
818 important source of coarse dust in urban areas according to the estimations of Li et al. (2016) and the another important
819 contributor to the differences between CAQIEI and previous emission inventories.

4.3.1.6 NMVOCs

821   For NMVOC emissions, since CAQIEI includes both anthropogenic and natural sources, its estimated NMVOC emissions
822 are much higher than those estimated by previous emission inventories. After consideration of natural sources, the CAQIEI
823 suggests close estimations of the NMVOC emissions with the MEIC, HTAPv3 and CEDS inventories on the national scale,
824 with their differences being about 1.5–12.5%. The estimated NMVOC emission by ABaCAS and EDGARv6 are slightly lower
825 than CAQIEI by 17.8% and 24.6%, respectively. On the regional scale, the CAQIEI suggests higher NMVOC emissions over
826 the northern China (NCP, NE and NW), with the top-down estimated NMVOC emissions about 30.4–81.4%, 27.3–72.1%,
827 79.3–116.8%, and 8.7–57.5% higher than those of the previous emission inventories. In contrast, the CAQIEI suggests lower

828 NMVOC emissions over the SE region, with the estimated NMVOC emissions of CAQIEI being about 21.2–27.6% lower

829 than those of MEIC, ABaCAS, HTAPv3 and CEDS. These results are consistent with the previous inversion results based on

830 the satellite observations, which suggest higher NMVOC emissions over the NCP region and lower NMVOC emissions over

831 the south China (Souri et al., 2020). Over the SW region, CAQIEI shows good agreement with MEIC, ABaCAS and CEDS,

832 with CAQIEI being slightly lower than these inventories by 1.0–8.9%, but is lower than HTAPv3 and EDGARv6 by about

833 38.6% and 29.1%, respectively. Again, it should be noted that the comparisons of NMVOC emission are conducted on the

834 basis of natural emissions estimated by CAMS and GFAS, and could be more sensitive to the used natural sources than other

835 species considering the larger contributions of the natural source to the NMVOC emissions.

4.3.2 Seasonality

837 Figure 12 presents the monthly profiles of different air pollutants obtained from different emission inventories. Note that

838 the natural sources have been added to the previous inventories to facilitate the comparisons. The results show that different

839 emission inventories give similar monthly profiles of NO_x and CO emissions, with higher emissions during wintertime and

840 lower emissions during summertime, which suggests relatively lower uncertainty in the estimated monthly profiles for these

841 two species. For SO_2 emissions, CAQIEI yields stronger monthly variation than the other inventories, with a higher proportion

842 from January to March and lower proportion during summertime. Due to the influences of dust emissions, the top-down

843 estimated $PM_{2.5}$ and PM_{10} emissions show higher proportions than the other emission inventories during the spring season,

844 especially for PM_{10}. However, the proportion of emissions during autumn and winter are lower than in the other inventories.

845 The monthly profiles of NMVOC emissions are generally consistent, with higher emissions during summer due to the enhanced

846 biogenic emissions. However, the profile of CAQIEI is flatter than the previous inventories, and suggests a higher proportion

847 during springtime. In addition, the timings of peak values of NMVOC emissions are also different between CAQIEI and the

848 previous inventories, with CAQIEI showing peak values during May–July but the other inventories suggesting peaks during

849 June–August.

4.3.3 Emission changes during 2015–2018

851 The top-down estimated emission changes of different air pollutants during 2015–2018 were also compared with previous

852 emission inventories. Figure 13 shows the time series of the total emissions of different species from 2013 to 2020 obtained

853 from the CAQIEI and other emission inventories. Comparisons of the emission changes over the regional scales are also

854 presented in Fig. S10–S15. Before the comparison, we firstly analyze the trends of natural sources in China to investigate their

855 influences on the emission changes of different species based on the CAMS emission inventory and GFAS. Note that we only

856 consider the soil, biogenic and biomass-burning emissions for the natural sources; the trends of dust emissions in China are

857 not analyzed, which may lead to uncertainty when comparing the emission changes of $PM_{2.5}$ and PM_{10}. As shown in Fig. S16,

858 the natural sources of NO_x and NMVOC emissions changed little during 2013–2018. The other species had small decreasing

859 trends from 2013 to 2018. However, considering the small contributions of natural sources to their emissions, these small

860 trends would not significantly influence their emission trends. For the dust emissions, previous studies have indicated a

861 declining trend in dust activity in China from 2001 to 2020 (Wu et al., 2022; Wang et al., 2021), due to weakened surface wind

862 and increased vegetation cover and soil moisture. These results suggest that the emission trends in the CAQIEI would be

863 mainly driven by the anthropogenic sources for the gaseous air pollutants based on the estimations of CAMS and GFAS, while

864 its estimated emission trends of $PM_{2.5}$ and PM_{10} would be influenced by the declining trends in dust emissions in China, which

865 should be noted when comparing the emission changes of $PM_{2.5}$ and PM_{10}.

866 As shown in Fig. 14, all the emission inventories agree that the NO_x, SO_2, CO, $PM_{2.5}$ and PM_{10} emissions in China were

867 reduced from 2015 to 2018, except for the increases of CO emissions estimated by TCR-2, which confirms the effectiveness

868 of the emission control policies implemented during the clean air action plans. Meanwhile, most emission inventories agree

that SO_2 is the species with the largest emission reduction rate, followed by $PM_{2.5}$, indicating better emission mitigation effects of these two species (Fig. 14). However, the CAQIEI suggested lower emission reduction rates than the other emission inventories for most species, especially for NO_x, PM_{10} and NMVOCs (Fig. 14). The estimated emission reduction rate of NO_x obtained from CAQIEI is about −2.7%, which is lower than the values of MEIC (−9.7%), ABaCAS (−23.0%), HTAPv3 (−13.0%) and CEDS (−9.0%). As we discussed in Sect. 4.2.2.2, the small reductions of NO_x emission in CAQIEI would be related to the increased vehicle emissions and the undesirable mitigation effects of the industry control. In fact, these factors have been considered in some bottom-up emission inventories, such as MEIC. The differences between our inversion results and previous inventories thus reflect uncertainty in the quantifications of the effects of these factors on the NO_x emissions due to the lack of sufficient statistics on mobile vehicle or other sectors. Our inversion results suggest larger adverse effects of these two factors on the reductions of NO_x emissions in China. According to Fig. S17, the differences between CAQIEI and these inventories mainly occur in the SE, SW, NW and Central regions, with the emission reduction rate estimated by CAQIEI being substantially lower than those estimated by previous inventories. In particular, CAQIEI suggests increases of NO_x emissions over the Central region, which is opposite to the previous emission inventories. Better agreement is achieved over the NCP and NE regions, with the emission reduction rate estimated by CAQIEI being closer to those of MEIC, HTAPv3 and CEDS. The NO_x emission reduction rates estimated by EDGARv6 (−3.3%) and TCR-2 (−1.7%) are closer to our results on the national scale, but they estimated lower NO_x emission reduction rate than our estimate over the NCP and NE regions.

Similarly, the emission reduction rate of PM_{10} obtained from CAQIEI (−10.8%) is lower than those estimated by MEIC (−27.9%), ABaCAS (−33.0%) and HTAPv3 (−27.8%) on the national scale (Fig. 14). A lower PM_{10} emission reduction rate of CAQIEI than these inventories also exist in the different regions of China, except SW (Fig. S17). In particular, different from previous emission inventories, CAQIEI suggests that PM_{10} emissions may have actually increased over the Central region. Considering that dust emissions may have decreased from 2015 to 2018 owing to weakened dust events (Wang et al., 2021), the increase in PM_{10} emissions over the Central region may reflect the increases in anthropogenic sources. Meanwhile, we also found that CAQIEI estimated the emission reduction rate of PM_{10} to be smaller than that of $PM_{2.5}$. This is different from previous emission inventories, which show similar emission reduction rates for $PM_{2.5}$ and PM_{10}. Considering that PM_{10} emissions include $PM_{2.5}$ and PMC emissions, the lower emission reduction rate of PM_{10} than $PM_{2.5}$ in CAQIEI suggests that PMC emissions may have decreased slower than $PM_{2.5}$ emissions from 2015 to 2018.

In terms of NMVOCs, most previous inventories, including MEIC, EDGARv6 and CEDS, suggest a weak decrease in China, with the estimated rates of change in emissions ranging from −0.8% to −4.6%. The emission reduction rate estimated by ABaCAS is larger, reaching up to −14.2%. In contrast, the CAQIEI suggests an opposite emission change to these inventories, with estimated NMVOC emissions increasing by 26.6% from 2015 to 2018. HATPv3 also suggests an increase in NMVOC emissions, but with a much lower rate of increase (2.7%). Similar results could also be found on the regional scale (Fig. S17), especially over the NCP, NE and Central regions, where NMVOC emissions could have increased by 38.0%, 38.3% and 60.0%, respectively, according to the estimates of CAQIEI. As we discussed in Sect. 4.2.2.2, the increases of NMVOC emission estimated in CAQIEI may be related to the increased anthropogenic NMVOC emissions from the chemical industry, solvent use, and vehicles. Therefore, similar to the NO_x emissions, the differences between CAQIEI and previous inventories reflects the uncertainty in the quantifications of the impacts of these factors, and suggest larger adverse effects of these factors on the emission reductions of NMVOC emission than the previous inventories.

The differences in the estimated emission reduction rates between CAQIEI and previous inventories are relatively smaller for SO_2 and $PM_{2.5}$ emissions. The emission reduction rate of SO_2 estimated by CAQIEI is close to that estimated by MEIC and CEDS, ranging from −34.7% to −44.3%. ABaCAS and HTAPv3 estimate a larger emission reduction rate of about −58.5% and −53.7%, respectively. EDGARv6 and TCR-2 may underestimate the reduction rate of SO_2, with estimates of only about −7.0% and −9.1%, respectively. This may be because EDGARv6 underestimates the FGD (flue-gas desulfurization devices) penetration or SO_2 removal efficiencies of FGD in China. On the regional scale (Fig. S17), the top-down estimated SO_2

emission reduction rate agrees reasonably with that of MEIC over the NCP, NE and SE regions, but these inventories estimate different SO$_2$ emission reduction rates over the SW, NW, and Central regions. The reduction rates estimated by MEIC over the SW and Central regions is higher than those given by CAQIEI, but lower over the NW region. The other emission inventories also give different emission reduction rates, suggesting large uncertainty in the estimated SO$_2$ emission reduction rates over these three regions. In terms of PM$_{2.5}$, CAQIEI's estimated emission reduction rate agrees well with those of MEIC and HTAPv3 on the national scale, which is about 24–27% from 2015 to 2018. The emission reduction rate of PM$_{2.5}$ estimated by EDGARv6 are lower than our estimates and other inventories, which were about 9%. On the regional scale, our results show good consistency with MEIC and HTAPv3 over the NCP, NE, SE and SW regions, but they have large differences over the NW and SW regions.

Different from the other species, the CO emission reduction rate estimated by CAQIEI (−21.3%) is higher than in most of the previous inventories, including MEIC (−13.0%), ABaCAS (−11.6%), EDGARv6 (−4.7%), and CEDS (−11.7%), suggesting larger mitigation effects on CO emissions than other inventories. HTAPv3 agrees with our results, with an estimated emission reduction rate of about −22.0%. On the regional scale (Fig. S17), our result is consistent with MEIC over the NCP and SE regions, with estimated emission reduction rates for CO of around 24% and 15%, respectively, while in other regions the emission reduction rate estimated by CAQIEI is higher than that estimated by MEIC. The TCR-2 shows opposite changes in CO emissions compared with the other inventories insofar as it suggests increases of CO emissions over different regions of China. Since the emissions in TCR-2 are constrained by satellite observations, the differences between our results and those of TCR-2 highlight that the observations used to constrain the emissions may have a large influence on the estimated emission changes. In this case, the estimated changes of CO emissions by CAQIEI are more consistent with those estimated by other bottom-up inventories. Considering this, the TCR-2 may have uncertainties in its estimated changes of CO emissions in China from 2015 to 2017, which could be related the suboptimal performance of the data assimilation caused by the underestimated background errors of CO or too short assimilation window for the CO emission estimates (Miyazaki et al., 2020)In this case, the assimilation of surface observations (our study) is shown to be superior to the assimilation of satellite observations (TCR-2), as our results are more consistent with other bottom-up inventories.

4.4 Uncertainty estimation of CAQIEI

Finally, the uncertainty of the inversed emission inventory product is estimated in this section to facilitate users' understanding of the data's accuracy. Within the framework of EnKF, the analysis perturbation $\mathbf{X}^a$ estimated by using Eq. (3) could provide the information regarding the uncertainty of the inversed emission inventory. The Coefficient of variation (hereinafter, CV), defined as the standard deviation divided by the average, with a larger value denoting higher uncertainty, is calculated based on the analysis perturbation to measure the uncertainty of the inverse emission inventory. Based on this method, the uncertainty (CV) of the a posteriori emission was estimated as follows: 92.3% (PM$_{2.5}$), 88.8% (PM$_{10}$), 26.7% (SO$_2$), 46.8% (CO), 31.8% (NO$_x$) and 65.5% (NMVOC). However, it should be noted that such uncertainty was only calculated under the framework of the EnKF constructed in this study, which is dependent on the assigned value of the a priori emission uncertainty, observation errors and the number of assimilated observations. In addition, we only considered the a priori emission uncertainty and the observation errors during the inversion. The influences of the other error sources, such as uncertainty in the chemistry transport model, meteorology simulations and the inversion method were not considered. Therefore, the current estimated uncertainty should be considered as a lower bound for the real uncertainty. More systematic analysis that thoroughly consider the uncertainty sources regarding the emission inversion should be conducted in future to give a more accurate estimation of the uncertainty in our products.

5 Discussion and conclusion

A long-term, top-down emissions inventory of major air pollutants in China was developed and validated in this study by assimilating surface observations from CNEMC using the modified EnKF method and NAQPMS. It includes gridded emission maps of NO_x, SO_2, CO, primary $PM_{2.5}$, primary PM_{10}, and NMVOCs in China from 2013 to 2020, on a monthly basis, with a horizontal resolution of 15 km × 15 km. This new top-down emissions inventory, named CAQIEI, provides new insights into the air pollutant emissions and their changes in China during the country's two clean air action periods. The estimated total emissions for the year 2015 in China are 25.2 Tg of NO_x, 17.8 Tg of SO_2, 465.4 Tg of CO, 15.0 Tg of $PM_{2.5}$, 40.1 Tg of PM_{10} and 46.0 Tg of NMVOCs. Comparisons of CAQIEI with previous inventories, including MEIC, ABaCAS, HTAPv3, EDGARv6, CEDS and TCR-2, on the basis of the natural emissions obtained from CAMS and GFAS showed reasonable agreement for the estimation of NO_x, SO_2 and NMVOC emissions in China. The $PM_{2.5}$ emissions obtained from CAQIEI (13.2 Tg) are slightly higher than in the previous emission inventories (8.3–11.1 Tg), while the CO emissions estimated by CAQIEI (426.8 Tg) are substantially higher than in previous inventories (120.7–237.7 Tg). However, the reasons for such a large gap are still not clear, but might be attributable to both the underestimation of CO sources (e.g., anthropogenic, biomass-burning and chemical-production sources) ~~according to previous model simulation and inversion studies~~ (Bergamaschi et al., 2000; Miyazaki et al., 2012; Petron et al., 2002; Petron et al., 2004; Tang et al., 2013; Gaubert et al., 2020), and/or the overestimation of CO sinks in the model (Müller et al., 2018). In addition, comparisons with previous inversion studies suggest there are larger differences in the top-down estimated CO emissions based on surface and satellite observations. Our inversion results are consistent with previous inversions based on surface observations, but are much higher than those based on satellite observations, suggesting large uncertainty in inversion-estimated CO emissions in China. Therefore, more research is needed to better understand the reasons behind the negative biases in CO simulation, and to explain the differences between our results and those of previous inventories. Similar to situation with CO emissions, the PM_{10} emissions estimated by CAQIEI (37.7 Tg) are also substantially higher than in previous inventories (11.1–15.9 Tg). However, this will be mainly associated with the emissions of coarse dust, which were not included in previous inventories. The estimation of dust emissions in China is subject to high levels of uncertainty, with the estimated dust fluxes based on different dust emission schemes differing by several orders of magnitude (Zeng et al., 2020). Therefore, our inversion results could provide a reference for the magnitude of coarse-dust emissions in China, which could then help to reduce the large uncertainty in estimations of dust emissions in China.

Several potential important deficiencies in current emission estimations were also indicated by CAQIEI on the regional scale. For example, the CAQIEI suggests substantially higher air pollutant emissions than the previous emission inventories over the NW and Central regions. Thus, the air pollutant issues may be more severe than we expected over these two regions. Meanwhile, our inversion results suggest higher NMVOC emissions over the northern China but suggest lower NMVOC emissions in southern China, which is consistent with the previous inversion studies based on the satellite. China is now facing increasingly severe O_3 pollution and has an urgent need for a coordinated control of O_3 and $PM_{2.5}$. Our results may provide valuable information on the NMVOC emissions in China, which is important for a proper understanding of O_3 pollution and the development of effective control strategies nationally. Higher emissions were also found in the NE region based on our inversion results. The NE region is a typical area for open-area biomass burning, with significant emissions from straw combustion (Wu et al., 2020b). The higher emissions estimated by our inversion result may indicate higher biomass-burning emissions over there. This is consistent with recent estimations of biomass-burning emissions by Xu et al. (2023) and Wu et al. (2020b), who showed higher biomass-burning emissions in China than previous estimations, including those of GFEDv4.1s (https://www.globalfiredata.org/data.html), FINNv1.5 (https://www.acom.ucar.edu/Data/fire/), and GFASv1.2 (https://www.ecmwf.int/en/forecasts/dataset/global-fire-assimilation-system).

Based on CAQIEI, we further quantified the emission changes of different air pollutants in China during the two clean air action plans. The results confirmed the effectiveness of these campaigns on the mitigation of air pollutant emissions in China, with estimated emission reductions of 15.1% for NO_x, 54.5% for SO_2, 35.7% for CO, 44.4% for $PM_{2.5}$, and 33.6% for

994   PM_{10} from 2015 to 2020. In contrast, NMVOC emissions increased by 21.0% from 2015 to 2020. Comparisons of the estimated
995   emission reduction rates during the two clean air action plans suggested that emission reductions were larger during the 2018–
996   2020 than during 2015–2017. The estimated rates of change in emissions were 5.9% for NO_x, −23.8% for SO_2, −9.8% for CO,
997   −14.5% for $PM_{2.5}$, −7.2% for PM_{10}, and 27.6% for NMVOCs during 2015–2017, which were smaller than the −12.1% for NO_x,
998   −23.5% for SO_2, −18.3% for CO, −26.6% for $PM_{2.5}$, −25.5% for PM_{10}, and −4.5% for NMVOCs during 2018–2020. On the
999   one hand, this is due to the fact that more sectors were controlled during the 2018–2020 action plan. Besides the industrial and
1000   power sectors, which were the main points of control in the 2013–2017 action plan, the residential sector, transportation sector,
1001   and non-point sources like blowing-dust emissions, were also strengthened in the 2018–2020 action plan. Consequently, the
1002   emission reduction rates of CO, $PM_{2.5}$ and PM_{10} during 2018–2020 were higher than those during the 2015–2017 when the
1003   2013–2017 action plan was implemented. However, the reduction of SO_2 emissions was similar during the two action plan
1004   periods. This is because most SO_2 emissions stem from the industrial sector and power plants, which together contribute about
1005   77% of all emissions (Zheng et al., 2018). Thus, the additional control of other sectors in the 2018–2020 action plan may not
1006   have significantly impacted the mitigation of SO_2 emissions. On the other hand, strict emission controls were implemented or
1007   strengthened in more areas of China during the 2018–2020 action plans. For example, the inversion results indicated that there
1008   were obvious increases of SO_2, NO_x, $PM_{2.5}$, PM_{10} and NMVOC emissions during 2015–2017 over the Central region,
1009   especially in the Fenwei Plain area, where the emission controls were relatively weak during the 2013–2017 action plan.
1010   However, all species showed obvious emission reductions almost the whole China during the 2018–2020 action plan.

1011   The estimated rates of change in emissions during 2015–2018 were also compared with those estimated by previous
1012   emission inventories. Although both CAQIEI and previous inventories showed declines of air pollutant emissions in China,
1013   the emission reduction rates estimated by CAQIEI were generally smaller than those estimated by previous inventories,
1014   especially for NO_x, PM_{10} and NMVOCs, suggesting a smaller mitigation effects of the air pollution control measures than the
1015   previous emission inventories suggested. In particular, China's NMVOC emissions were shown to have increased by 26.6%
1016   from 2015 to 2018, especially over NCP (38.0%), NE (38.3%) and Central (60.0%). CO was found to be an exception insofar
1017   as the emission reduction rate estimated by CAQIEI was larger than that of most previous emission inventories, except in the
1018   NCP region. The estimated emission reduction rates of SO_2 and $PM_{2.5}$ were relatively closer to those of previous inventories,
1019   suggesting better consistency in the estimated emission reduction for these two species.

1020   Overall, the inversion inventory developed in this study could provide us with value information on the complex variations
1021   of air pollutant emissions in China during its two recent clean air action periods, which could help improve our understanding
1022   of air pollutant emissions and related changes in air quality in China. For example, the increases of O_3 and nitrate
1023   concentrations may be associated with the undesirable emission reduction effects of the 2013–2017 action plans. The estimated
1024   lower NO_x emission reduction rate by CAQIEI may also help explain the weak responses of nitrogen deposition fluxes to the
1025   clean air action plans. Meanwhile, this top-down emissions inventory can be used to supply the input data for CTMs or server
1026   as a comparable reference for future inversion studies based on other methods or observation data, which is expected to
1027   improve the performance of model simulations and air quality forecasts, and facilitate the development of inversion method.

6 Limitations

1029   However, due to the complexity of the emission estimation, it is inevitable that there are some limitations in our inversion
1030   results. Here We summarise some issues that might affect the quality of the CAQIEI which were known at the time of
1031   publication to assist the potential users in properly using this data products.
1032   (1) The changes in the number of observation sites would induce spurious emission trends during 2013–2014, especially
1033   over western China, although the influence of the number of observation sites is smaller over the NCP and SE regions because
1034   of their higher density of observation sites. Therefore, it is recommended that not to use the emissions in 2013 and 2014 when

analyzing the emission trends in China. This limitation makes it difficult to estimate the overall emission control effects of 2013 – 2017 action plan. Consequently, the emission change rate during the 2015–2017 were sampled in this study to represent the emission control effects of the 2013–2017 action plan, but it may not necessarily reflect the overall reduction rate of the action plan for the entire period. In addition, although the number of observation sites has become stable since 2015, the limited number of observation sites makes it difficult to fully constrain China's air pollutant emissions, especially for the natural sources considering that the majority of the observation sites are located in the urban areas. Therefore, the uncertainty in the estimated emissions over the remote areas are expected to be higher than those over the urban areas, especially for the species with large amount of natural emission, such as PM and NMVOC. For example, the coarse-dust emissions over western China are expected to be underestimated by CAQIEI because of the limited availability of observation sites. Therefore, adding observations there will help improve the accuracy of the inversion estimates. For example, simultaneous assimilation of the surface and satellite observation may help alleviate this problem and provide more constrains on the emissions without surface observations.

(2) The natural and anthropogenic emissions are not differentiated in our inversion method, leading to higher emissions of PM_{10} and NMVOCs than in other emission inventories. This also hinders the comparisons of our inversion results with the previous inventories. Therefore, potential readers should be aware of that the current comparisons of our inversion results and previous inventories are on the basis of the natural emissions estimated by CAMS and GFAS, which does not necessarily indicate large uncertainties in anthropogenic sources within the bottom-up inventories. The impacts are expected to be smaller for the NO_x, SO_2 and CO due to the small contributions of natural sources to their emission, but would be larger for NMVOC and PM which has large amount of natural emission. Assimilation of isotope data, speciated $PM_{2.5}$ and NMVOC observations may help differentiate the natural and anthropogenic emissions, and address this problem in future.

(3) The NMVOC emissions may have larger uncertainty than the other species. On the one hand, a significant amount of NMVOC emission would originate from suburban or rural regions. Therefore, although the O_3 observations at the urban sites could provide information on the NMVOC emissions over the suburban or rural areas according to covariance estimated by the ensemble simulation, the NMVOC emissions may not be fully constrained due to the lack of observation sites over the suburban or rural areas. On the other hand, due to the lack of long-term NMVOC observations, the NMVOC emissions were constrained by the O_3 concentrations in this study. Although the feasibility of this approach has been demonstrated by previous inversion studies, the nonlinear NO_x-VOC-O_3 interactions could inevitably introduces greater uncertainty into the inversion of NMVOC than other species. Therefore, more attention should be paid while using the inversion results of NMVOC, and more robust analysis of the effects of nonlinear NO_x-VOC-O_3 interactions and the number of observation sites should be performed in future to better illustrate the feasibility of assimilating O_3 to constrain the NMVOC emissions.

(4) The errors in the meteorological simulation and the CTMs were not considered in the emission inversions, which would lead to uncertainty in our estimated emissions. For example, the errors in the simulated wind would influence the transportation of the air pollutant and lead to uncertainty in the emissions distributions. According to the evaluation results of meteorological simulations (Table S1), the simulated relative humidity is generally lower than the observations, which may weaken the formation of secondary aerosol. On the contrary, the simulated precipitation was higher than the observation for most regions which would lead to overestimations of the wet removal of air pollutants. As a result, there may be a positive tendency in the inversed emission inventory due to the errors in the simulated relative humidity and precipitation. Besides these parameters, the accuracy of the simulated boundary layer is also important for the performance of the emission inversions (Du et al., 2020), although it was not evaluated currently due to the lack of observation. If the WRF systematically underestimates the boundary layer, the vertical diffusions of the air pollutants would be suppressed, which would lead to overestimated surface air pollutant concentrations and a negative tendency in the inverse emission inventory. However, it is difficult to consider the meteorological and model errors in the assimilation process. it is difficult to quantify the influences of the meteorological errors on the emission inversions, as the errors in the meteorological simulation and chemical transport

model interact with each other. More comprehensive analysis should be conducted in the future to better understand the impacts of the meteorological and model errors on the inverse emission inventory. A multi-model inversion framework, for example that of Miyazaki et al. (2020a), may help alleviate the influences of model errors on emission inversions in future. Using other models (e.g., WRF-Chem, CMAQ) to validate our inversion inventory could also help us assess the impacts of model uncertainty on the emission inversions. Meanwhile, because of the many uses that require a rapid update of emissions, it may be time to organize an intercomparison study focused on the emission inversions.

(4)(5)   Current inversion emission inventory is mainly assessed by the surface observations and previous emission inventories. more independent observations, such as the satellite observation data, should be used in future to further validate the inversion results of this study and its derived findings. For example, the independent measurements from field campaign or satellite retrievals (e.g., TropOMI CO data) can help validate the reliability of the much higher a posterior CO emissions in CAQIEI than the previous inventories in the future.

7 data availability

The CAQIEI inventory can be freely download at https://doi.org/10.57760/sciencedb.13151 (Kong et al., 2023), which includes monthly grid maps of the air pollutant emissions from 2013 to 2020. The contained species include NO_x, SO_2, CO, primary $PM_{2.5}$, primary PM_{10} and NMVOC. The horizontal resolution is 15km. There are totally 8 Network Common Data Form files (NetCDF), which were named by the date and contains the monthly emissions of different air pollutants in China in each year. The description of the content of each NetCDF file and some important notes when using this dataset are also available in README.txt on the website.

Tables

Table 1. Corresponding relationships between the chemical observations and adjusted emissions

Species	Description	Observations used for inversions of this species
BC	Black carbon	$PM_{2.5}$
OC	Organic carbon	$PM_{2.5}$
PMF	Fine-mode unspeciated aerosol	$PM_{2.5}$
PMC	Coarse-mode unspeciated aerosol	$PM_{10} - PM_{2.5}$
NO_x	Nitrogen oxide	NO_2
SO_2	Sulfur dioxide	SO_2
CO	Carbon monoxide	CO
NMVOCs	Non-methane volatile organic compounds	MDA8h O_3

Table 2. Evaluation statistics of the *a posteriori* (*a priori*) model simulation for different species[a]

	PM$_{2.5}$ (µg/m^3)				PM$_{10}$ (µg/m^3)			
	R	MBE	NMB (%)	RMSE	R	MBE	NMB (%)	RMSE
Hourly	0.77 (0.53)	2.1 (13.3)	4.5 (28.6)	32.4 (55.6)	0.72 (0.44)	−3.7 (−11.5)	−4.6 (−14.3)	53.1 (74.4)
Daily	0.89 (0.61)	2.1 (13.3)	4.4 (28.4)	20.0 (46.3)	0.88 (0.51)	−3.7 (−11.2)	−4.6 (−14.1)	31.6 (62.2)
Monthly	0.94 (0.68)	2.1 (13.3)	4.5 (28.3)	11.7 (32.5)	0.90 (0.56)	−3.6 (−11.3)	−4.5 (−14.1)	21.2 (44.1)
Yearly	0.94 (0.62)	2.2 (11.9)	4.4 (24.3)	9.1 (27.7)	0.89 (0.52)	−3.8 (−13.4)	−4.6 (−16.1)	18.5 (38.7)

	SO$_2$ (µg/m^3)				NO$_2$ (µg/m^3)			
	R	MBE	NMB (%)	RMSE	R	MBE	NMB (%)	RMSE
Hourly	0.64 (0.16)	−1.8 (19.0)	−9.1 (93.8)	24.9 (58.7)	0.67 (0.45)	−1.2 (−0.9)	−3.9 (−2.7)	19.9 (25.5)
Daily	0.80 (0.20)	−1.8 (19.0)	−9.2 (94.5)	16.0 (51.4)	0.80 (0.51)	−1.2 (−0.8)	−3.7 (−2.6)	12.8 (20.1)
Monthly	0.85 (0.20)	−1.9 (18.9)	−9.3 (93.1)	12.4 (45.8)	0.84 (0.57)	−1.2 (−0.8)	−3.8 (−2.6)	9.4 (15.6)
Yearly	0.83 (0.18)	−2.4 (17.0)	−10.8 (75.9)	11.6 (42.4)	0.82 (0.63)	−1.3 (−1.6)	−3.9 (−5.0)	8.1 (13.0)

	CO (mg/m^3)				O$_3$ (µg/m^3)			
	R	MBE	NMB (%)	RMSE	R	MBE	NMB (%)	RMSE
Hourly	0.69 (0.38)	−0.1 (−0.4)	−8.8 (−45.6)	0.6 (0.8)	0.71 (0.51)	5.6 (−8.4)	9.5 (−14.0)	34.9 (41.6)
Daily	0.81 (0.42)	−0.1 (−0.4)	−8.6 (−45.5)	0.4 (0.7)	0.71 (0.40)	5.7 (−8.4)	9.5 (−14.1)	26.1 (33.8)
Monthly	0.83 (0.42)	−0.1 (−0.4)	−8.7 (−45.7)	0.3 (0.7)	0.76 (0.47)	5.6 (−8.4)	9.4 (−14.1)	19.6 (26.0)
Yearly	0.82 (0.27)	−0.1 (−0.5)	−9.0 (−47.6)	0.3 (0.7)	0.53 (0.11)	5.1 (−7.8)	8.7 (−13.4)	14.2 (20.5)

[a] The time series of the air pollutant concentrations at each station were firstly catenated into a single vector. Then the values of each evaluation metric were calculated based on the catenated time series of the observed and simulated concentrations.

Table 3. Inversion-estimated emissions (Tg/yr) of different species in China as well as the six regions for year 2015

	China	NCP	SE	NE	SW	NW	Central
NO_x	25.2	5.1	7.1	4.5	4.2	1.2	3.2
SO_2	17.8	3.5	3.3	4.0	2.6	0.8	3.6
CO	465.4	82.2	106.7	78.7	82.8	32.6	82.3
$PM_{2.5}$	14.9	2.7	3.3	3.1	2.9	1.2	1.9
PM_{10}	40.1	8.7	7.5	8.2	5.5	4.1	6.2
NMVOC	46.0	9.0	13.7	8.5	7.8	2.7	4.2

Table 4. The calculated annual trends of $PM_{2.5}$ and PM_{10} emissions in China based on CAQIEI

	$PM_{2.5}$ (Tg/year)			PM_{10} (Tg/year)		
	2015–2020	2015–2017	2018–2020	2015–2020	2015–2017	2018–2020
China	−1.4*	−1.1	−1.5	−2.6*	−1.4	−4.6
NCP	−0.32*	−0.30	−0.32	−0.64*	−0.88	−0.99
SE	−0.32*	−0.21	−0.44	−0.52*	−0.48	−0.84
NE	−0.24*	−0.25	−0.11	−0.52*	−0.22	−0.73
SW	−0.21*	−0.26	−0.20	−0.40*	−0.26	−0.56
NW	−0.09	−0.08	−0.12	−0.20*	−0.32	−0.32
Central	−0.15	0.01	−0.32	−0.27	−0.32	−1.14

* Trend is significant at the 0.05 significance level

1154 **Table 5. The calculated annual trends of the four gaseous emissions in China based on CAQIEI**

	SO$_2$ (Tg/year)			CO (Tg/year)		
	2015–2020	2015–2017	2018–2020	2015–2020	2015–2017	2018–2020
China	−2.1*	−2.1	−1.3	−36.0*	−22.8	−33.5
NCP	−0.57*	−0.69	−0.21	−8.4*	−4.30	−7.23
SE	−0.34*	−0.39	−0.20	−6.1*	−3.54	−8.37
NE	−0.44*	−0.44	−0.21	−6.2*	−1.74	−3.91
SW	−0.22*	−0.27	−0.17	−3.8*	−2.36	−4.54
NW	−0.08*	−0.08	−0.08	−3.0*	−0.73	−2.95
Central	−0.46*	−0.25	−0.40	−8.7*	−10.14	−6.55

	NO$_x$ (Tg/year)			NMVOC (Tg/year)		
	2015–2020	2015–2017	2018–2020	2015–2020	2015–2017	2018–2020
China	−0.67	0.74	−1.6	1.9	6.3	−1.3
NCP	−0.32	0.05	−0.40	0.66	1.37	−0.42
SE	−0.22	0.18	−0.49	0.50	1.73	−0.24
NE	−0.17	0.03	−0.19	0.03	0.79	−0.49
SW	−0.06	0.10	−0.26	0.23*	0.43	0.03
NW	−0.03	0.11	−0.06	0.10	0.69	−0.27
Central	0.04	0.28	−0.16	0.55*	1.33	0.09

1155 * Trend is significant at the 0.05 significance level

1156
1157
1158
1159
1160
1161
1162
1163
1164
1165
1166
1167
1168
1169
1170
1171
1172
1173
1174
1175
1176
1177
1178

1179 **Table 6 The top-down estimated CO emissions in China from previous inventories**

Reference	Region	Period	Method	Assimilated observation	*A priori* CO emission (kt/day)	*A posteriori* CO emission (kt/day)
Feng et al. (2020)	China Mainland	December 2013	EnKF with CMAQ model	Surface observation	586.4	1678.0
		December 2017			499.3	1388.1
	NCP	December 2013			143.9	394.3
		December 2017			120.5	340.7
Muller et al. (2018)	China	2013	4DVar with IMAGES model	IASI CO observation with different constraints on OH levels	454.8	367.1–553.4
Gaubert et al. (2020)	Central China	May 2016	DART/CAM-CHEM	MOPITT CO observation	193.6	220.3
	North China				93.5	163.6
Jiang et al. (2017)	East China	2013	4DVar with GEOS-Chem	MOPITT CO observation	564.5	439.5–484.4
		2014				430.4–481.1
		2015				397.5–439.7
Zheng et al. (2019)	China	2010–2017 average	Bayesian inversion	MOPITT CO, OMI HCHO, and GOSAT CH_4 observation	-	444.4

1180
1181
1182
1183
1184
1185
1186
1187
1188
1189
1190
1191
1192
1193

1194 **Figures**

1195
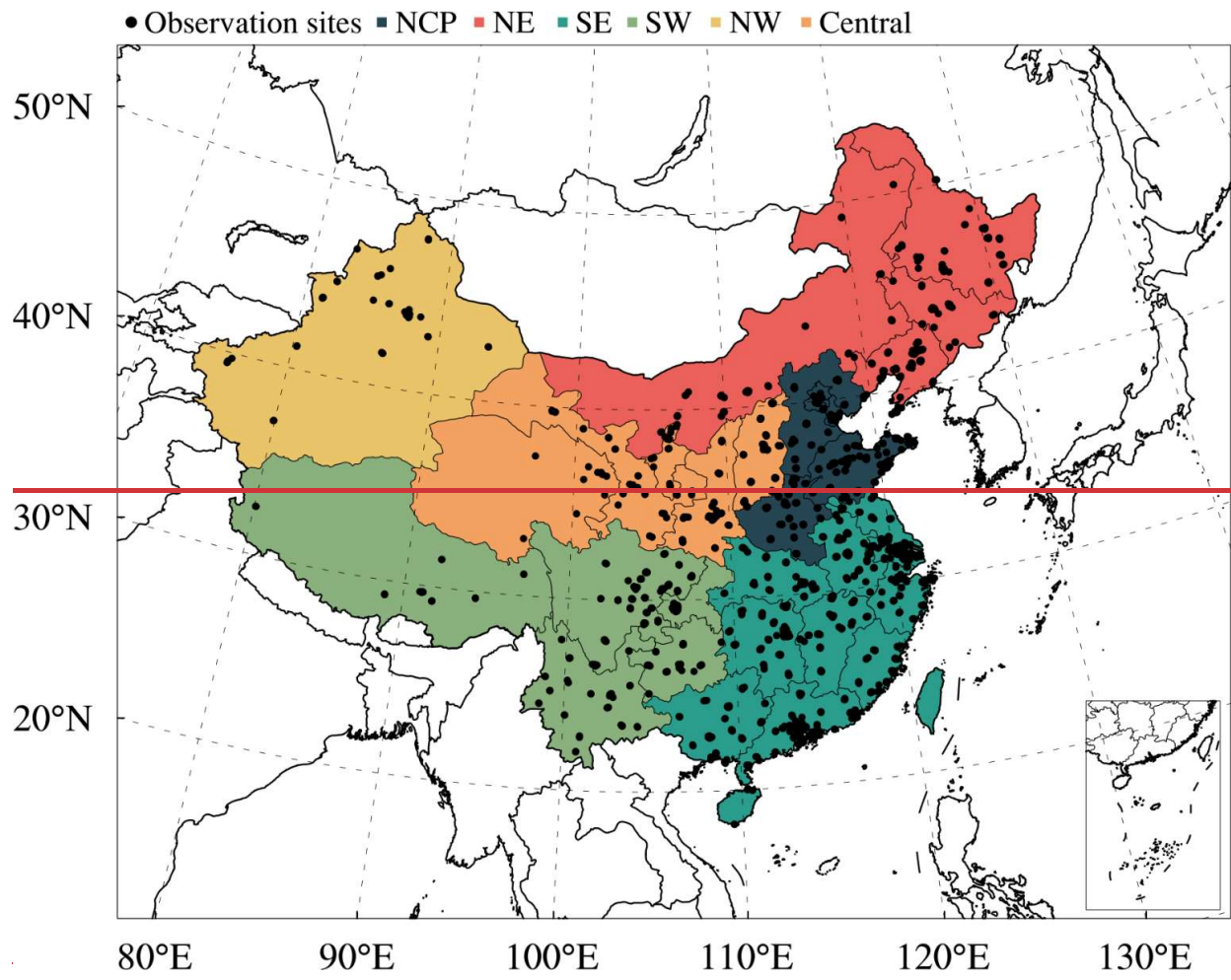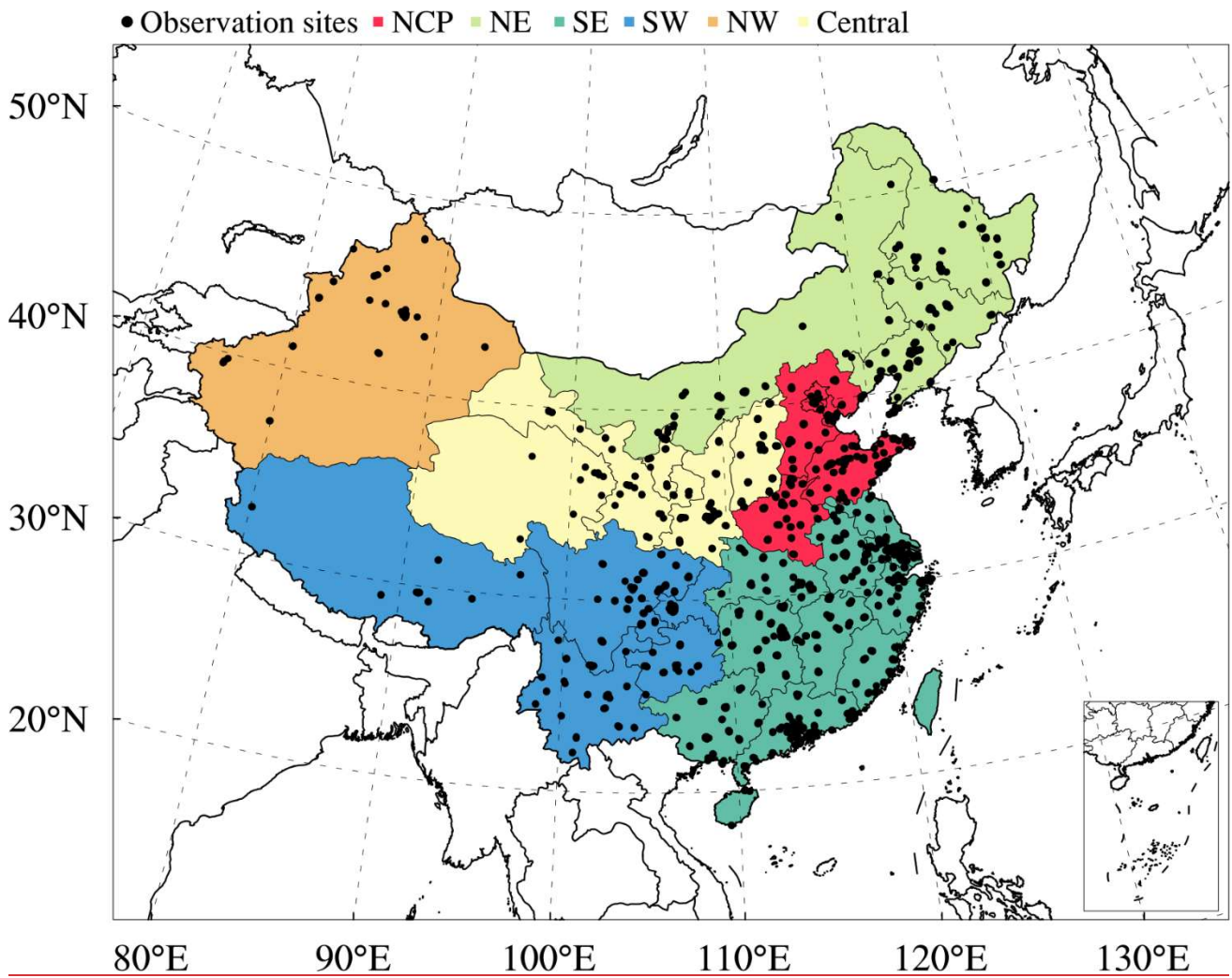
Figure 1: Modeling domain of the ensemble simulation overlaid with the distributions of observation sites from CNEMC. Different colors denote the different regions in mainland China—namely, the North China Plain (NCP), Northeast China (NE), Southwest China (SW), Southeast China (SE), Northwest China (NW) and Central China (Central).

1203
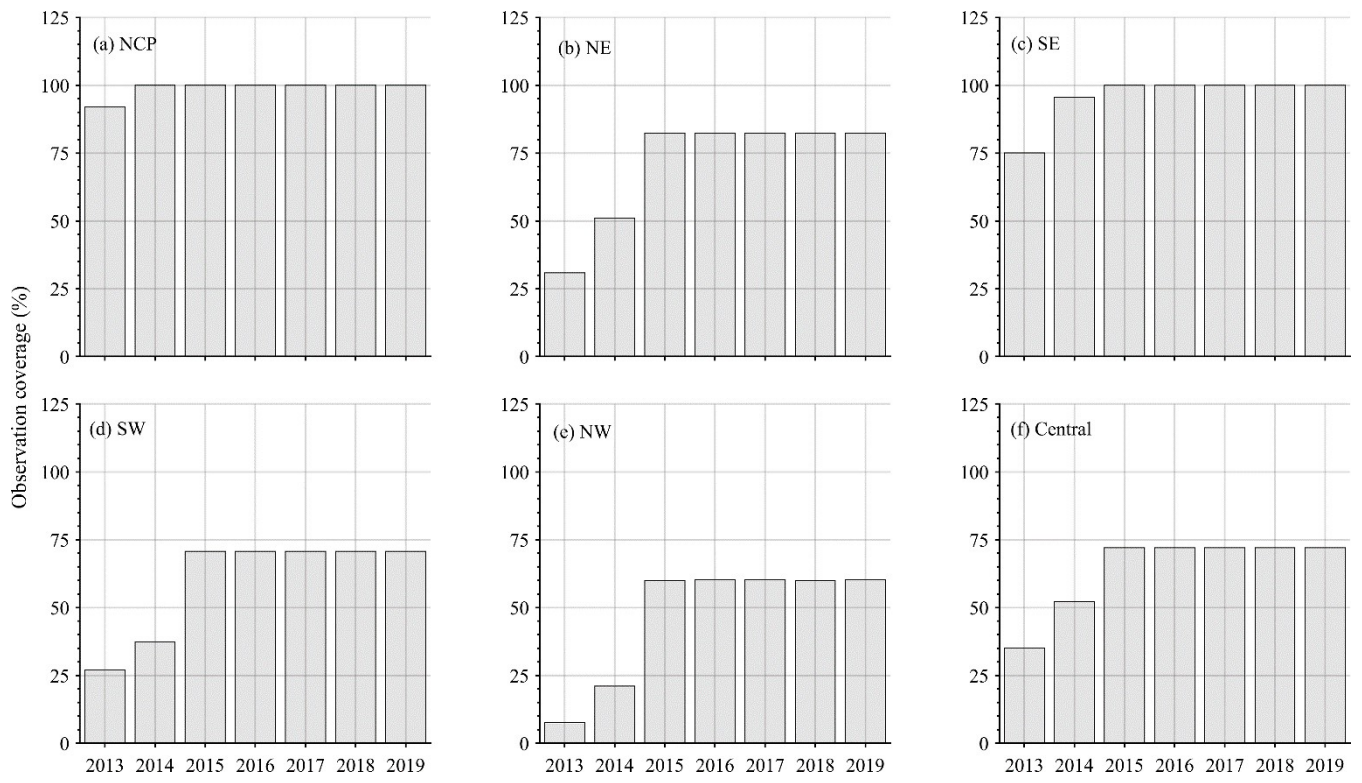
Figure 2: Time series of the observational coverage from 2013 to 2020 over different regions of China.

1204

1205

1206

1207

1208

1209

1210

1211

1212

1213
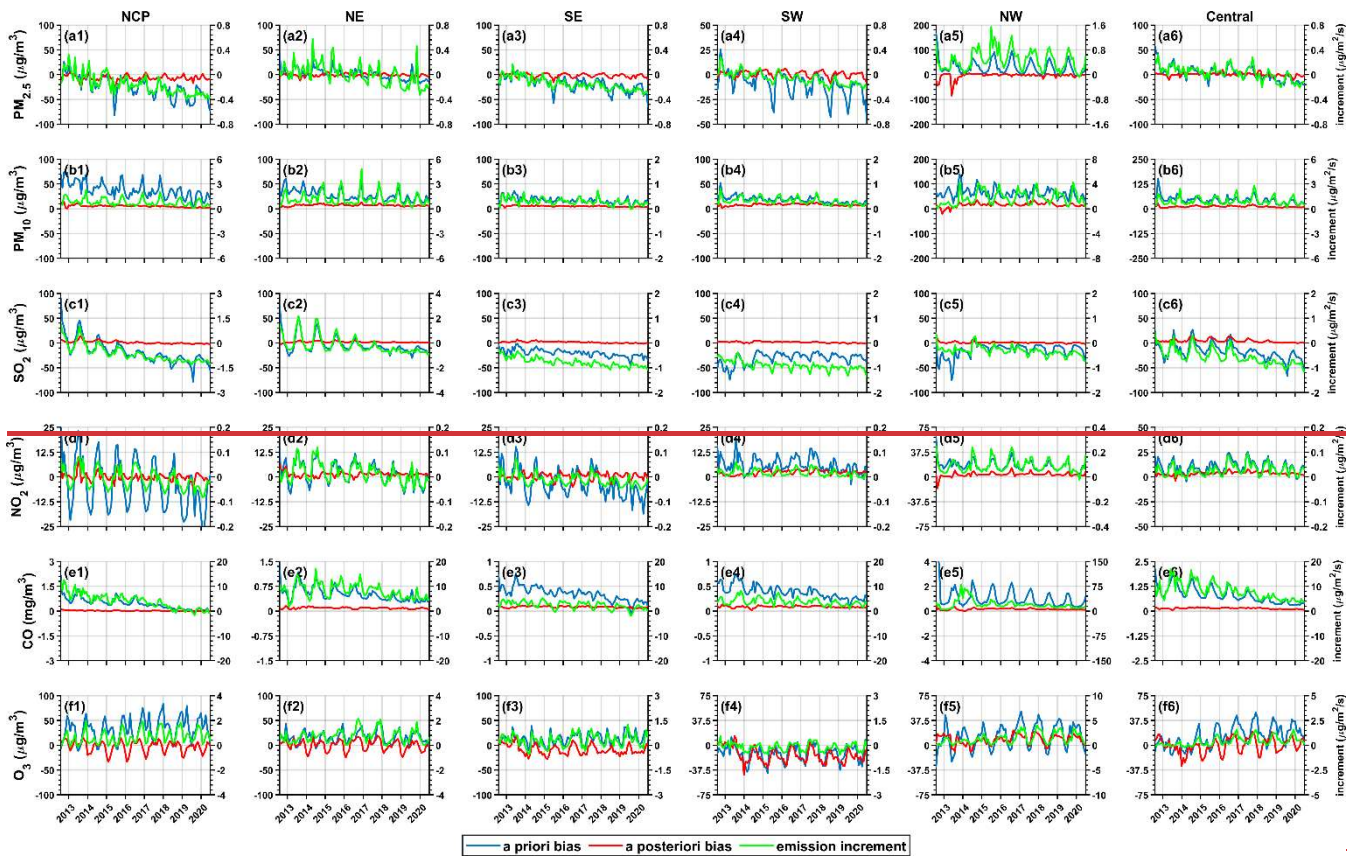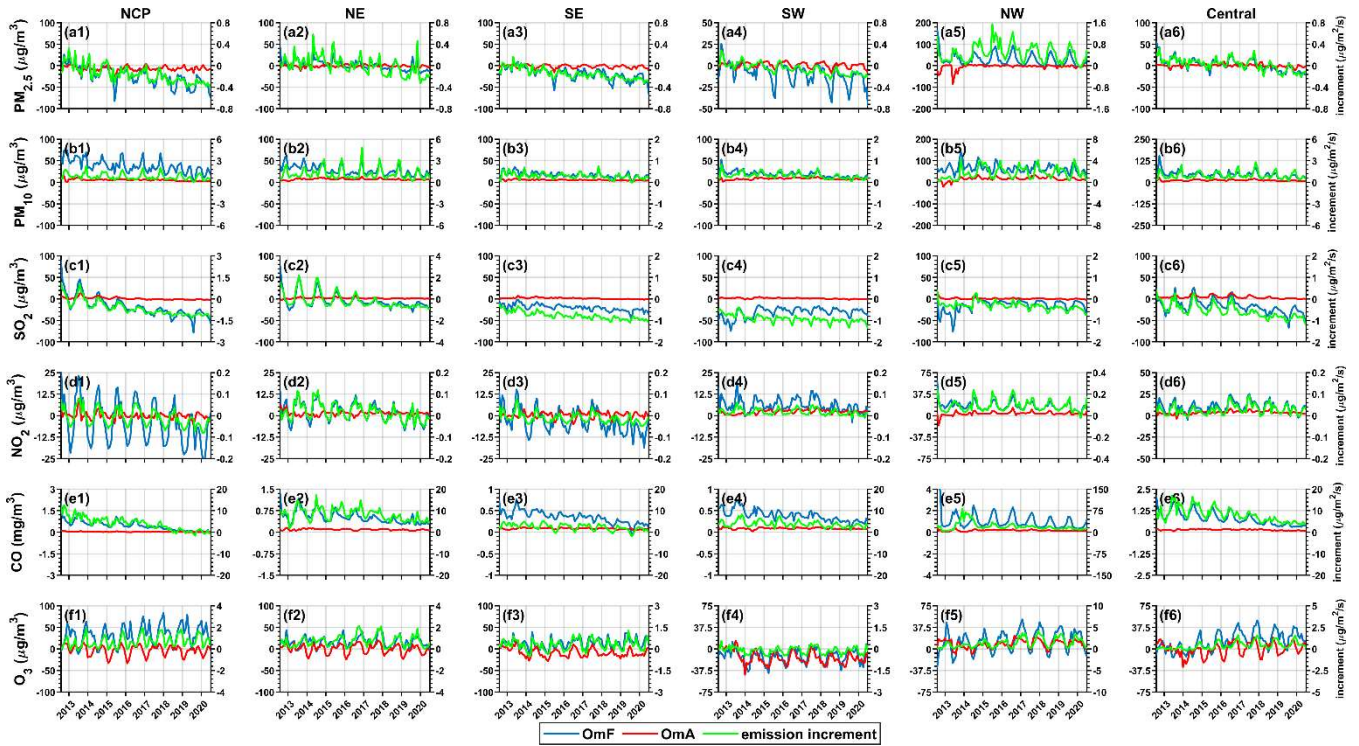
Figure 3: Time series of the *a priori* bias (blue lines), the *a posteriori* bias (red lines), and the emission increment (green lines) from 2013 to 2020 for different species over the six regions of China.

1214
1215

1216

1217
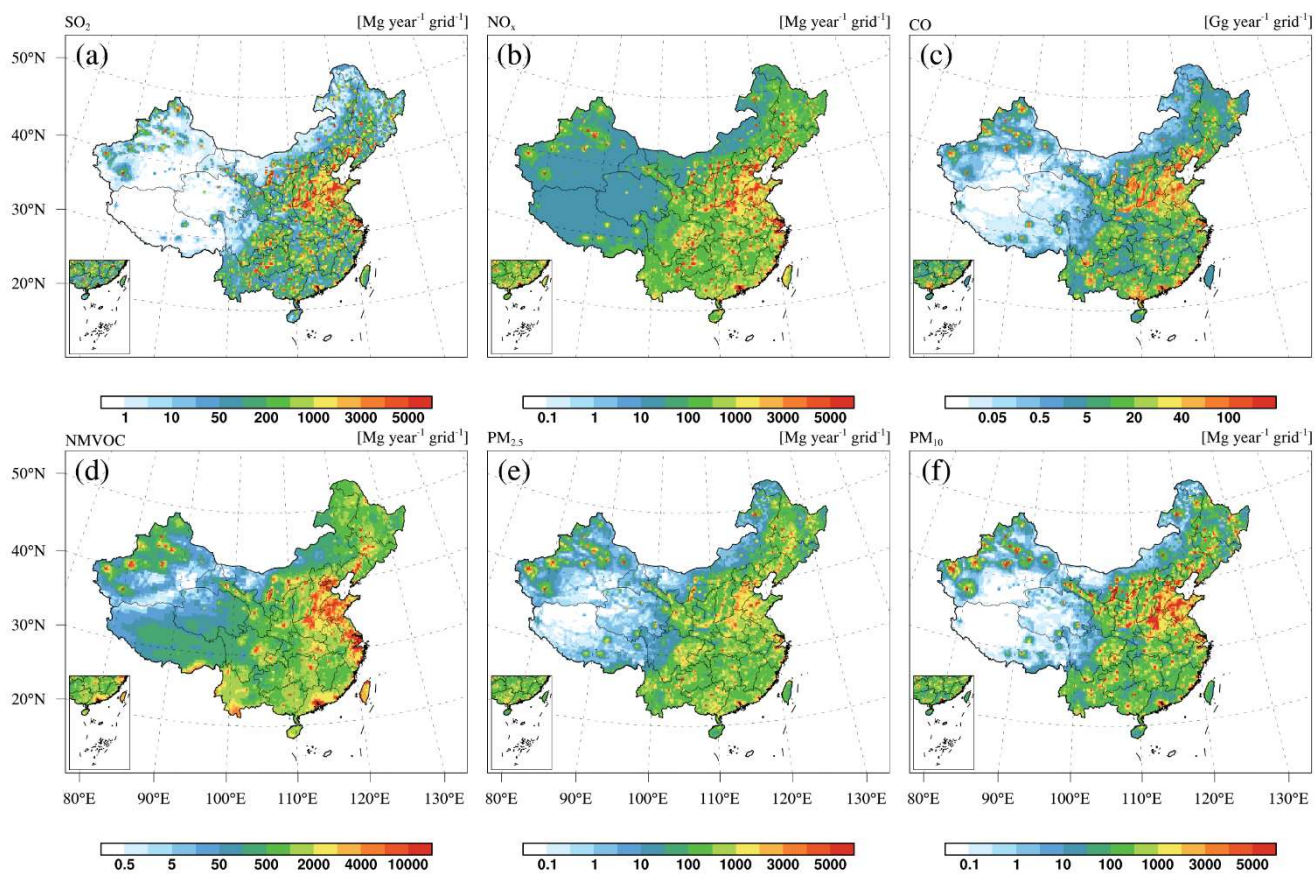
1218

Figure 4: Spatial distributions of the emissions of (a) SO$_2$, (b) NO$_x$, (c) CO, (d) NMVOCs, (e) PM$_{2.5}$, and (f) PM$_{10}$ in 2015 obtained from CAQIEI.

1221

1222

1223
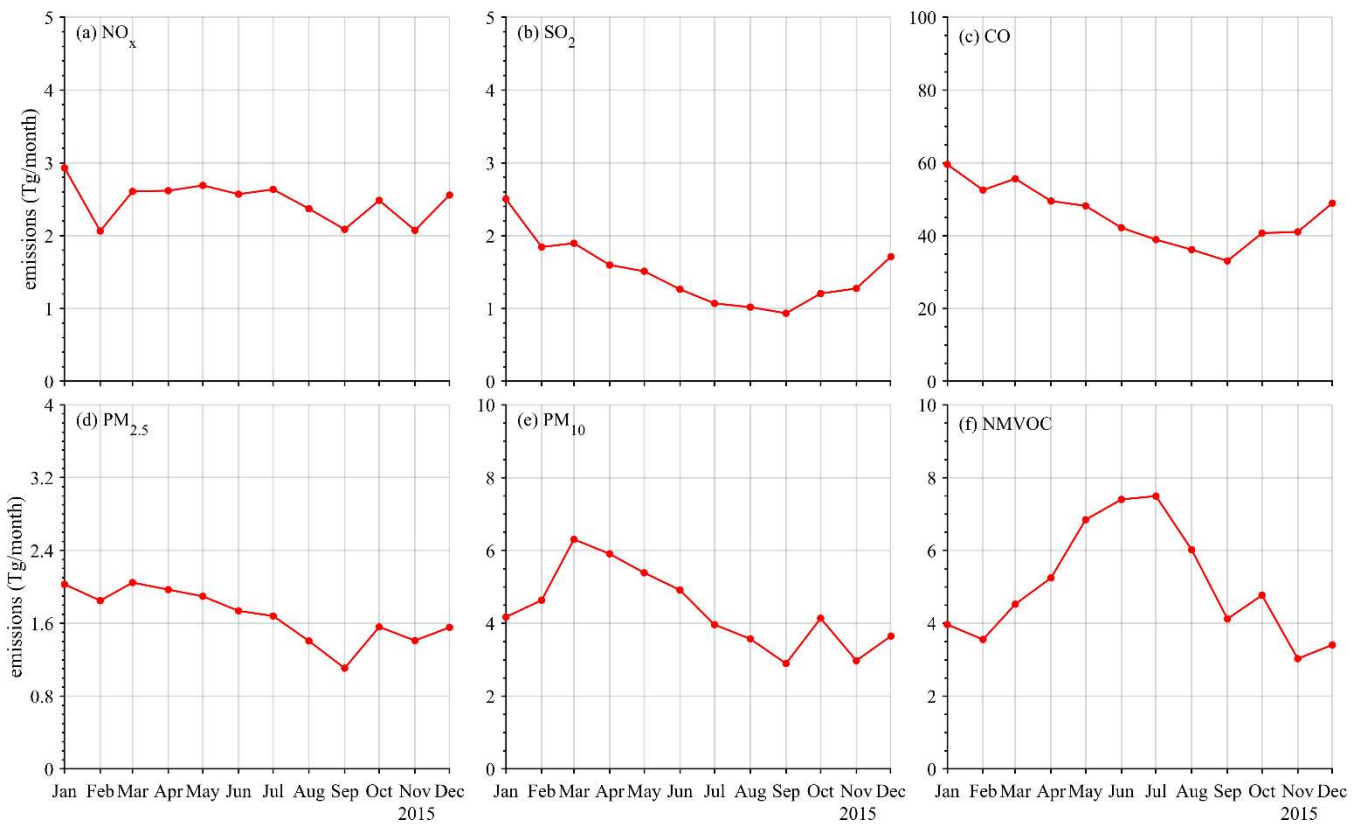
1224

1225 **Figure 5: Monthly series of total emissions of (a) NO$_x$, (b) SO$_2$, (c) CO, (d) PM$_{2.5}$, (e) PM$_{10}$, and (f) NMVOCs in China for year 2015**
1226 **obtained from CAQIEI.**

1227

1228

1229

1230

1231

1232

1233

1234

1235

1236

1237

1238

1239

1240

1241
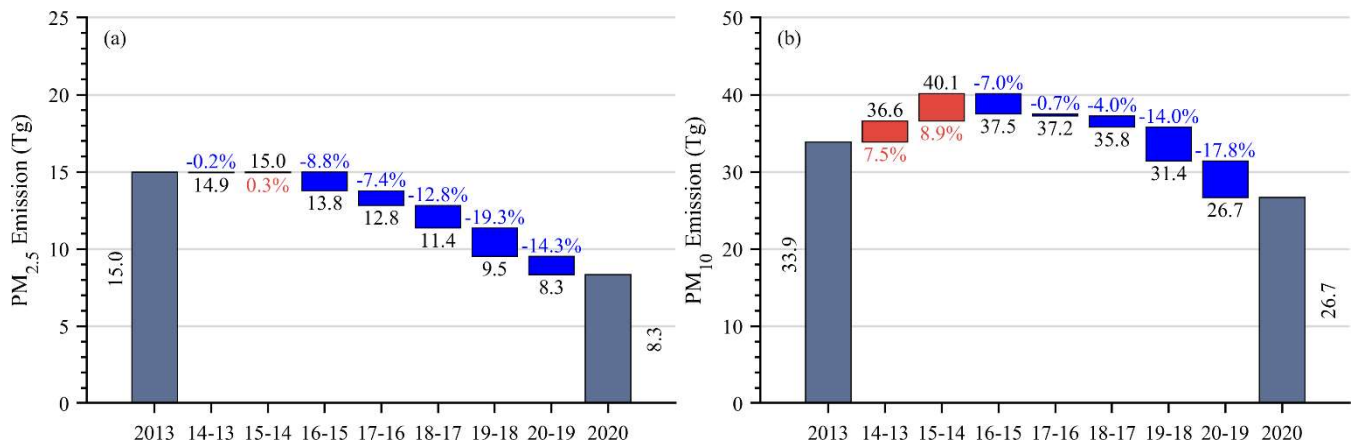
1242

1243 **Figure 6: Emission changes in (a) PM₂.₅ and (b) PM₁₀ obtained from CAQIEI from 2013 to 2020.**
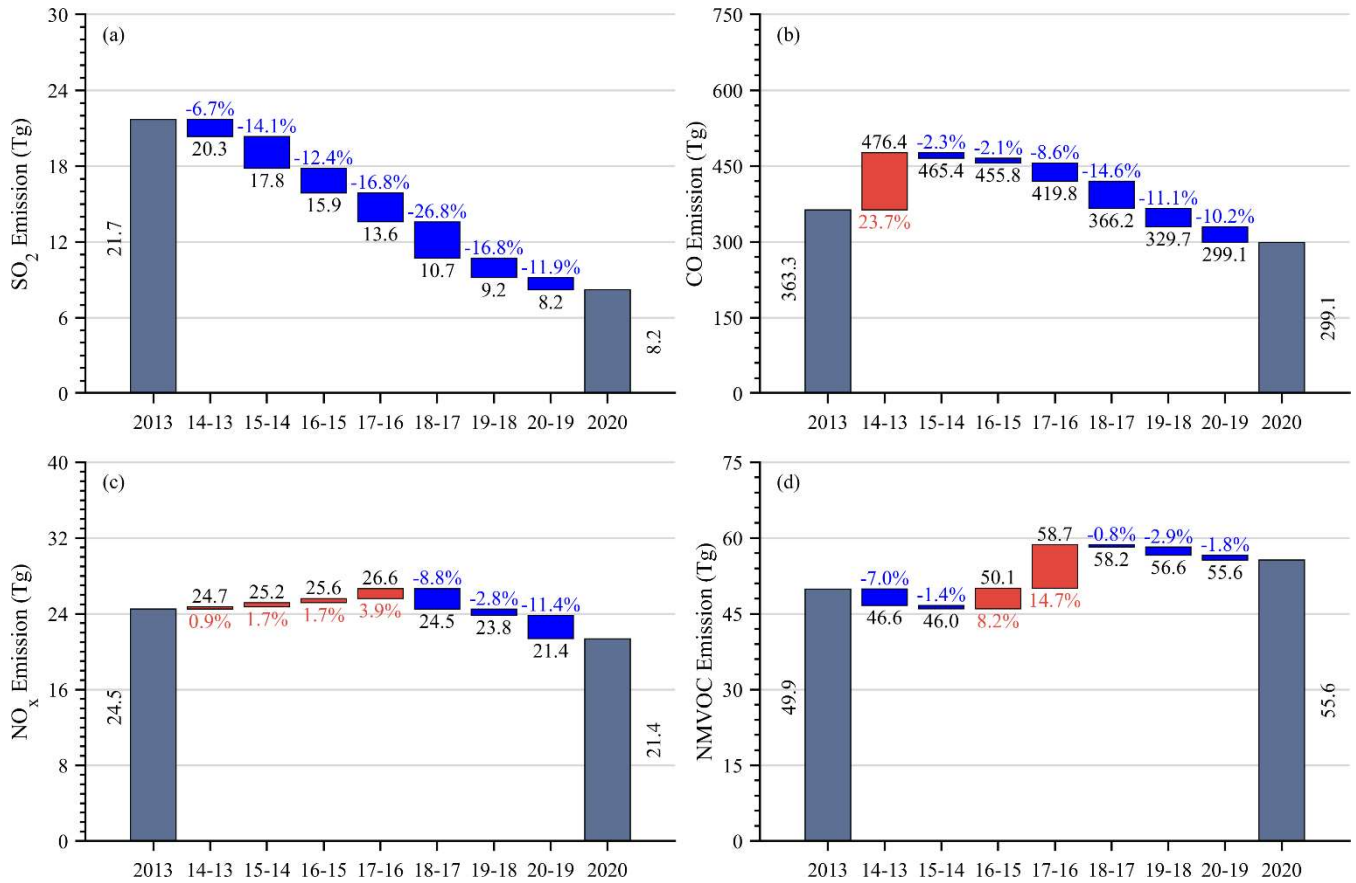
1244

1245 **Figure 7: Emission changes in (a) SO₂, (b) CO, (c) NOₓ, and (d) NMVOCs obtained from CAQIEI from 2013 to 2020.**

1246
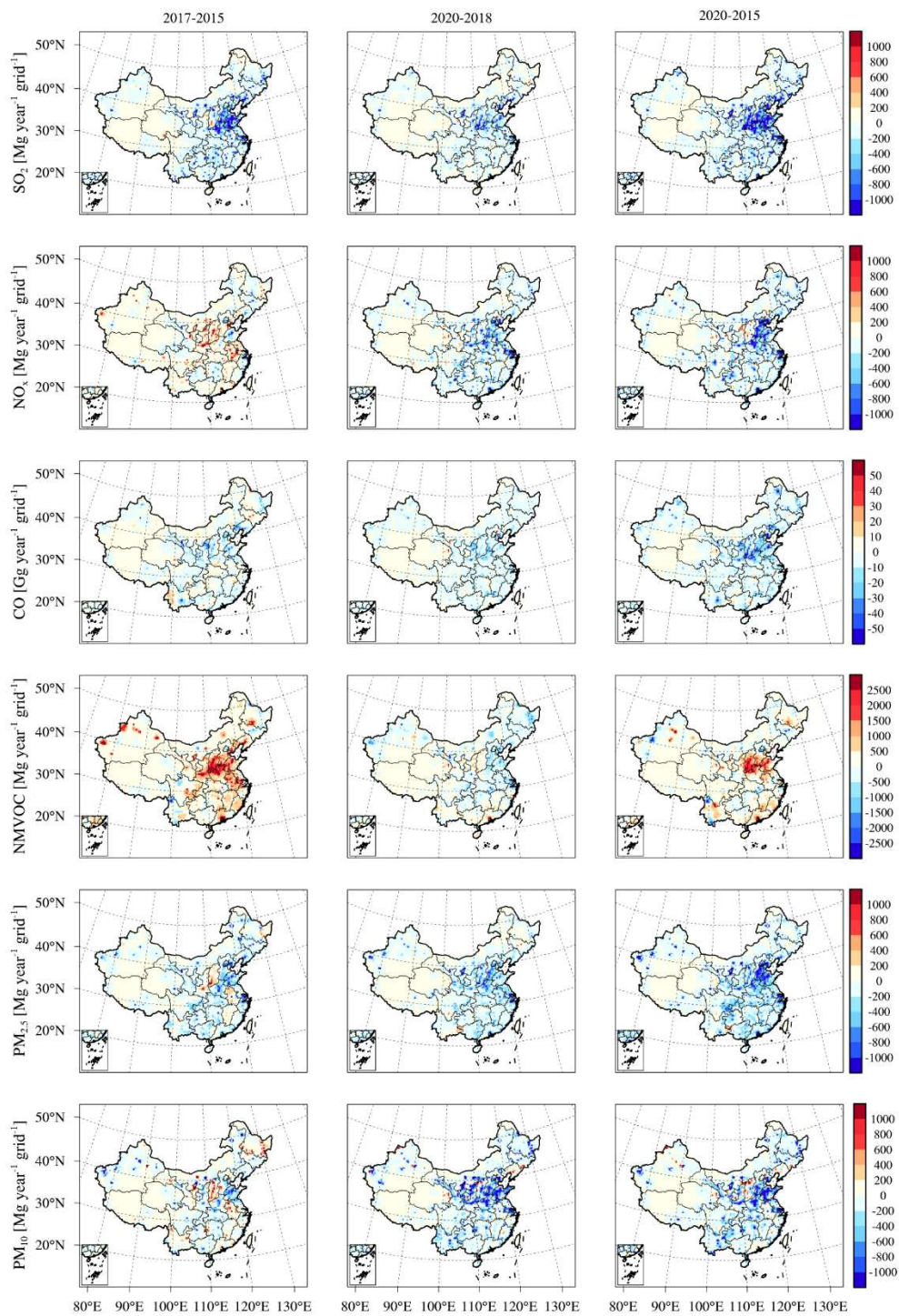
1247

1248 **Figure 8: Spatial distributions of the emission changes of different species during 2015–2017 (left panels), 2018–2020 (middle panels),**
1249 **and 2015–2020 (right panels) obtained from CAQIEI from 2013 to 2020.**
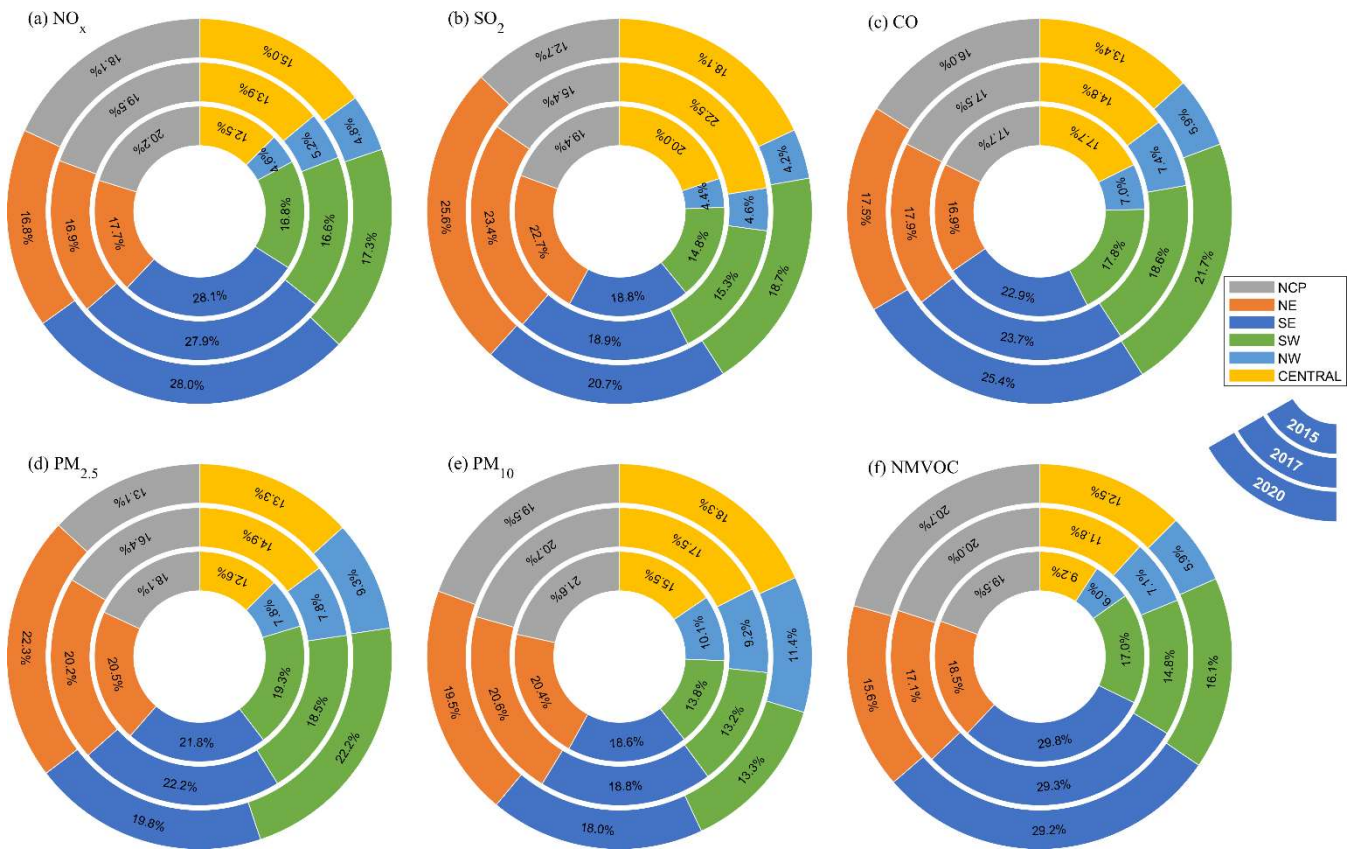
1250

Figure 9: Emission distributions of (a) NOₓ, (b) SO₂, (c) CO, (d) PM2.5, € PM₁₀, and (f) NMVOCs among different regions in China obtained from CAQIEI in 2015, 2017 and 2020.

1253

1254
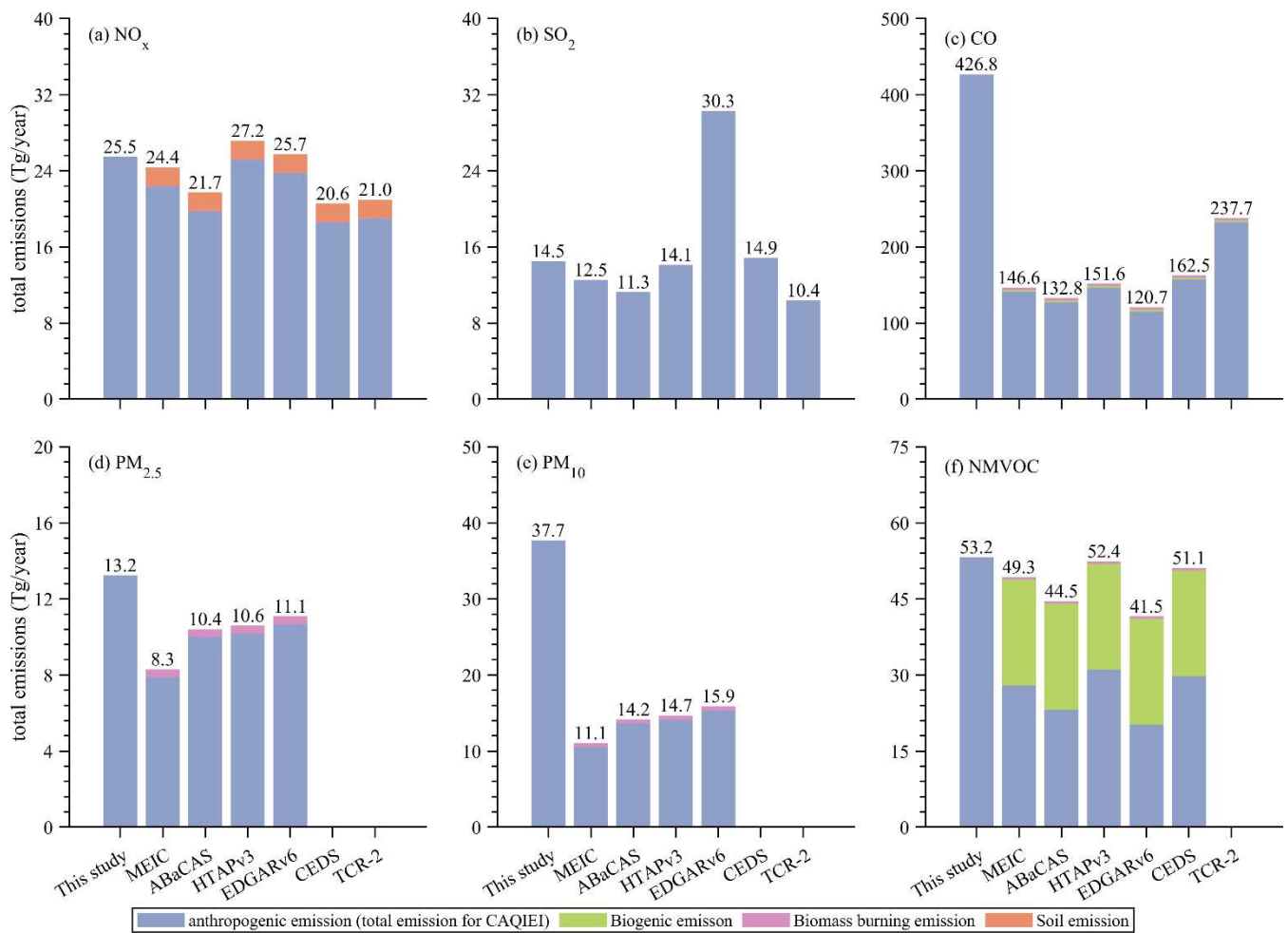
1255

Figure 10: Comparisons of the averaged emissions of (a) NO$_x$, (b) SO$_2$, (c) CO, (d) PM$_{2.5}$, (e) PM$_{10}$, and (f) NMVOCs over China from 2015 to 2018 between CAQIEI and previous inventories added with natural sources.

1256
1257

1258
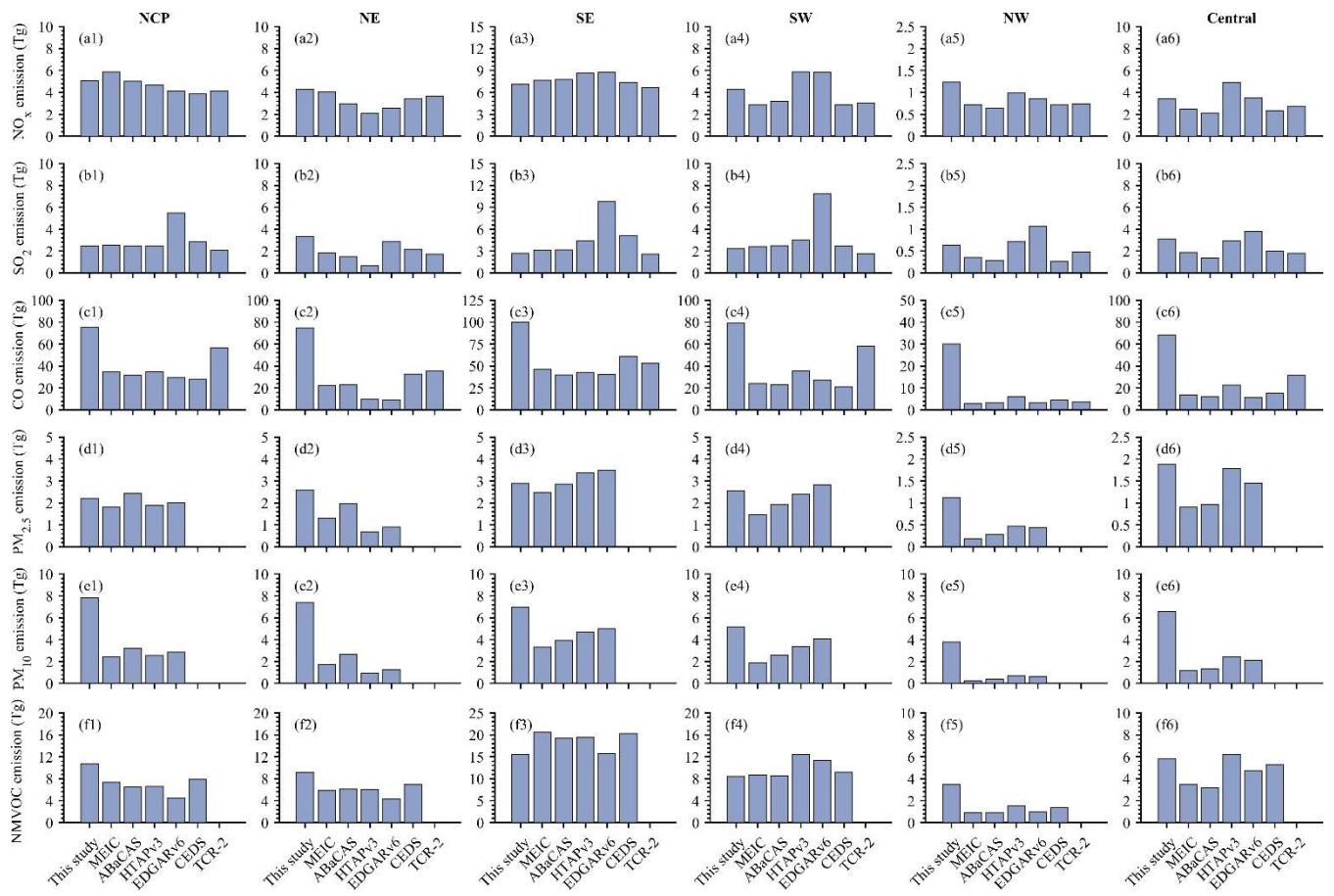
Figure 11: Comparisons of the averaged emissions of (a) NO$_x$, (b) SO$_2$, (c) CO, (d) PM$_{2.5}$, (e) PM$_{10}$, and (f) NMVOCs over different regions in China from 2015 to 2018 between CAQIEI and previous inventories added with natural sources.
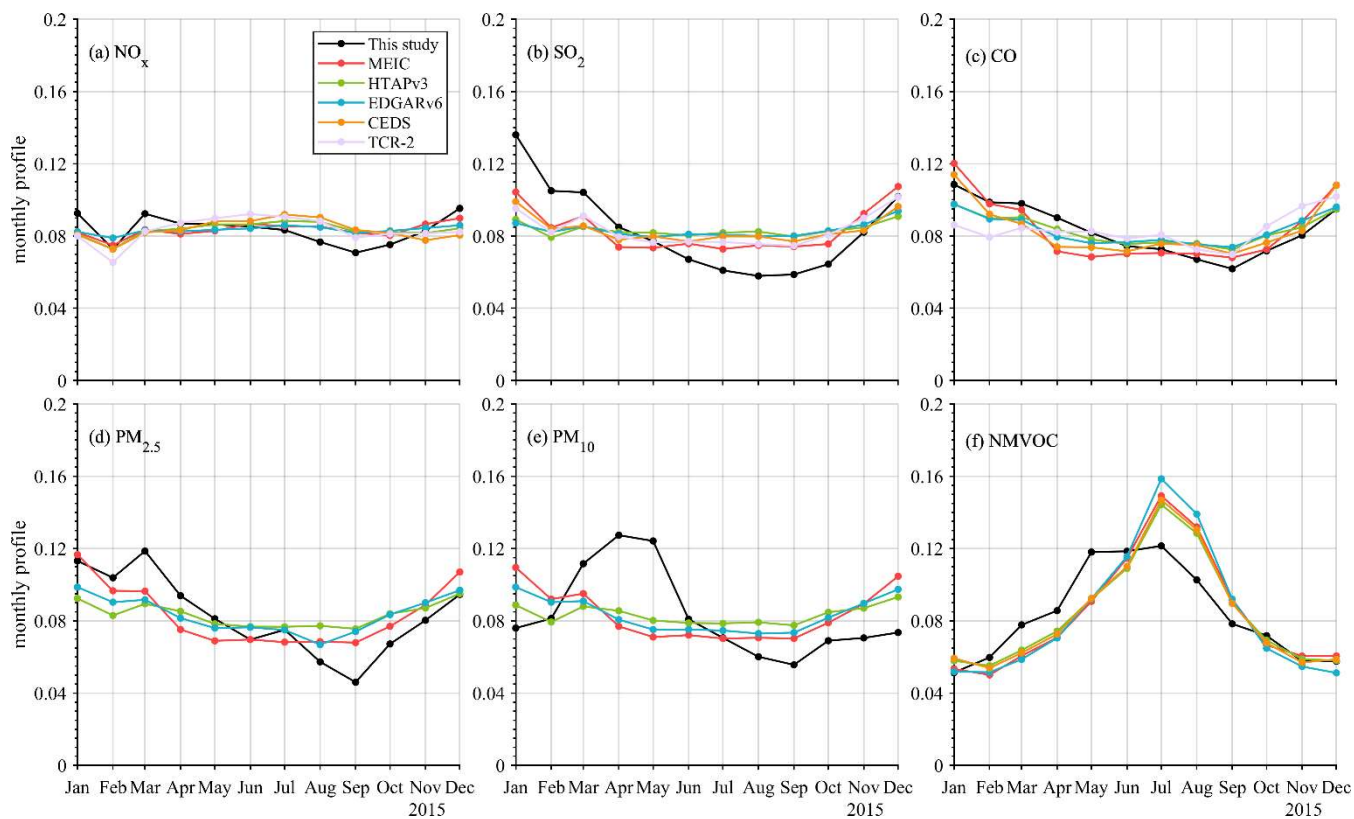
Figure 12: Comparisons of the monthly profiles of (a) NOₓ, (b) SO₂, (c) CO, (d) PM₂.₅, (e) PM₁₀, and (f) NMVOCs over China averaged from 2015 to 2018 between CAQIEI and previous inventories added with natural sources.
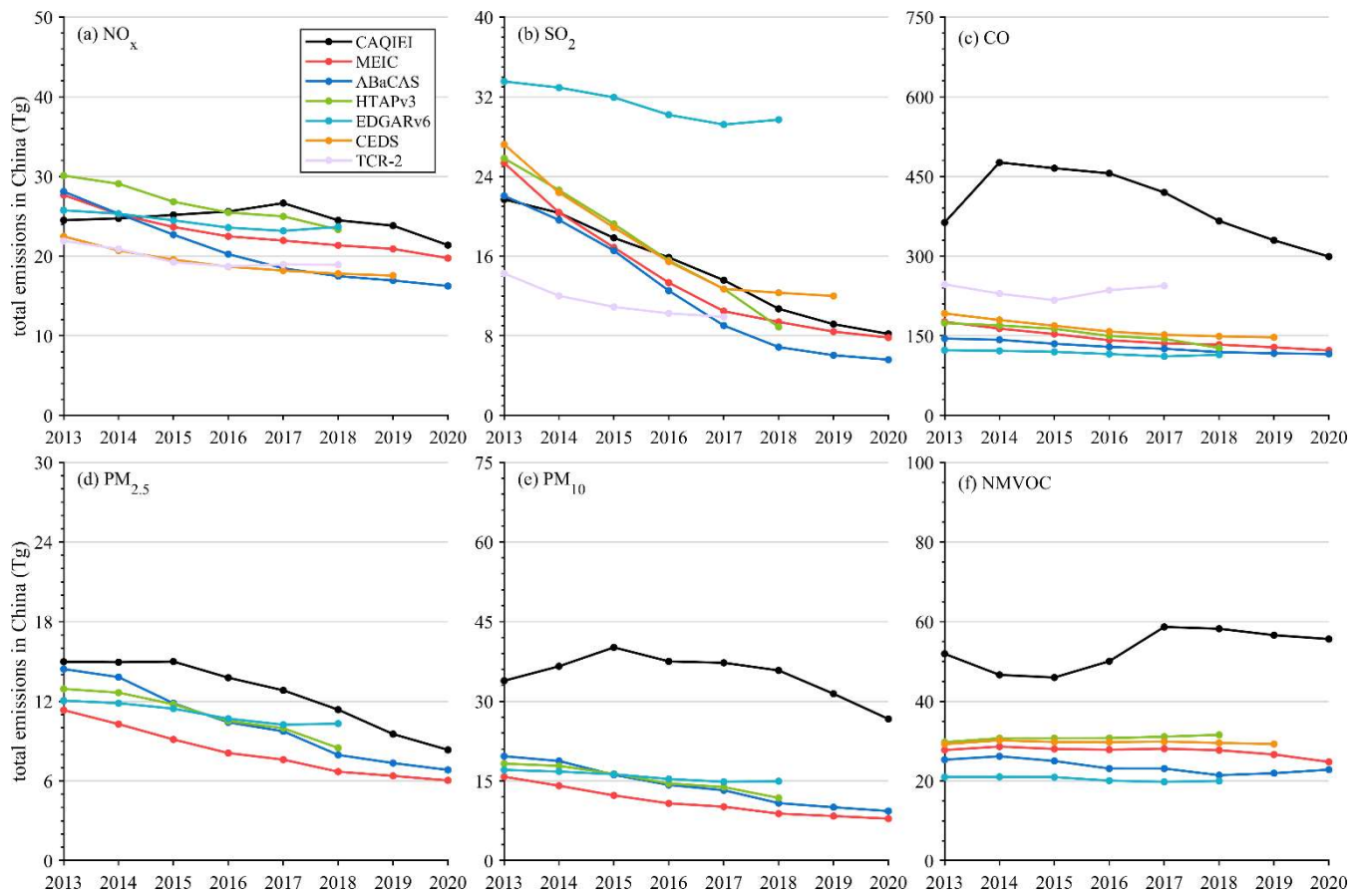
Figure 13: Time series of annual emissions of (a) NO$_x$, (b) SO$_2$, (c) CO, (d) PM$_{2.5}$, (e) PM$_{10}$ and (f) NMVOC over China from 2013 to 2020 obtained from CAQIEI and previous inventories. Note that the natural sources were not included in the previous inventories in this figure.
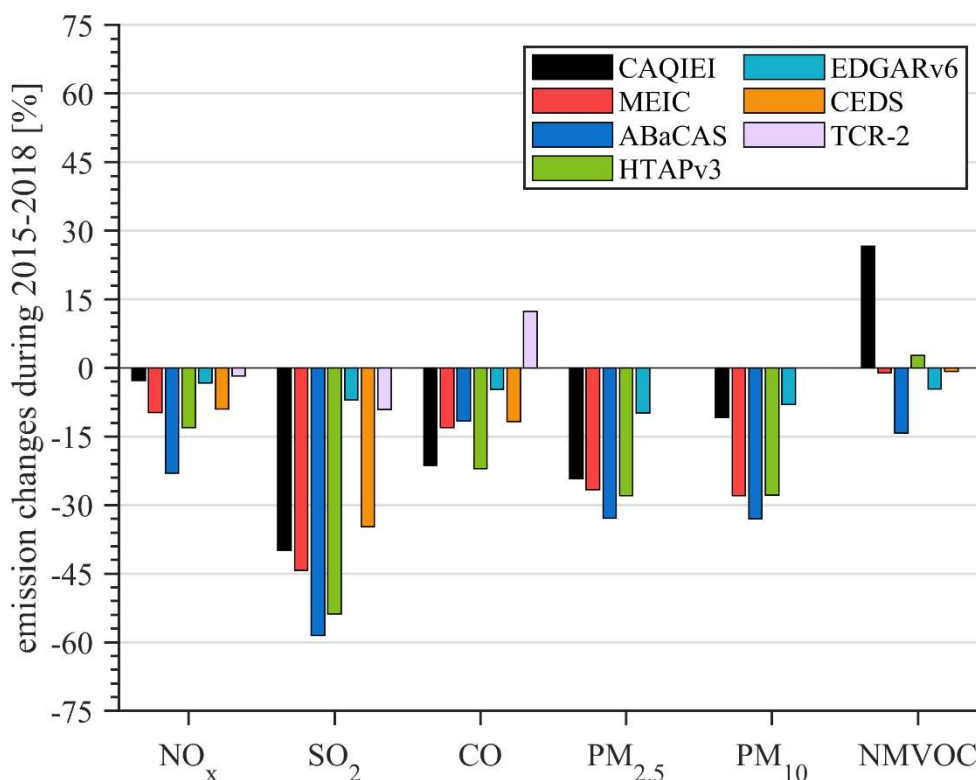
Figure 14: Comparisons of the calculated emission changes of (a) NO_x, (b) SO_2, (c) CO, (d) $PM_{2.5}$, (e) PM_{10}, and (f) NMVOCs over China from 2015 to 2018 between CAQIEI and previous inventories. Note that the natural sources were not included in the calculation of the emission changes in this figure.

Author contributions

X.T., Z.W., and J.Z. conceived and designed the project; L.K., H.W., X.T., and L.W. established the data assimilation system; Q.W. and L.K. performed the meteorology simulations; L.K., H.C., and J.L. conducted the ensemble simulation with the NAQPMS model; J.L., L.Z., W.W., B.L., Q.W., D.C. and Y.P. provided the air quality monitoring data; H.W. performed the quality control of the observation data; and L.K. performed the inversion estimation, generated the figures, and wrote the paper, with comments provided by G.R.C.

Competing interests

The authors declare no competing financial interest.

Acknowledgements

We acknowledge the use of surface air quality observation data from CNEMC and the strong support from the National Key Scientific and Technological Infrastructure project "Earth System Science Numerical Simulator Facility" (EarthLab), which provide us with ample computational resources to fill the requirement of the inversion of multiple years using the ensemble method at a high grid resolution of 15km.

Financial support

This research has been sponsored by the National Natural Science Foundation of China (Grant Nos. 42175132, 92044303, 42205119), the National Key R&D Program (Grant No. 2020YFA0607802), the CAS Information Technology Program (Grant No. CAS-WX2021SF-0107-02).

References

Athanasopoulou, E., Tombrou, M., Pandis, S. N., and Russell, A. G.: The role of sea-salt emissions and heterogeneous chemistry in the air quality of polluted coastal areas, Atmos. Chem. Phys., 8, 5755-5769, https://doi.org/10.5194/acp-8-5755-2008, 2008.

Bergamaschi, P., Hein, R., Heimann, M., and Crutzen, P. J.: Inverse modeling of the global CO cycle 1. Inversion of CO mixing ratios, J. Geophys. Res.-Atmos., 105, 1909-1927, https://doi.org/10.1029/1999jd900818, 2000.

Bobbink, R., Hornung, M., and Roelofs, J. G. M.: The effects of air-borne nitrogen pollutants on species diversity in natural and semi-natural European vegetation, J. Ecol., 86, 717-738, https://doi.org/10.1046/j.1365-2745.1998.8650717.x, 1998.

Brasseur, G. P., Hauglustaine, D. A., Walters, S., Rasch, P. J., Müller, J.-F., Granier, C., and Tie, X. X.: MOZART, a global chemical transport model for ozone and related chemical tracers: 1. Model description, J. Geophys. Res.-Atmos., 103, 28265-28289, https://doi.org/10.1029/98JD02397, 1998.

Cao, H. S., Fu, T. M., Zhang, L., Henze, D. K., Miller, C. C., Lerot, C., Abad, G. G., De Smedt, I., Zhang, Q., van Roozendael, M., Hendrick, F., Chance, K., Li, J., Zheng, J. Y., and Zhao, Y. H.: Adjoint inversion of Chinese non-methane volatile organic compound emissions using space-based observations of formaldehyde and glyoxal, Atmos. Chem. Phys., 18, 15017-15046, https://10.5194/acp-18-15017-2018, 2018.

Cohen, A. J., Brauer, M., Burnett, R., Anderson, H. R., Frostad, J., Estep, K., Balakrishnan, K., Brunekreef, B., Dandona, L., Dandona, R., Feigin, V., Freedman, G., Hubbell, B., Jobling, A., Kan, H., Knibbs, L., Liu, Y., Martin, R., Morawska, L., Pope, C. A., Shin, H., Straif, K., Shaddick, G., Thomas, M., van Dingenen, R., van Donkelaar, A., Vos, T., Murray, C. J. L., and Forouzanfar, M. H.: Estimates and 25-year trends of the global burden of disease attributable to ambient air pollution: an analysis of data from the Global Burden of Diseases Study 2015, Lancet, 389, 1907-1918, https://doi.org/10.1016/s0140-6736(17)30505-6, 2017.

Crippa, M., Guizzardi, D., Butler, T., Keating, T., Wu, R., Kaminski, J., Kuenen, J., Kurokawa, J., Chatani, S., Morikawa, T., Pouliot, G., Racine, J., Moran, M. D., Klimont, Z., Manseau, P. M., Mashayekhi, R., Henderson, B. H., Smith, S. J., Suchyta, H., Muntean, M., Solazzo, E., Banja, M., Schaaf, E., Pagani, F., Woo, J. H., Kim, J., Monforti-Ferrario, F., Pisoni, E., Zhang, J., Niemi, D., Sassi, M., Ansari, T., and Foley, K.: The HTAP_v3 emission mosaic: merging regional and global monthly emissions (2000–2018) to support air quality modelling and policies, Earth Syst. Sci. Data, 15, 2667-2694, https://doi.org/10.5194/essd-15-2667-2023, 2023.

Dee, D. P. and Da Silva, A. M.: Data assimilation in the presence of forecast bias, Q. J. R. Meteorol. Soc., 124, 269-295, https://doi.org/10.1002/qj.49712454512, 1998.

Du, Q., Zhao, C., Zhang, M., Dong, X., Chen, Y., Liu, Z., Hu, Z., Zhang, Q., Li, Y., Yuan, R., and Miao, S.: Modeling diurnal variation of surface $PM_{2.5}$ concentrations over East China with WRF-Chem: impacts from boundary-layer mixing and anthropogenic emission, Atmos. Chem. Phys., 20, 2839-2863, https://doi.org/10.5194/acp-20-2839-2020, 2020.

Elbern, H., Strunk, A., Schmidt, H., and Talagrand, O.: Emission rate and chemical state estimation by 4-dimensional variational inversion, Atmos. Chem. Phys., 7, 3749-3769, https://doi.org/10.5194/acp-7-3749-2007, 2007.

Elguindi, N., Granier, C., Stavrakou, T., Darras, S., Bauwens, M., Cao, H., Chen, C., van der Gon, H., Dubovik, O., Fu, T. M., Henze, D. K., Jiang, Z., Keita, S., Kuenen, J. J. P., Kurokawa, J., Liousse, C., Miyazaki, K., Muller, J. F., Qu, Z., Solmon, F., and Zheng, B.: Intercomparison of Magnitudes and Trends in Anthropogenic Surface Emissions From Bottom-Up Inventories, Top-Down Estimates, and Emission Scenarios, Earth Future, 8, 20, https://doi.org/10.1029/2020ef001520, 2020.

Evensen, G.: Sequential data assimilation with a nonlinear quasi-geostrophic model using Monte Carlo methods to forecast error statistics, J. Geophys. Res.-Oceans, 99, 10143-10162, https://doi.org/10.1029/94JC00572, 1994.

Fan, H., Zhao, C., Yang, Y., and Yang, X.: Spatio-Temporal Variations of the PM2.5/PM10 Ratios and Its Application to Air Pollution Type Classification in China, Front. Environ. Sci., 9, https://doi.org/10.3389/fenvs.2021.692440, 2021.

Feng, S., Jiang, F., Qian, T., Wang, N., Jia, M., Zheng, S., Chen, J., Ying, F., and Ju, W.: Constraint of non-methane volatile organic compound emissions with TROPOMI HCHO observations and its impact on summertime surface ozone simulation over China, EGUsphere, 2024, 1-34, https://10.5194/egusphere-2023-2654, 2024.

Feng, S., Jiang, F., Wu, Z., Wang, H., Ju, W., and Wang, H.: CO Emissions Inferred From Surface CO Observations Over China in December 2013 and 2017, J. Geophys. Res.-Atmos., 125, e2019JD031808, https://doi.org/10.1029/2019JD031808, 2020.

Fu, X., Wang, T., Gao, J., Wang, P., Liu, Y. M., Wang, S. X., Zhao, B., and Xue, L. K.: Persistent Heavy Winter Nitrate Pollution Driven by Increased Photochemical Oxidants in Northern China, Environ. Sci. Technol., 54, 3881-3889, https://doi.org/10.1021/acs.est.9b07248, 2020.

Gaubert, B., Emmons, L. K., Raeder, K., Tilmes, S., Miyazaki, K., Arellano Jr, A. F., Elguindi, N., Granier, C., Tang, W., Barré, J., Worden, H. M., Buchholz, R. R., Edwards, D. P., Franke, P., Anderson, J. L., Saunois, M., Schroeder, J., Woo, J. H., Simpson, I. J., Blake, D. R., Meinardi, S., Wennberg, P. O., Crounse, J., Teng, A., Kim, M., Dickerson, R. R., He, H., Ren, X., Pusede, S. E., and Diskin, G. S.: Correcting model biases of CO in East Asia: impact on oxidant distributions during KORUS-AQ, Atmos. Chem. Phys., 20, 14617-14647, https://doi.org/10.5194/acp-20-14617-2020, 2020.

Goldberg, D. L., Saide, P. E., Lamsal, L. N., de Foy, B., Lu, Z. F., Woo, J. H., Kim, Y., Kim, J., Gao, M., Carmichael, G., and Streets, D. G.: A top-down assessment using OMI NO2 suggests an underestimate in the NOx emissions inventory in Seoul, South Korea, during KORUS-AQ, Atmos. Chem. Phys., 19, 1801-1818, https://10.5194/acp-19-1801-2019, 2019.

Granier, C., Lamarque, J., Mieville, A., Muller, J., Olivier, J., Orlando, J., Peters, J., Petron, G., Tyndall, G., and Wallens, S.: POET, a database of surface emissions of ozone precursors, available at: http://www.aero.jussieu.fr/projet/ACCENT/POET.php (last access: 09 October 2023), 2005.

Hauglustaine, D. A., Brasseur, G. P., Walters, S., Rasch, P. J., Muller, J. F., Emmons, L. K., and Carroll, C. A.: MOZART, a global chemical transport model for ozone and related chemical tracers 2. Model results and evaluation, J. Geophys. Res.-Atmos., 103, 28291-28335, https://doi.org/10.1029/98jd02398, 1998.

Henze, D. K., Seinfeld, J. H., and Shindell, D. T.: Inverse modeling and mapping US air quality influences of inorganic PM2.5 precursor emissions using the adjoint of GEOS-Chem, Atmos. Chem. Phys., 9, 5877-5903, https://doi.org/10.5194/acp-9-5877-2009, 2009.

Hernández, D. L., Vallano, D. M., Zavaleta, E. S., Tzankova, Z., Pasari, J. R., Weiss, S., Selmants, P. C., and Morozumi, C.: Nitrogen Pollution Is Linked to US Listed Species Declines, BioScience, 66, 213-222, https://doi.org/10.1093/biosci/biw003, 2016.

Jalkanen, J. P., Johansson, L., Kukkonen, J., Brink, A., Kalli, J., and Stipa, T.: Extension of an assessment model of ship traffic exhaust emissions for particulate matter and carbon monoxide, Atmos. Chem. Phys., 12, 2641-2659, https://doi.org/10.5194/acp-12-2641-2012, 2012.

Janssens-Maenhout, G., Crippa, M., Guizzardi, D., Dentener, F., Muntean, M., Pouliot, G., Keating, T., Zhang, Q., Kurokawa, J., Wankmuller, R., van der Gon, H. D., Kuenen, J. J. P., Klimont, Z., Frost, G., Darras, S., Koffi, B., and Li, M.: HTAP_v2.2: a mosaic of regional and global emission grid maps for 2008 and 2010 to study hemispheric transport of air pollution, Atmos. Chem. Phys., 15, 11411-11432, https://doi.org/10.5194/acp-15-11411-2015, 2015.

Jiang, Z., Worden, J. R., Worden, H., Deeter, M., Jones, D. B. A., Arellano, A. F., and Henze, D. K.: A 15-year record of CO emissions constrained by MOPITT CO observations, Atmos. Chem. Phys., 17, 4565-4583, https://doi.org/10.5194/acp-17-4565-2017, 2017.

Kaiser, J. W., Heil, A., Andreae, M. O., Benedetti, A., Chubarova, N., Jones, L., Morcrette, J. J., Razinger, M., Schultz, M. G., Suttie, M., and van der Werf, G. R.: Biomass burning emissions estimated with a global fire assimilation system based on observed fire radiative power, Biogeosciences, 9, 527-554, https://doi.org/10.5194/bg-9-527-2012, 2012.

Kan, H., Chen, R., and Tong, S.: Ambient air pollution, climate change, and population health in China, Environ. Int., 42, 10-19, https://doi.org/10.1016/j.envint.2011.03.003, 2012.

Kang, J.-Y., Yoon, S.-C., Shao, Y., and Kim, S.-W.: Comparison of vertical dust flux by implementing three dust emission schemes in WRF/Chem, J. Geophys. Res.-Atmos., 116, https://doi.org/10.1029/2010JD014649, 2011

Kong, L., Tang, X., Wang, Z. F., Zhu, J., Li, J. J., Wu, H. J., Wu, Q. Z., Chen, H. S., Zhu, L. L., Wang, W., Liu, B., Wang, Q., Chen D. H., Pan Y. P., Li, J., Wu, L., and Carmichael, G. R.: Inversed Emission Inventory for Chinese Air Quality (CAQIEI) version 1.0, Science Data Bank [dataset], https://doi.org/10.57760/sciencedb.13151, 2023.

Kong, L., Tang, X., Zhu, J., Wang, Z., Pan, Y., Wu, H., Wu, L., Wu, Q., He, Y., Tian, S., Xie, Y., Liu, Z., Sui, W., Han, L., and Carmichael, G.: Improved Inversion of Monthly Ammonia Emissions in China Based on the Chinese Ammonia Monitoring Network and Ensemble Kalman Filter, Environ. Sci. Technol., 53, 12529-12538, https://doi.org/10.1021/acs.est.9b02701, 2019.

Kong, L., Tang, X., Zhu, J., Wang, Z., Sun, Y., Fu, P., Gao, M., Wu, H., Lu, M., Wu, Q., Huang, S., Sui, W., Li, J., Pan, X., Wu, L., Akimoto, H., and Carmichael, G. R.: Unbalanced emission reductions of different species and sectors in China during COVID-19 lockdown derived by multi-species surface observation assimilation, Atmos. Chem. Phys., 23, 6217-6240, https://doi.org/10.5194/acp-23-6217-2023, 2023.

Kong, L., Tang, X., Zhu, J., Wang, Z., Li, J., Wu, H., Wu, Q., Chen, H., Zhu, L., Wang, W., Liu, B., Wang, Q., Chen, D., Pan, Y., Song, T., Li, F., Zheng, H., Jia, G., Lu, M., Wu, L., and Carmichael, G. R.: A 6-year-long (2013–2018) high-resolution air quality reanalysis dataset in China based on the assimilation of surface observations from CNEMC, Earth Syst. Sci. Data, 13, 529-570, https://doi.org/10.5194/essd-13-529-2021, 2021.

Kong, L., Tang, X., Zhu, J., Wang, Z., Fu, J. S., Wang, X., Itahashi, S., Yamaji, K., Nagashima, T., Lee, H. J., Kim, C. H., Lin, C. Y., Chen, L., Zhang, M., Tao, Z., Li, J., Kajino, M., Liao, H., Wang, Z., Sudo, K., Wang, Y., Pan, Y., Tang, G., Li, M., Wu, Q., Ge, B., and Carmichael, G. R.: Evaluation and uncertainty investigation of the NO2, CO and NH3 modeling over China under the framework of MICS-Asia III, Atmos. Chem. Phys., 20, 181-202, https://doi.org/10.5194/acp-20-181-2020, 2020.

Koohkan, M. R., Bocquet, M., Roustan, Y., Kim, Y., and Seigneur, C.: Estimation of volatile organic compound emissions for Europe using data assimilation, Atmos. Chem. Phys., 13, 5887-5905, https://doi.org/10.5194/acp-13-5887-2013, 2013.

Koukouli, M. E., Theys, N., Ding, J. Y., Zyrichidou, I., Mijling, B., Balis, D., and Johannes, V. R.: Updated SO2 emission estimates over China using OMI/Aura observations, Atmos. Meas. Tech., 11, 1817-1832, 10.5194/amt-11-1817-2018, 2018.

Krotkov, N. A., McLinden, C. A., Li, C., Lamsal, L. N., Celarier, E. A., Marchenko, S. V., Swartz, W. H., Bucsela, E. J., Joiner, J., Duncan, B. N., Boersma, K. F., Veefkind, J. P., Levelt, P. F., Fioletov, V. E., Dickerson, R. R., He, H., Lu, Z. F., and Streets, D. G.: Aura OMI observations of regional SO2 and NO2 pollution changes from 2005 to 2015, Atmos. Chem. Phys., 16, 4605-4629, https://doi.org/10.5194/acp-16-4605-2016, 2016.

Krupa, S. V.: Effects of atmospheric ammonia (NH3) on terrestrial vegetation: a review, Environ. Pollut., 124, 179-221, https://doi.org/10.1016/s0269-7491(02)00434-7, 2003.

Kurokawa, J. and Ohara, T.: Long-term historical trends in air pollutant emissions in Asia: Regional Emission inventory in ASia (REAS) version 3, Atmos. Chem. Phys., 20, 12761-12793, https://doi.org/10.5194/acp-20-12761-2020, 2020.

Kurokawa, J., Ohara, T., Morikawa, T., Hanayama, S., Janssens-Maenhout, G., Fukui, T., Kawashima, K., and Akimoto, H.: Emissions of air pollutants and greenhouse gases over Asian regions during 2000-2008: Regional Emission inventory in ASia (REAS) version 2, Atmos. Chem. Phys., 13, 11019-11058, https://doi.org/10.5194/acp-13-11019-2013, 2013.

Lei, L., Zhou, W., Chen, C., He, Y., Li, Z. J., Sun, J. X., Tang, X., Fu, P. Q., Wang, Z. F., and Sun, Y. L.: Long-term characterization of aerosol chemistry in cold season from 2013 to 2020 in Beijing, China, Environ. Pollut., 268, 9, 10.1016/j.envpol.2020.115952, 2021.

Li, C., McLinden, C., Fioletov, V., Krotkov, N., Carn, S., Joiner, J., Streets, D., He, H., Ren, X., Li, Z., and Dickerson, R. R.: India Is Overtaking China as the World's Largest Emitter of Anthropogenic Sulfur Dioxide, Sci Rep, 7, 14304, https://doi.org/10.1038/s41598-017-14639-8, 2017a.

Li, H., Cheng, J., Zhang, Q., Zheng, B., Zhang, Y., Zheng, G., and He, K.: Rapid transition in winter aerosol composition in Beijing from 2014 to 2017: response to clean air actions, Atmos. Chem. Phys., 19, 11485-11499, https://doi.org/10.5194/acp-19-11485-2019, 2019a.

Li, J., Wang, Z., Zhuang, G., Luo, G., Sun, Y., and Wang, Q.: Mixing of Asian mineral dust with anthropogenic pollutants over East Asia: a model case study of a super-duststorm in March 2010, Atmos. Chem. Phys., 12, 7591-7607, 2012.

Li, K., Jacob, D. J., Liao, H., Shen, L., Zhang, Q., and Bates, K. H.: Anthropogenic drivers of 2013-2017 trends in summer surface ozone in China, Proc. Natl. Acad. Sci. U.S.A., 116, 422-427, https://doi.org/10.1073/pnas.1812168116, 2019b.

Li, L. Y., Yang, W. Z., Xie, S. D., and Wu, Y.: Estimations and uncertainty of biogenic volatile organic compound emission inventory in China for 2008-2018, Sci. Total Environ., 733, 10, https://doi.org/10.1016/j.scitotenv.2020.139301, 2020a.

Li, M., Zhang, Q., Zheng, B., Tong, D., Lei, Y., Liu, F., Hong, C. P., Kang, S. C., Yan, L., Zhang, Y. X., Bo, Y., Su, H., Cheng, Y. F., and He, K. B.: Persistent growth of anthropogenic non-methane volatile organic compound (NMVOC) emissions in China during 1990-2017: drivers, speciation and ozone formation potential, Atmos. Chem. Phys., 19, 8897-8913, https://doi.org/10.5194/acp-19-8897-2019, 2019c.

Li, M., Zhang, Q., Kurokawa, J. I., Woo, J. H., He, K., Lu, Z., Ohara, T., Song, Y., Streets, D. G., Carmichael, G. R., Cheng, Y., Hong, C., Huo, H., Jiang, X., Kang, S., Liu, F., Su, H., and Zheng, B.: MIX: a mosaic Asian anthropogenic emission inventory under the international collaboration framework of the MICS-Asia and HTAP, Atmos. Chem. Phys., 17, 935-963, https://doi.org/10.5194/acp-17-935-2017, 2017b.

Li, N., Long, X., Tie, X. X., Cao, J. J., Huang, R. J., Zhang, R., Feng, T., Liu, S. X., and Li, G. H.: Urban dust in the Guanzhong basin of China, part II: A case study of urban dust pollution using the WRF-Dust model, Sci. Total Environ., 541, 1614-1624, https://doi.org/10.1016/j.scitotenv.2015.10.028, 2016.

Li, R., Cui, L. L., Li, J. L., Zhao, A., Fu, H. B., Wu, Y., Zhang, L. W., Kong, L. D., and Chen, J. M.: Spatial and temporal variation of particulate matter and gaseous pollutants in China during 2014-2016, Atmos. Environ., 161, 235-246, https://doi.org/10.1016/j.atmosenv.2017.05.008, 2017c.

Li, S., Wang, S., Wu, Q., Zhang, Y., Ouyang, D., Zheng, H., Han, L., Qiu, X., Wen, Y., Liu, M., Jiang, Y., Yin, D., Liu, K., Zhao, B., Zhang, S., Wu, Y., and Hao, J.: Emission trends of air pollutants and CO2 in China from 2005 to 2021, Earth Syst. Sci. Data, 15, 2279-2294, https://doi.org/10.5194/essd-15-2279-2023, 2023.

Li, W., Shao, L., Wang, W., Li, H., Wang, X., Li, Y., Li, W., Jones, T., and Zhang, D.: Air quality improvement in response to intensified control strategies in Beijing during 2013-2019, Sci. Total Environ., 744, https://doi.org/10.1016/j.scitotenv.2020.140776, 2020b.

Liu, J., Tong, D., Zheng, Y. X., Cheng, J., Qin, X. Y., Shi, Q. R., Yan, L., Lei, Y., and Zhang, Q.: Carbon and air pollutant emissions from China's cement industry 1990-2015: trends, evolution of technologies, and drivers, Atmos. Chem. Phys., 21, 1627-1647, https://doi.org/10.5194/acp-21-1627-2021, 2021.

Liu, J., Mauzerall, D. L., Chen, Q., Zhang, Q., Song, Y., Peng, W., Klimont, Z., Qiu, X. H., Zhang, S. Q., Hu, M., Lin, W. L., Smith, K. R., and Zhu, T.: Air pollutant emissions from Chinese households: A major and underappreciated ambient pollution source, Proc. Natl. Acad. Sci. U.S.A., 113, 7756-7761, https://doi.org/10.1073/pnas.1604537113, 2016.

Lu, X., Zhang, L., Wang, X. L., Gao, M., Li, K., Zhang, Y. Z., Yue, X., and Zhang, Y. H.: Rapid Increases in Warm-Season Surface Ozone and Resulting Health Impact in China Since 2013, Environ. Sci. Technol. Lett., 7, 240-247, https://doi.org/10.1021/acs.estlett.0c00171, 2020.

Lu, X., Hong, J. Y., Zhang, L., Cooper, O. R., Schultz, M. G., Xu, X. B., Wang, T., Gao, M., Zhao, Y. H., and Zhang, Y. H.: Severe Surface Ozone Pollution in China: A Global Perspective, Environ. Sci. Technol. Lett., 5, 487-494, https://doi.org/10.1021/acs.estlett.8b00366, 2018.

Ma, C. Q., Wang, T. J., Mizzi, A. P., Anderson, J. L., Zhuang, B. L., Xie, M., and Wu, R. S.: Multiconstituent Data Assimilation With WRF-Chem/DART: Potential for Adjusting Anthropogenic Emissions and Improving Air Quality Forecasts Over Eastern China, J. Geophys. Res.-Atmos., 124, 7393-7412, https://doi.org/10.1029/2019jd030421, 2019.

Martin, S. T., Hung, H. M., Park, R. J., Jacob, D. J., Spurr, R. J. D., Chance, K. V., and Chin, M.: Effects of the physical state of tropospheric ammonium-sulfate-nitrate particles on global aerosol direct radiative forcing, Atmos. Chem. Phys., 4, 183-214, https://doi.org/10.5194/acp-4-183-2004, 2004.

McDuffie, E. E., Smith, S. J., O'Rourke, P., Tibrewal, K., Venkataraman, C., Marais, E. A., Zheng, B., Crippa, M., Brauer, M., and Martin, R. V.: A global anthropogenic emission inventory of atmospheric pollutants from sector- and fuel-specific sources (1970-2017): an application of the Community Emissions Data System (CEDS), Earth Syst. Sci. Data, 12, 3413-3442, https://doi.org/10.5194/essd-12-3413-2020, 2020.

Miyazaki, K. and Eskes, H.: Constraints on surface NOx emissions by assimilating satellite observations of multiple species, Geophys. Res. Lett., 40, 4745-4750, https://doi.org/10.1002/grl.50894, 2013.

Miyazaki, K., Bowman, K. W., Yumimoto, K., Walker, T., and Sudo, K.: Evaluation of a multi-model, multi-constituent assimilation framework for tropospheric chemical reanalysis, Atmos. Chem. Phys., 20, 931-967, https://doi.org/10.5194/acp-20-931-2020, 2020a.

Miyazaki, K., Eskes, H. J., Sudo, K., Takigawa, M., van Weele, M., and Boersma, K. F.: Simultaneous assimilation of satellite NO2, O-3, CO, and HNO3 data for the analysis of tropospheric chemical composition and emissions, Atmos. Chem. Phys., 12, 9545-9579, https://doi.org/10.5194/acp-12-9545-2012, 2012.

Miyazaki, K., Bowman, K., Sekiya, T., Eskes, H., Boersma, F., Worden, H., Livesey, N., Payne, V. H., Sudo, K., Kanaya, Y., Takigawa, M., and Ogochi, K.: Updated tropospheric chemistry reanalysis and emission estimates, TCR-2, for 2005–2018, Earth Syst. Sci. Data, 12, 2223-2259, https://doi.org/10.5194/essd-12-2223-2020, 2020b.

Müller, J.-F., Stavrakou, T., Bauwens, M., George, M., Hurtmans, D., Coheur, P.-F., Clerbaux, C., and Sweeney, C.: Top-Down CO Emissions Based On IASI Observations and Hemispheric Constraints on OH Levels, Geophys. Res. Lett., 45, 1621-1629, https://doi.org/10.1002/2017GL076697, 2018.

Muller, J. F., Stavrakou, T., Bauwens, M., George, M., Hurtmans, D., Coheur, P. F., Clerbaux, C., and Sweeney, C.: Top-Down CO Emissions Based On IASI Observations and Hemispheric Constraints on OH Levels, Geophys. Res. Lett., 45, 1621-1629, https://doi.org/10.1002/2017gl076697, 2018.

Paulot, F., Jacob, D. J., Pinder, R. W., Bash, J. O., Travis, K., and Henze, D. K.: Ammonia emissions in the United States, European Union, and China derived by high-resolution inversion of ammonium wet deposition data: Interpretation with a new agricultural emissions inventory (MASAGE_NH3), J. Geophys. Res.-Atmos., 119, 4343-4364, https://doi.org/10.1002/2013jd021130, 2014.

Peng, Z., Lei, L., Tan, Z. M., Zhang, M., Ding, A., and Kou, X.: Dynamics-based estimates of decline trend with fine temporal variations in China's PM2.5 emissions, EGUsphere, 2023, 1-34, https://doi.org/10.5194/egusphere-2023-755, 2023.

Peng, Z., Lei, L. L., Liu, Z. Q., Su, J. N., Ding, A. J., Ban, J. M., Chen, D., Kou, X. X., and Chu, K. K.: The impact of multi-species surface chemical observation assimilation on air quality forecasts in China, Atmos. Chem. Phys., 18, 18, https://doi.org/10.5194/acp-18-17387-2018, 2018.

Petron, G., Granier, C., Khattatov, B., Lamarque, J. F., Yudin, V., Muller, J. F., and Gille, J.: Inverse modeling of carbon monoxide surface emissions using Climate Monitoring and Diagnostics Laboratory network observations, J. Geophys. Res.-Atmos., 107, 23, https://doi.org/10.1029/2001jd001305, 2002.

Petron, G., Granier, C., Khattatov, B., Yudin, V., Lamarque, J. F., Emmons, L., Gille, J., and Edwards, D. P.: Monthly CO surface sources inventory based on the 2000-2001 MOPITT satellite data, Geophys. Res. Lett., 31, 5, https://doi.org/10.1029/2004gl020560, 2004.

Philip, S., Martin, R. V., Snider, G., Weagle, C. L., van Donkelaar, A., Brauer, M., Henze, D. K., Klimont, Z., Venkataraman, C., Guttikunda, S. K., and Zhang, Q.: Anthropogenic fugitive, combustion and industrial dust is a significant, underrepresented fine particulate matter source in global atmospheric models, Environ. Res. Lett., 12, 7, https://doi.org/10.1088/1748-9326/aa65a4, 2017.

Price, C., Penner, J., and Prather, M.: NOx from lightning .1. Global distribution based on lightning physics, J. Geophys. Res.-Atmos., 102, 5929-5941, https://doi.org/10.1029/96jd03504, 1997.

Prospero, J. M., Ginoux, P., Torres, O., Nicholson, S. E., and Gill, T. E.: Environmental characterization of global sources of atmospheric soil dust identified with the Nimbus 7 Total Ozone Mapping Spectrometer (TOMS) absorbing aerosol product, Rev. Geophys., 40, 31, https://doi.org/10.1029/2000rg000095, 2002.

Qu, Z., Henze, D. K., Capps, S. L., Wang, Y., Xu, X. G., Wang, J., and Keller, M.: Monthly top-down NO_x emissions for China (2005-2012): A hybrid inversion method and trend analysis, J. Geophys. Res.-Atmos., 122, 4600-4625, https://doi.org/10.1002/2016jd025852, 2017.

Qu, Z., Henze, D. K., Li, C., Theys, N., Wang, Y., Wang, J., Wang, W., Han, J., Shim, C., Dickerson, R. R., and Ren, X. R.: SO2 Emission Estimates Using OMI SO2 Retrievals for 2005-2017, J. Geophys. Res.-Atmos., 124, 8336-8359, https://doi.org/10.1029/2019jd030243, 2019.

Randerson, J. T., Van Der Werf, G. R., Giglio, L., Collatz, G. J., and Kasibhatla, P. S.: Global Fire Emissions Database, Version 4.1 (GFEDv4), ORNL DAAC, Oak Ridge, Tennessee, USA, https://doi.org/10.3334/ORNLDAAC/1293, 2017.

Ren, J., Guo, F., and Xie, S.: Diagnosing ozone–NOx–VOC sensitivity and revealing causes of ozone increases in China based on 2013–2021 satellite retrievals, Atmos. Chem. Phys., 22, 15035-15047, https://10.5194/acp-22-15035-2022, 2022.

Sakov, P. and Oke, P. R.: A deterministic formulation of the ensemble Kalman filter: an alternative to ensemble square root filters, Tellus Ser. A-Dyn. Meteorol. Oceanol., 60, 361-371, https://doi.org/10.1111/j.1600-0870.2007.00299.x, 2008.

Sindelarova, K., Granier, C., Bouarar, I., Guenther, A., Tilmes, S., Stavrakou, T., Muller, J. F., Kuhn, U., Stefani, P., and Knorr, W.: Global data set of biogenic VOC emissions calculated by the MEGAN model over the last 30 years, Atmos. Chem. Phys., 14, 9317-9341, https://doi.org/10.5194/acp-14-9317-2014, 2014.

Song, C., Wu, L., Xie, Y., He, J., Chen, X., Wang, T., Lin, Y., Jin, T., Wang, A., Liu, Y., Dai, Q., Liu, B., Wang, Y.-n., and Mao, H.: Air pollution in China: Status and spatiotemporal variations, Environ. Pollut., 227, 334-347, https://doi.org/10.1016/j.envpol.2017.04.075, 2017.

Souri, A. H., Nowlan, C. R., Abad, G. G., Zhu, L., Blake, D. R., Fried, A., Weinheimer, A. J., Wisthaler, A., Woo, J. H., Zhang, Q., Miller, C. E. C., Liu, X., and Chance, K.: An inversion of NOx and non-methane volatile organic compound (NMVOC) emissions using satellite observations during the KORUS-AQ campaign and implications for surface ozone over East Asia, Atmos. Chem. Phys., 20, 9837-9854, https://10.5194/acp-20-9837-2020, 2020.

Stavrakou, T., Muller, J. F., Bauwens, M., De Smedt, I., Van Roozendael, M., De Maziere, M., Vigouroux, C., Hendrick, F., George, M., Clerbaux, C., Coheur, P. F., and Guenther, A.: How consistent are top-down hydrocarbon emissions based on formaldehyde observations from GOME-2 and OMI?, Atmos. Chem. Phys., 15, 11861-11884, https://10.5194/acp-15-11861-2015, 2015.

Stein, O., Schultz, M. G., Bouarar, I., Clark, H., Huijnen, V., Gaudel, A., George, M., and Clerbaux, C.: On the wintertime low bias of Northern Hemisphere carbon monoxide found in global model simulations, Atmos. Chem. Phys., 14, 9295-9316, https://doi.org/10.5194/acp-14-9295-2014, 2014.

Streets, D. G., Bond, T. C., Carmichael, G. R., Fernandes, S. D., Fu, Q., He, D., Klimont, Z., Nelson, S. M., Tsai, N. Y., Wang, M. Q., Woo, J. H., and Yarber, K. F.: An inventory of gaseous and primary aerosol emissions in Asia in the year 2000, J. Geophys. Res.-Atmos., 108, n/a-n/a, https://doi.org/10.1029/2002JD003093, 2003.

Tandeo, P., Ailliot, P., Bocquet, M., Carrassi, A., Miyoshi, T., Pulido, M., and Zhen, Y. C.: A Review of Innovation-Based Methods to Jointly Estimate Model and Observation Error Covariance Matrices in Ensemble Data Assimilation, Mon. Weather Rev., 148, 3973-3994, https://doi.org/10.1175/mwr-d-19-0240.1, 2020.

Tang, M., Liu, Y., He, J., Wang, Z., Wu, Z., and Ji, D.: In situ continuous hourly observations of wintertime nitrate, sulfate and ammonium in a megacity in the North China plain from 2014 to 2019: Temporal variation, chemical formation and regional transport, Chemosphere, 262, https://doi.org/10.1016/j.chemosphere.2020.127745, 2021.

Tang, X., Zhu, J., Wang, Z., Gbaguidi, A., Lin, C., Xin, J., Song, T., and Hu, B.: Limitations of ozone data assimilation with adjustment of NOx emissions: mixed effects on NO_2 forecasts over Beijing and surrounding areas, Atmos. Chem. Phys., 16, 6395-6405, https://doi.org/10.5194/acp-16-6395-2016, 2016.

Tang, X., Zhu, J., Wang, Z., Wang, M., Gbaguidi, A., Li, J., Shao, M., Tang, G. Q., and Ji, D. S.: Inversion of CO emissions over Beijing and its surrounding areas with ensemble Kalman filter, Atmos. Environ., 81, 676-686, https://doi.org/10.1016/j.atmosenv.2013.08.051, 2013.

Tegen, I., Lacis, A. A., and Fung, I.: The influence on climate forcing of mineral aerosols from disturbed soils, Nature, 380, 419-422, https://doi.org/10.1038/380419a0, 1996.

van der Werf, G. R., Randerson, J. T., Giglio, L., Collatz, G. J., Mu, M., Kasibhatla, P. S., Morton, D. C., DeFries, R. S., Jin, Y., and van Leeuwen, T. T.: Global fire emissions and the contribution of deforestation, savanna, forest, agricultural, and peat fires (1997–2009), Atmos. Chem. Phys., 10, 11707-11735, https://doi.org/10.5194/acp-10-11707-2010, 2010.

von Schneidemesser, E., Monks, P. S., Allan, J. D., Bruhwiler, L., Forster, P., Fowler, D., Lauer, A., Morgan, W. T., Paasonen, P., Righi, M., Sindelarova, K., and Sutton, M. A.: Chemistry and the Linkages between Air Quality and Climate Change, Chem. Rev., 115, 3856-3897, https://doi.org/10.1021/acs.chemrev.5b00089, 2015.

Wang, S., Su, H., Chen, C., Tao, W., Streets, D. G., Lu, Z., Zheng, B., Carmichael, G. R., Lelieveld, J., Poeschl, U., and Cheng, Y.: Natural gas shortages during the "coal-to-gas" transition in China have caused a large redistribution of air pollution in winter 2017, Proc. Natl. Acad. Sci. U.S.A., 117, 31018-31025, https://doi.org/10.1073/pnas.2007513117, 2020a.

Wang, S. S., Yu, Y., Zhang, X. X., Lu, H. Y., Zhang, X. Y., and Xu, Z. W.: Weakened dust activity over China and Mongolia from 2001 to 2020 associated with climate change and land-use management, Environ. Res. Lett., 16, 12, https://doi.org/10.1088/1748-9326/ac3b79, 2021.

Wang, X., Liang, X.-Z., Jiang, W., Tao, Z., Wang, J. X. L., Liu, H., Han, Z., Liu, S., Zhang, Y., Grell, G. A., and Peckham, S. E.: WRF-Chem simulation of East Asian air quality: Sensitivity to temporal and vertical emissions distributions, Atmos. Environ., 44, 660-669, https://doi.org/10.1016/j.atmosenv.2009.11.011, 2010.

Wang, X. G. and Bishop, C. H.: A comparison of breeding and ensemble transform Kalman filter ensemble forecast schemes, J. Atmos. Sci., 60, 1140-1158, https://doi.org/10.1175/1520-0469(2003)060<1140:Acobae>2.0.Co;2, 2003.

Wang, X. Y., Lei, Y., Yan, L., Liu, T., Zhang, Q., and He, K. B.: A unit-based emission inventory of SO2, NOx and PM for the Chinese iron and steel industry from 2010 to 2015, Sci. Total Environ., 676, 18-30, https://doi.org/10.1016/j.scitotenv.2019.04.241, 2019a.

Wang, Y. C., Li, X., Wang, Q. Y., Zhou, B. H., Liu, S. X., Tian, J., Hao, Q., Li, G. H., Han, Y. M., Ho, S. S. H., and Cao, J. J.: Response of aerosol composition to the clean air actions in Baoji city of Fen-Wei River Basin, Environ. Res., 210, 10, https://doi.org/10.1016/j.envres.2022.112936, 2022.

Wang, Y. H., Gao, W. K., Wang, S., Song, T., Gong, Z. Y., Ji, D. S., Wang, L. L., Liu, Z. R., Tang, G. Q., Huo, Y. F., Tian, S. L., Li, J. Y., Li, M. G., Yang, Y., Chu, B. W., Petaja, T., Kerminen, V. M., He, H., Hao, J. M., Kulmala, M., Wang, Y. S., and Zhang, Y. H.: Contrasting trends of PM2.5 and surface-ozone concentrations in China from 2013 to 2017, Natl. Sci. Rev., 7, 1331-1339, https://doi.org/10.1093/nsr/nwaa032, 2020b.

Wang, Y. S., Li, W. J., Gao, W. K., Liu, Z. R., Tian, S. L., Shen, R. R., Ji, D. S., Wang, S., Wang, L. L., Tang, G. Q., Song, T., Cheng, M. T., Wang, G. H., Gong, Z. Y., Hao, J. M., and Zhang, Y. H.: Trends in particulate matter and its chemical compositions in China from 2013-2017, Sci. China-Earth Sci., 62, 1857-1871, https://doi.org/10.1007/s11430-018-9373-1, 2019b.

Wu, C. L., Lin, Z. H., Shao, Y. P., Liu, X. H., and Li, Y.: Drivers of recent decline in dust activity over East Asia, Nat. Commun., 13, 10, https://doi.org/10.1038/s41467-022-34823-3, 2022.

World Health Organization (WHO): Ambient air pollution: a global assessment of exposure and burden of disease, https://www.who.int/publications/i/item/9789241511353, last access: 16 November 2023.

Wu, H., Tang, X., Wang, Z., Wu, L., Li, J., Wang, W., Yang, W., and Zhu, J.: High-spatiotemporal-resolution inverse estimation of CO and NOx emission reductions during emission control periods with a modified ensemble Kalman filter, Atmos. Environ., 236, 117631, https://doi.org/10.1016/j.atmosenv.2020.117631, 2020a.

Wu, H. J., Tang, X., Wang, Z. F., Wu, L., Lu, M. M., Wei, L. F., and Zhu, J.: Probabilistic Automatic Outlier Detection for Surface Air Quality Measurements from the China National Environmental Monitoring Network, Adv. Atmos. Sci., 35, 1522-1532, https://doi.org/10.1007/s00376-018-8067-9, 2018.

Wu, J., Kong, S. F., Wu, F. Q., Cheng, Y., Zheng, S. R., Qin, S., Liu, X., Yan, Q., Zheng, H., Zheng, M. M., Yan, Y. Y., Liu, D. T., Ding, S., Zhao, D. L., Shen, G. F., Zhao, T. L., and Qi, S. H.: The moving of high emission for biomass burning in China: View from multi-year emission estimation and human-driven forces, Environ. Int., 142, 17, https://doi.org/10.1016/j.envint.2020.105812, 2020b.

Xing, J., Li, S. W., Jiang, Y. Q., Wang, S. X., Ding, D., Dong, Z. X., Zhu, Y., and Hao, J. M.: Quantifying the emission changes and associated air quality impacts during the COVID-19 pandemic on the North China Plain: a response modeling study, Atmos. Chem. Phys., 20, 14347-14359, https://10.5194/acp-20-14347-2020, 2020.

Xu, Q., Wang, S., Jiang, J., Bhattarai, N., Li, X., Chang, X., Qiu, X., Zheng, M., Hua, Y., and Hao, J.: Nitrate dominates the chemical composition of PM2.5 during haze event in Beijing, China, Sci. Total Environ., 689, 1293-1303, https://doi.org/10.1016/j.scitotenv.2019.06.294, 2019a.

Xu, W., Sun, Y., Wang, Q., Zhao, J., Wang, J., Ge, X., Xie, C., Zhou, W., Du, W., Li, J., Fu, P., Wang, Z., Worsnop, D. R., and Coe, H.: Changes in Aerosol Chemistry From 2014 to 2016 in Winter in Beijing: Insights From High-Resolution Aerosol Mass Spectrometry, J. Geophys. Res.-Atmos., 124, 1132-1147, https://doi.org/10.1029/2018JD029245, 2019b.

Xu, Y., Huang, Z., Ye, J., and Zheng, J.: Hourly emissions of air pollutants and greenhouse gases from open biomass burning in China during 2016–2020, Sci. Data, 10, 629, https://doi.org/10.1038/s41597-023-02541-0, 2023.

Yan, X. Y., Akimoto, H., and Ohara, T.: Estimation of nitrous oxide, nitric oxide and ammonia emissions from croplands in East, Southeast and South Asia, Glob. Change Biol., 9, 1080-1096, https://doi.org/10.1046/j.1365-2486.2003.00649.x, 2003.

Yin, L., Du, P., Zhang, M., Liu, M., Xu, T., and Song, Y.: Estimation of emissions from biomass burning in China (2003–2017) based on MODIS fire radiative energy data, Biogeosciences, 16, 1629-1640, https://doi.org/10.5194/bg-16-1629-2019, 2019.

Zeng, Y., Wang, M., Zhao, C., Chen, S., Liu, Z., Huang, X., and Gao, Y.: WRF-Chem v3.9 simulations of the East Asian dust storm in May 2017: modeling sensitivities to dust emission and dry deposition schemes, Geosci. Model Dev., 13, 2125-2147, https://doi.org/10.5194/gmd-13-2125-2020, 2020.

Zhang, Z. Y., Guan, H., Luo, L., Zheng, N. J., and Xiao, H. Y.: Response of fine aerosol nitrate chemistry to Clean Air Action in winter Beijing: Insights from the oxygen isotope signatures, Sci. Total Environ., 746, 8, https://doi.org/10.1016/j.scitotenv.2020.141210, 2020.

Zheng, B., Chevallier, F., Yin, Y., Ciais, P., Fortems-Cheiney, A., Deeter, M. N., Parker, R. J., Wang, Y. L., Worden, H. M., and Zhao, Y. H.: Global atmospheric carbon monoxide budget 2000-2017 inferred from multi-species atmospheric inversions, Earth Syst. Sci. Data, 11, 1411-1436, https://doi.org/10.5194/essd-11-1411-2019, 2019.

Zheng, B., Tong, D., Li, M., Liu, F., Hong, C. P., Geng, G. N., Li, H. Y., Li, X., Peng, L. Q., Qi, J., Yan, L., Zhang, Y. X., Zhao, H. Y., Zheng, Y. X., He, K. B., and Zhang, Q.: Trends in China's anthropogenic emissions since 2010 as the consequence of clean air actions, Atmos. Chem. Phys., 18, 14095-14111, https://doi.org/10.5194/acp-18-14095-2018, 2018.

Zheng, Y. X., Xue, T., Zhang, Q., Geng, G. N., Tong, D., Li, X., and He, K. B.: Air quality improvements and health benefits from China's clean air action since 2013, Environ. Res. Lett., 12, 9, https://doi.org/10.1088/1748-9326/aa8a32, 2017.

Zhong, Q., Tao, S., Ma, J., Liu, J., Shen, H., Shen, G., Guan, D., Yun, X., Meng, W., Yu, X., Cheng, H., Zhu, D., Wan, Y., and Hu, J.: PM2.5 reductions in Chinese cities from 2013 to 2019 remain significant despite the inflating effects of meteorological conditions, One Earth, 4, 448-458, https://doi.org/10.1016/j.oneear.2021.02.003, 2021.

Zhou, M., Nie, W., Qiao, L., Huang, D. D., Zhu, S., Lou, S., Wang, H., Wang, Q., Tao, S., Sun, P., Liu, Y., Xu, Z., An, J., Yan, R., Su, H., Huang, C., Ding, A., and Chen, C.: Elevated Formation of Particulate Nitrate From N2O5 Hydrolysis in the Yangtze River Delta Region From 2011 to 2019, Geophys. Res. Lett., 49, e2021GL097393, https://doi.org/10.1029/2021GL097393, 2022a.

Zhou, W., Lei, L., Du, A. D., Zhang, Z. Q., Li, Y., Yang, Y., Tang, G. Q., Chen, C., Xu, W. Q., Sun, J. X., Li, Z. J., Fu, P. Q., Wang, Z. F., and Sun, Y. L.: Unexpected Increases of Severe Haze Pollution During the Post COVID-19 Period: Effects of Emissions, Meteorology, and Secondary Production, J. Geophys. Res.-Atmos., 127, 14, https://doi.org/10.1029/2021jd035710, 2022b.

1639   Zhou, W., Gao, M., He, Y., Wang, Q. Q., Xie, C. H., Xu, W. Q., Zhao, J., Du, W., Qiu, Y. M., Lei, L., Fu, P. Q., Wang, Z. F., Worsnop, D.

1640   R., Zhang, Q., and Sun, Y. L.: Response of aerosol chemistry to clean air action in Beijing, China: Insights from two-year ACSM

1641   measurements and model simulations, Environ. Pollut., 255, 11, https://doi.org/10.1016/j.envpol.2019.113345, 2019.

1642

Supplementary Material

Text S1: Evaluation of the meteorological simulation

The performance of meteorological simulation is important for the inversion estimation since the meteorological parameters influence the transport, chemical and removal process of air pollutants and affect the estimation of flow-dependent background error covariance. Figure S18–S23 presents the comparisons of the simulated meteorological parameters, including zonal wind (U), meridional wind (V), temperature (T), relative humidity (RH) and precipitation, against the observations obtained from China Meteorological Administration (Figure S24). Evaluation statistics of meteorological simulation are also presented in Table S1. It shows that the WRF simulation can generally captured the main features of the different meteorological parameters over the different regions of China. The calculated correlation coefficient is 0.49–1.00 for different parameters, and the values of MB (RMSE) are -0.36–0.01 (0.3–0.52) m/s for U, -0.37–0.32 (0.32–0.80) m/s for V, -1.11–1.11 (0.6–2.17) ℃ for T, -11.2 to -2.59 (6.94–12.06) % for RH, and -2.05–37.35 (5.45–61.62) mm for precipitation. This suggests WRF simulation generally well reproduce the meteorological conditions for all regions of China, which is acceptable for the inversion estimates.

Text S2: Assessment of the influences of site differences on the emission inversions

The emission increments at the observation sites (a posteriori minus a priori) for different species in China from 2013 to 2015 under the scenarios of fixed observation sites (blue lines) and varying observation sites (orange) were calculated to assess the influences of the site differences on the emission inversions (Fig. S2). In the fixed-site scenario, it is assumed that the number of observation sites remains constant at the 2013 level while in the varying-site scenario, the number of observation sites increases over time. The differences in emission increments between these two scenarios are used to analyze the impact of changes in the observation coverage on the emission inversions. Please note that, to simplify calculations, we only computed the emission increments at the locations of observation sites. Therefore, they may not be equal to the emission increments calculated for the entire grid as reported in the paper. However, they are still useful indicators for the effects of emission inversion. In addition, since we did not consider the temporal variation in the a priori emissions, the changes of the emission increments can be used to approximate the temporal variations of the a posterior emissions. It can be clearly seen that that there are obvious differences in the emission increments between the two scenarios. The emission increment is larger in the varying-site scenario than that in the fixed-site scenario for all species due to the increases of observation sites. Moreover, as indicated in Fig. S2, the changes of observation sites were shown to significantly affect the estimation of the emission trend in 2013 and 2014. Most of species showed decreasing trends in their inversed emission under the fixed-site scenario. However, under the varying-site scenario, the decreasing trends were smaller

for PM$_{2.5}$, NO$_x$ and NMVOC, and the emissions of PM$_{10}$ and CO even showed increasing trends. This is due to that the emission increments were positive over most of observation sites for these species as demonstrated in Fig.3. Thus, the increases of observation site would lead to increases of positive emission increments and higher a posteriori emissions, which may counteract the decreasing trends or even lead to an opposite trend. These results provide the evidences that the increasing trends in the total emissions of PM$_{10}$ and CO from 2013 to 2015 seen in Fig. 6 and Fig. 7 are highly likely to be a spurious trend caused by the changes of observation coverage. The weak emission changes in PM$_{2.5}$ and NO$_x$ (Fig. 6 and Fig. 7) may also be related to the changes in the number of observation sites. The SO$_2$ emission is an except that its calculated trend is larger under the varying-site scenario than that under the fixed-site scenario. This is because that the emission increment for the SO$_2$ is generally negative over the most sites, thus the increased observation sites would lead to larger decreasing trend in the inversed emissions of SO$_2$. To date, these results highlighted the significant influences of the site differences on the estimated emissions and their trends. Therefore, we recommend not to use the emission in 2013 and 2014 when analyze the trends of the emissions.

~~Table S1~~Text S3: Comparisons of model performance driven by CAQIEI with that driven by more recent bottom-up emission inventories

To obtain a better understanding of the accuracy of our inverse emission inventory, we conducted a one-year simulation of air pollution in China for year 2020 with more recent bottom-up emission inventories and compared its performance with that driven by the CAQIEI. The used bottom-up inventories in this simulation case includes the HTAPv3 (Crippa et al., 2023) inventory for the anthropogenic emissions outside China with a base year of 2018; the MEIC inventory for the anthropogenic emissions over China with a base year of 2020; the CAMS emission inventory (https://ads.atmosphere.copernicus.eu/cdsapp#!/dataset/cams-global-emission-inventories?tab=overview, last access: 19 June 2024) for the biogenic, soil and oceanic emissions; and the Global Fire Assimilation System (GFAS) (Kaiser et al., 2012) for the biomass burning emissions. Note that since the MEIC emission inventory does not include the ship, air and waste emissions. Emissions from these sectors over China were provided by the HTAPv3 emission inventory. For clarity, in following content, we name this simulation case as the MEIC-HTAPv3 based on the anthropogenic emission inventory used.

Figure S25 shows the time series of hourly concentrations of different air pollutants in China obtained from observation and simulation driven by the CAQIEI and more recent bottom-up inventories. Comparisons of the evaluation statistics of these two simulation scenarios are also presented in Table S3. It shows that updating the bottom-up emission inventories to a more recent year

does improve the model performance compared to the outdated a priori emission inventory (Table 2), suggesting that the bottom-up emission inventory has to some extent captured the changes of air pollutant emissions in China. It is also encouraging to find that the model performance driven by CAQIEI and MEIC-HTAPv3 is similar for the $PM_{2.5}$, PM_{10}, and SO_2 over the NCP, NE, SE and SW regions, both significantly improved from the a priori emission inventory. This suggest that both the top-down and recent bottom-up emission inventories have good performance in capturing the emission changes of these species over these regions and they yield consistent estimations. However, the model simulation driven by MEIC-HTAPv3 still have negative biases in the CO concentrations possibly due to the underestimations of CO emissions as we illustrated in Sect.4.3.1.3. Similarly, due to the errors in the dust emission, there are negative biases in the simulated $PM_{2.5}$ and PM_{10} concentrations over the western China driven by MEIC-HTAPv3. On the contrary, the simulated NO_2 concentrations in MEIC-HTAPv3 are higher than the observations over the NCP, NE and SE regions, which also partly contributes to the underestimated O_3 concentrations over these regions. The CAQIEI generally achieves better performance in simulating the air pollutant concentrations in China as indicated by higher values of correlation coefficient and lower values of bias and root mean square of error in the model simulation driven by CAQIEI than that driven by MEIC-HTAPv3 (Table S3).

90
91
92
93
94
95
96
97
98
99 **Table S1: Evaluation statistics for the meteorology simulation**

Region	U (m/s)			V (m/s)			T (°C)			RH (%)			Precipitation (mm/month)		
	R	MB	RMSE	R	MB	RMSE	R	MB	RMSE	R	MB	RMSE	R	MB	RMSE
NCP	0.95	0.01	0.30	0.95	-0.02	0.49	1.00	-0.42	0.84	0.95	-11.24	11.66	0.95	3.74	18.56
NE	0.94	0.37	0.51	0.89	-0.08	0.49	0.99	-1.11	2.17	0.77	-2.59	7.18	0.97	12.09	19.76
SE	0.84	-0.27	0.37	0.98	-0.37	0.80	1.00	-0.40	0.60	0.88	-7.00	7.58	0.94	37.35	61.62
SW	0.63	-0.44	0.52	0.69	0.04	0.37	0.99	1.11	1.27	0.87	-5.84	6.94	0.92	16.85	40.18
NW	0.49	-0.36	0.51	0.58	0.32	0.43	0.99	0.83	1.91	0.79	-9.49	12.06	0.51	-2.05	5.45
CENTRAL	0.95	0.10	0.41	0.70	-0.08	0.32	1.00	-0.27	0.93	0.85	-8.59	10.30	0.97	4.64	10.87

100

101 **Table S2 The average mean (standard deviation) of the calculated factor for the inflation of the ensemble member over**
102 **different regions of China for different species**

	NCP	NE	SE	SW	NW	Central
$PM_{2.5}$	1.0 (0.2)	1.7 (1.6)	1.0 (0.0)	6.8 (8.5)	3.1 (3.8)	3.9 (3.9)
PM_{10}	1.4 (0.7)	7.2 (8.0)	2.4 (0.8)	78.1 (108.2)	26.3 (36.5)	36.0 (49.0)
SO_2	1.4 (0.7)	4.1 (3.2)	2.3 (0.8)	176.1 (254.6)	7.8 (6.5)	58.6 (72.5)
NO_x	1.0 (0.1)	1.7 (0.7)	1.2 (0.3)	8.1 (5.3)	2.8 (1.3)	5.4 (4.1)
CO	1.0 (0.1)	2.8 (2.3)	1.4 (0.4)	18.8 (16.8)	6.8 (6.9)	8.6 (10.0)
NMVOC	1.4 (0.6)	4.5 (4.4)	1.6 (0.5)	8.1 (8.6)	6.5 (5.8)	8.1 (10.1)

103

104

105 **Table S3: Evaluation statistics of the model simulation driven by CAQIEI (outside brackets) and more recent bottom-up**
106 **inventories (inside brackets) in 2020**

	$PM_{2.5}$ $(\mu g/m^3)$	PM_{10} $(\mu g/m^3)$	SO_2 $(\mu g/m^3)$	NO_2 $(\mu g/m^3)$	CO (mg/m^3)	O_3 $(\mu g/m^3)$
R	0.77 (0.53)	0.73 (0.44)	0.37 (0.19)	0.69 (0.45)	0.67 (0.40)	0.75 (0.48)
MB	3.6 (5.3)	-0.3 (-14.9)	0.3 (0.7)	-0.9 (6.7)	-0.06 (-0.4)	6.3 (-13.7)
NMB (%)	10.5 (15.8)	-0.5 (-25.9)	2.6 (7.6)	-3.4 (26.2)	-8.9 (-52.7)	10.2 (-22.1)
RMSE	24.6 (34.2)	37.4 (49.1)	10.9 (13.6)	15.9 (25.1)	0.4 (0.6)	30.3 (42.3)

107
108

109
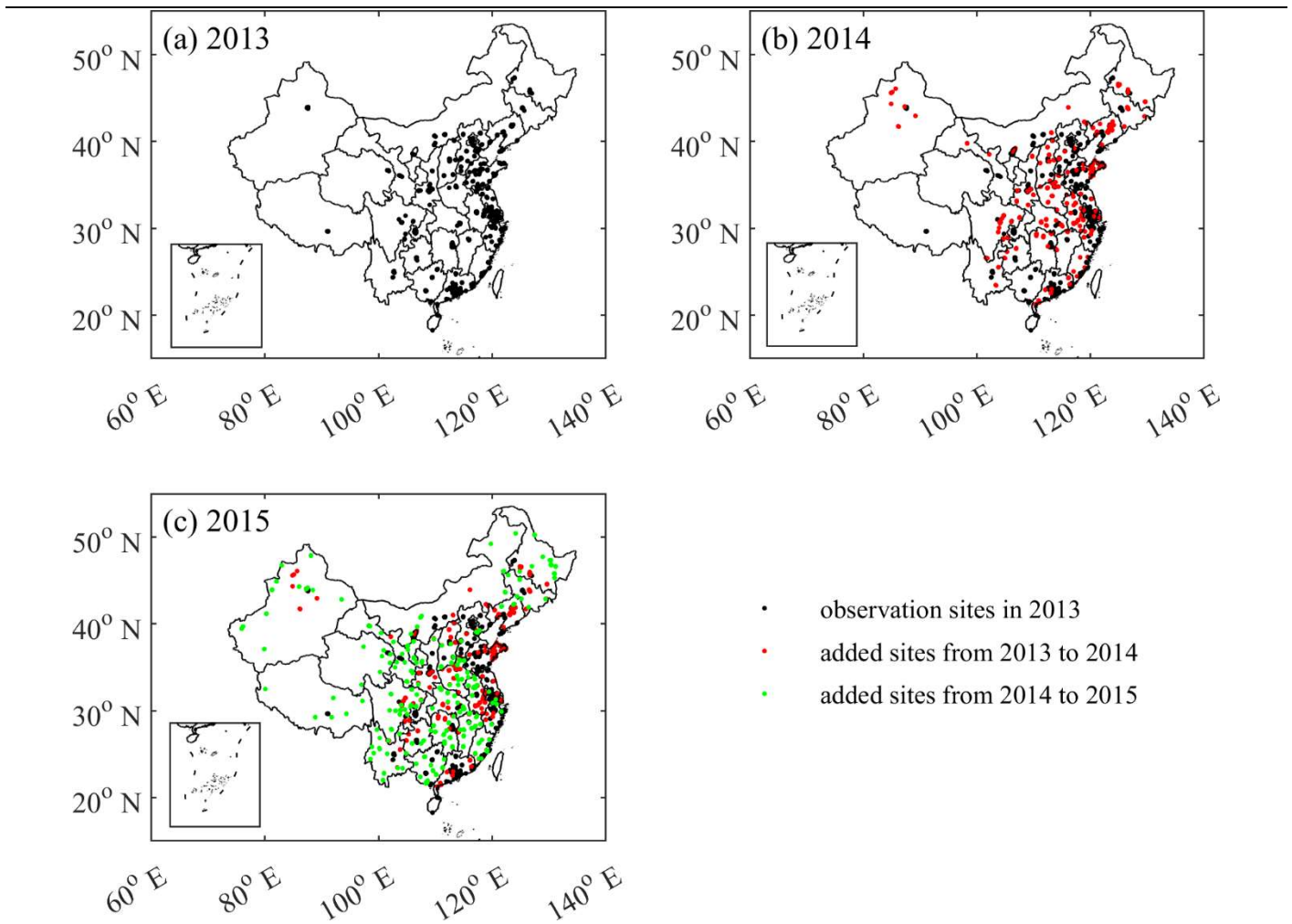
Figure S1: Spatial distributions of observation sites in (a) 2013, (b) 2014 and (c) 2015. The observation sites in 2013 were marked as black dots, while the added observation sites from 2013 to 2014 and those from 2014 to 2015 were marked as red and green dots, respectively.

112

113

114
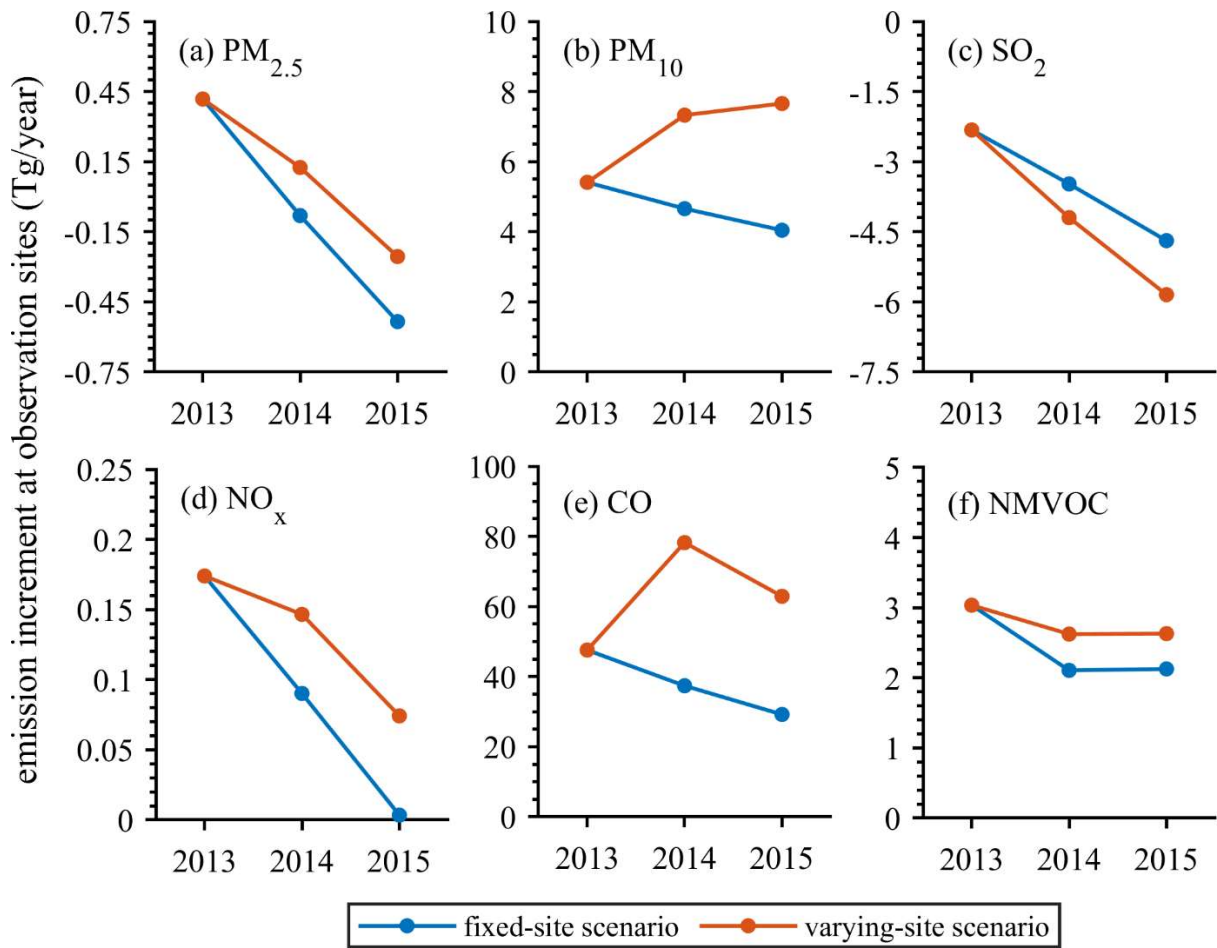
Figure S2: The calculated total emission increments at the observation sites for different species under the fixed-site scenario and varying-site scenario.

117

118

119

120

121

122

123
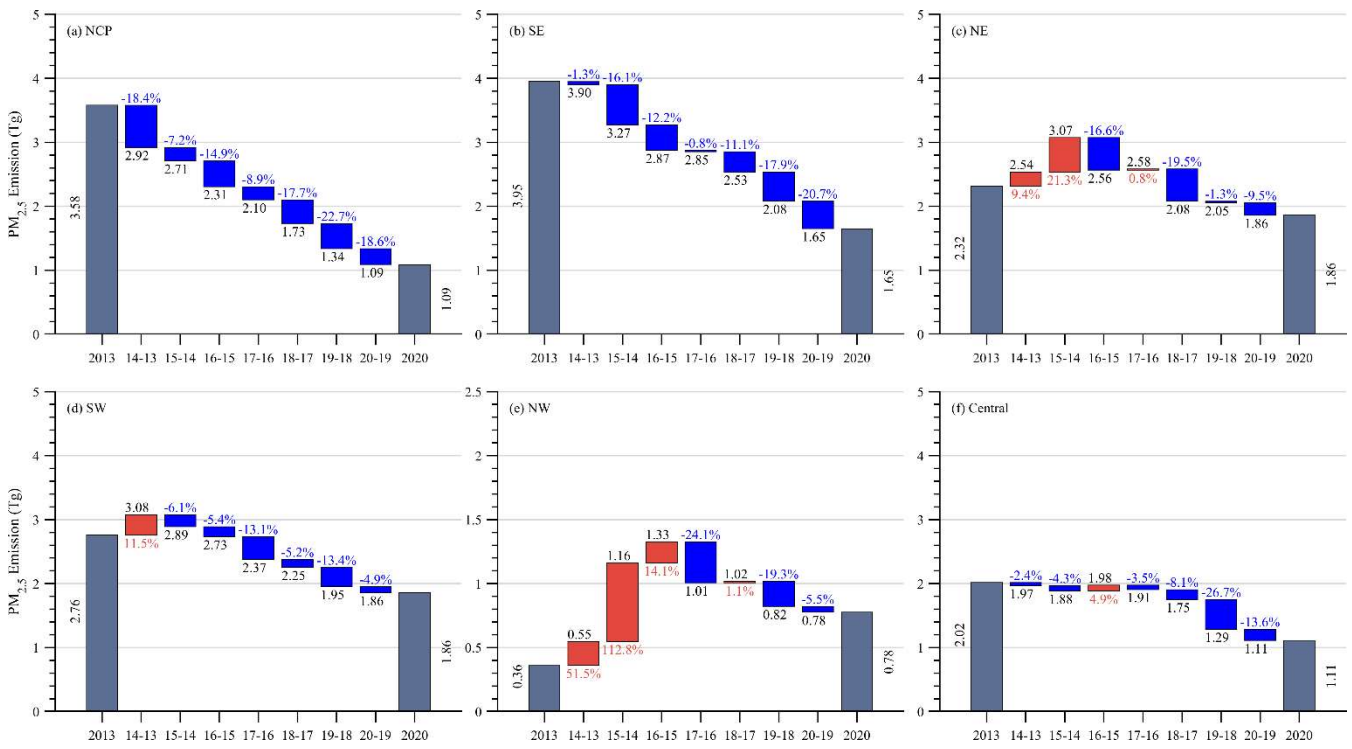
124   **Figure S3: Emission changes of PM₂.₅ from 2013 to 2020 over different regions of China obtained from CAQIEI.**

125

126
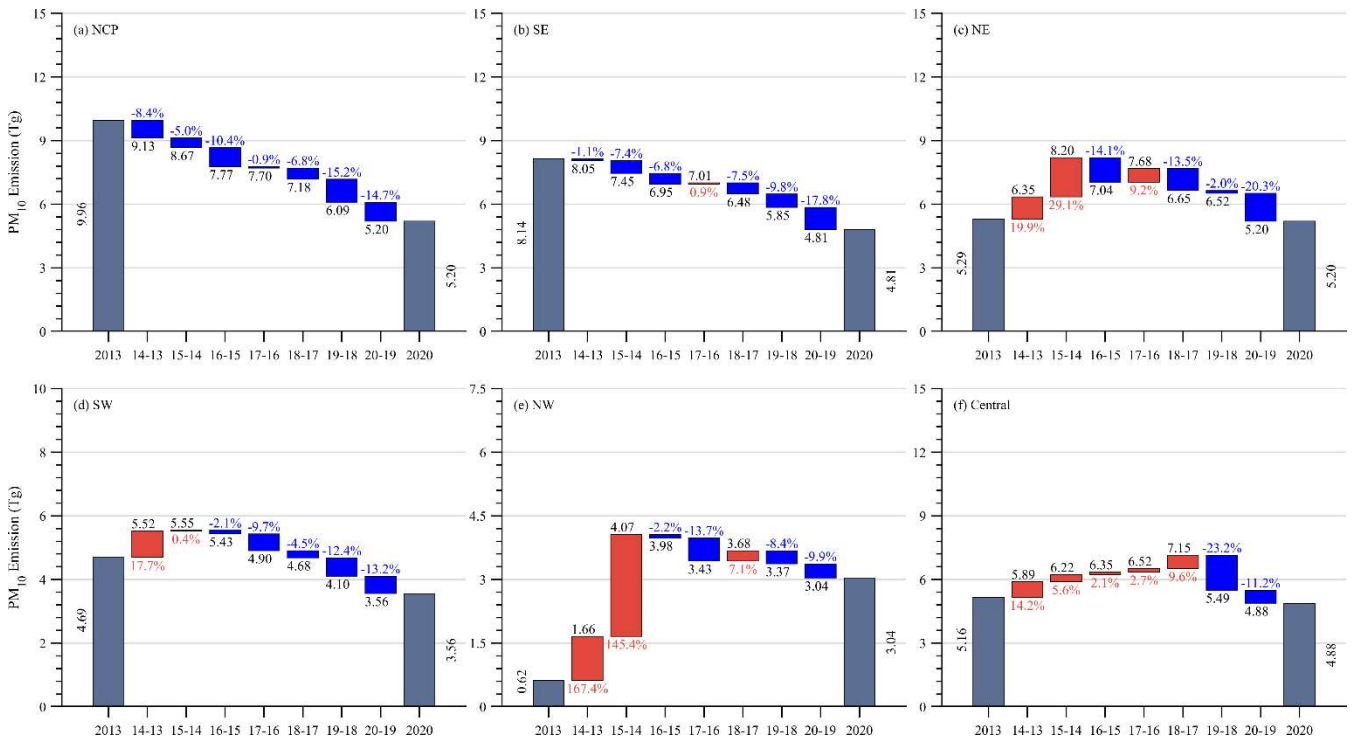
127   **Figure S4: Same as Fig. S3 but for PM₁₀.**
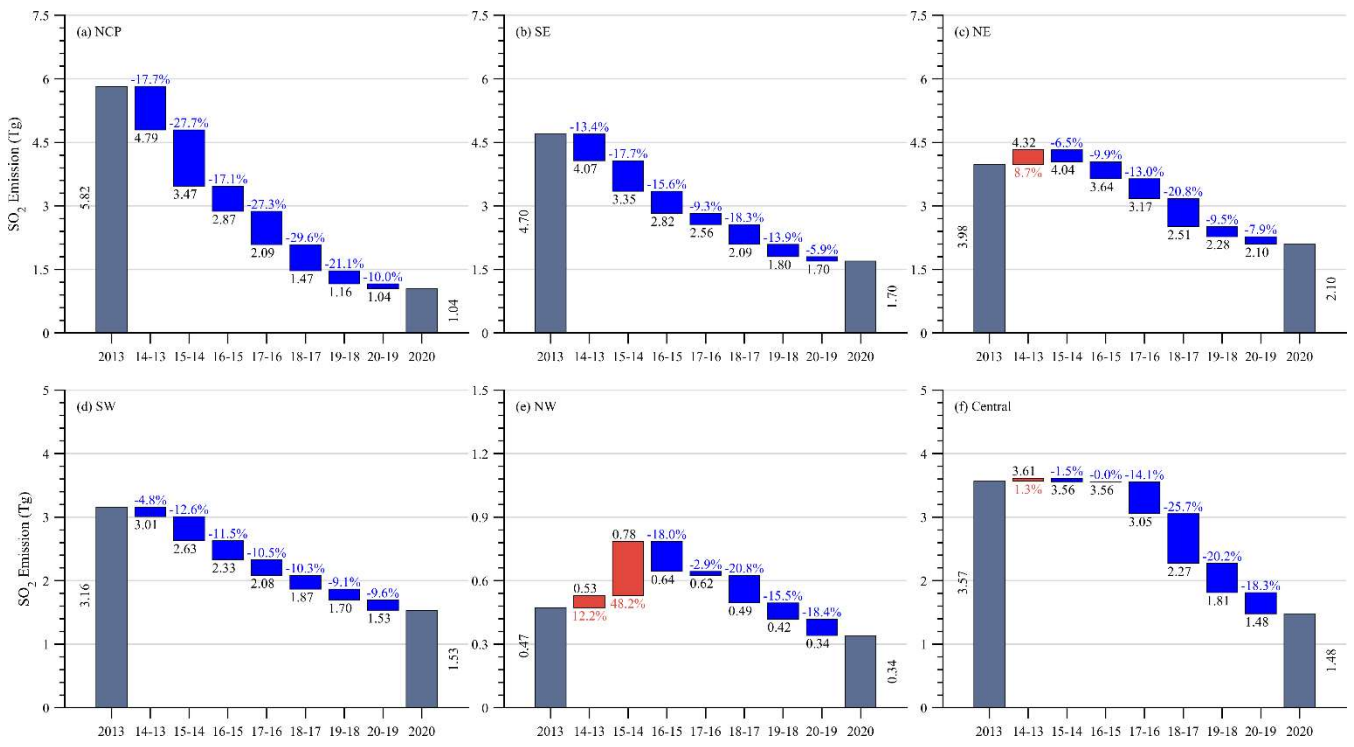
128
129 **Figure S5: Same as Fig. S3 but for SO₂.**
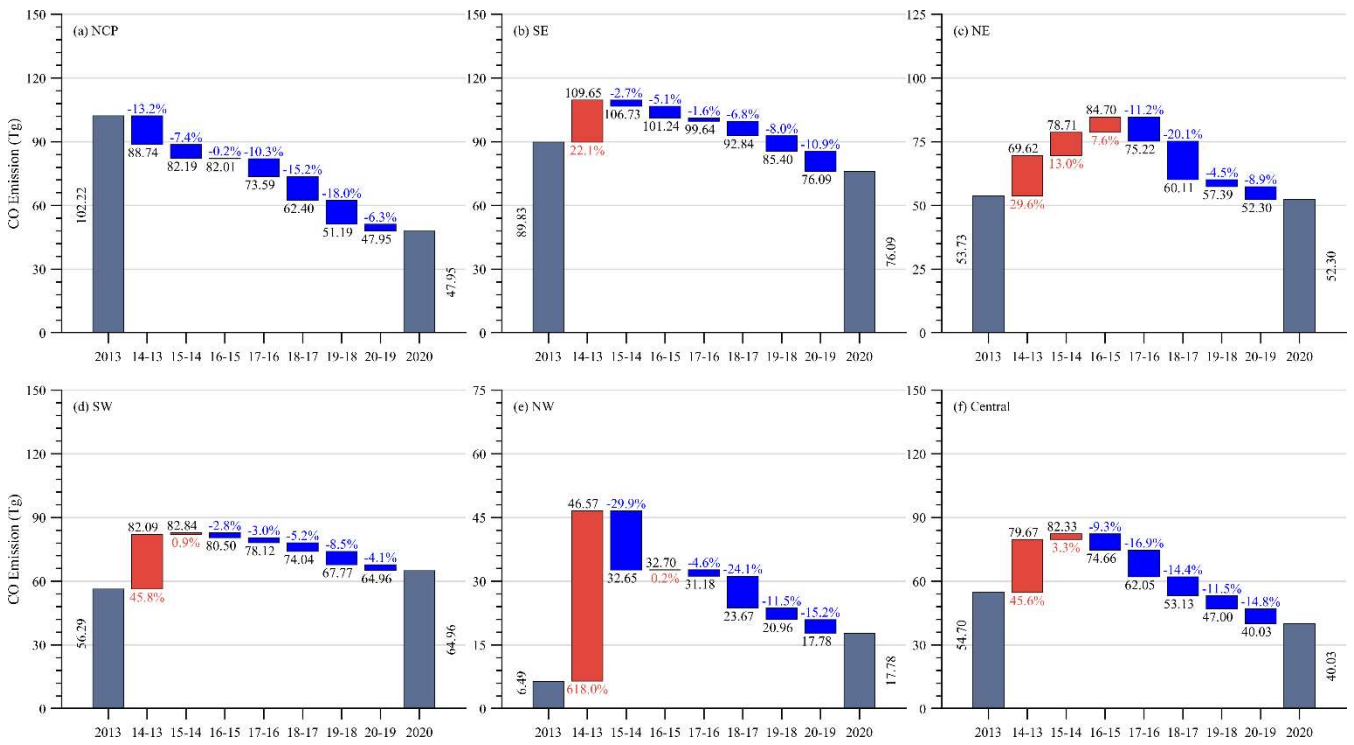
130
131 **Figure S6: Same as Fig. S3 but for CO.**

132
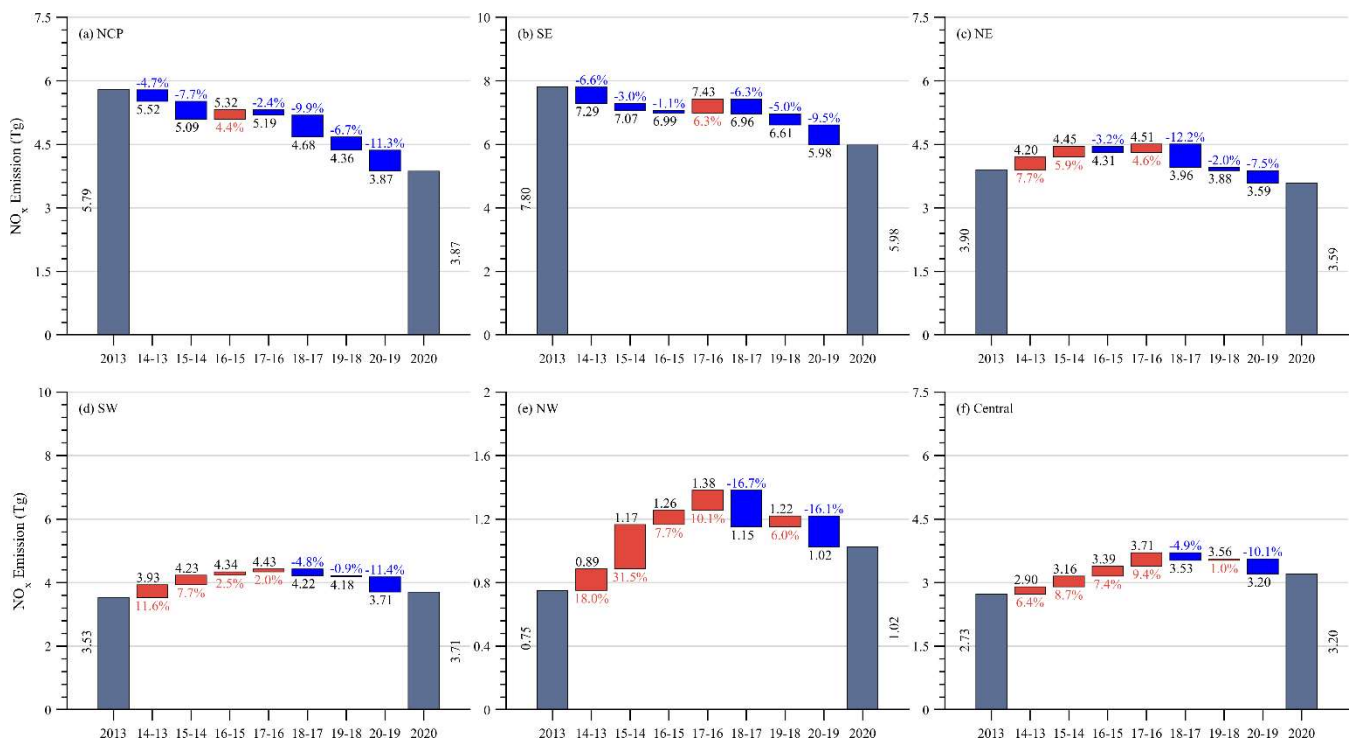
133 **Figure S7: Same as Fig. S3 but for NO_x.**

134
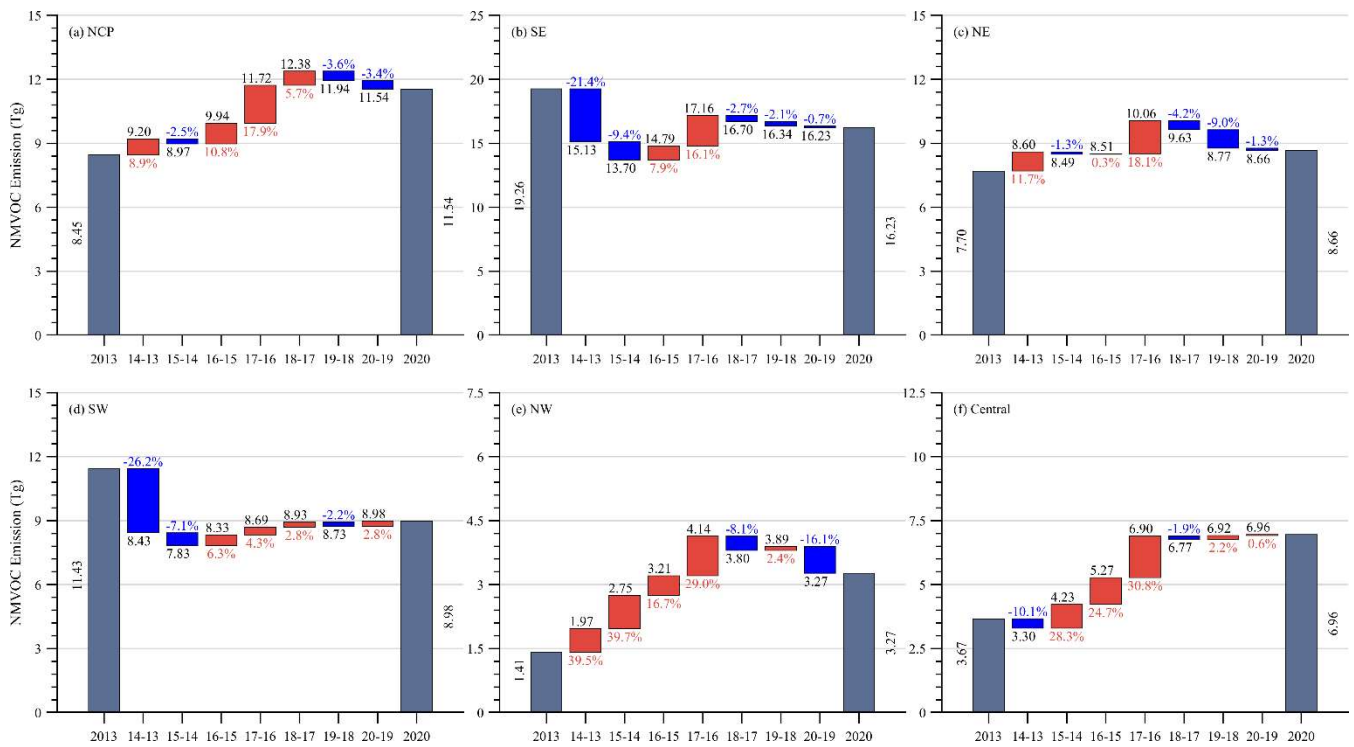
135 **Figure S8: Same as Fig. S3 but for NMVOC.**

136

137

138

139

140

141

142
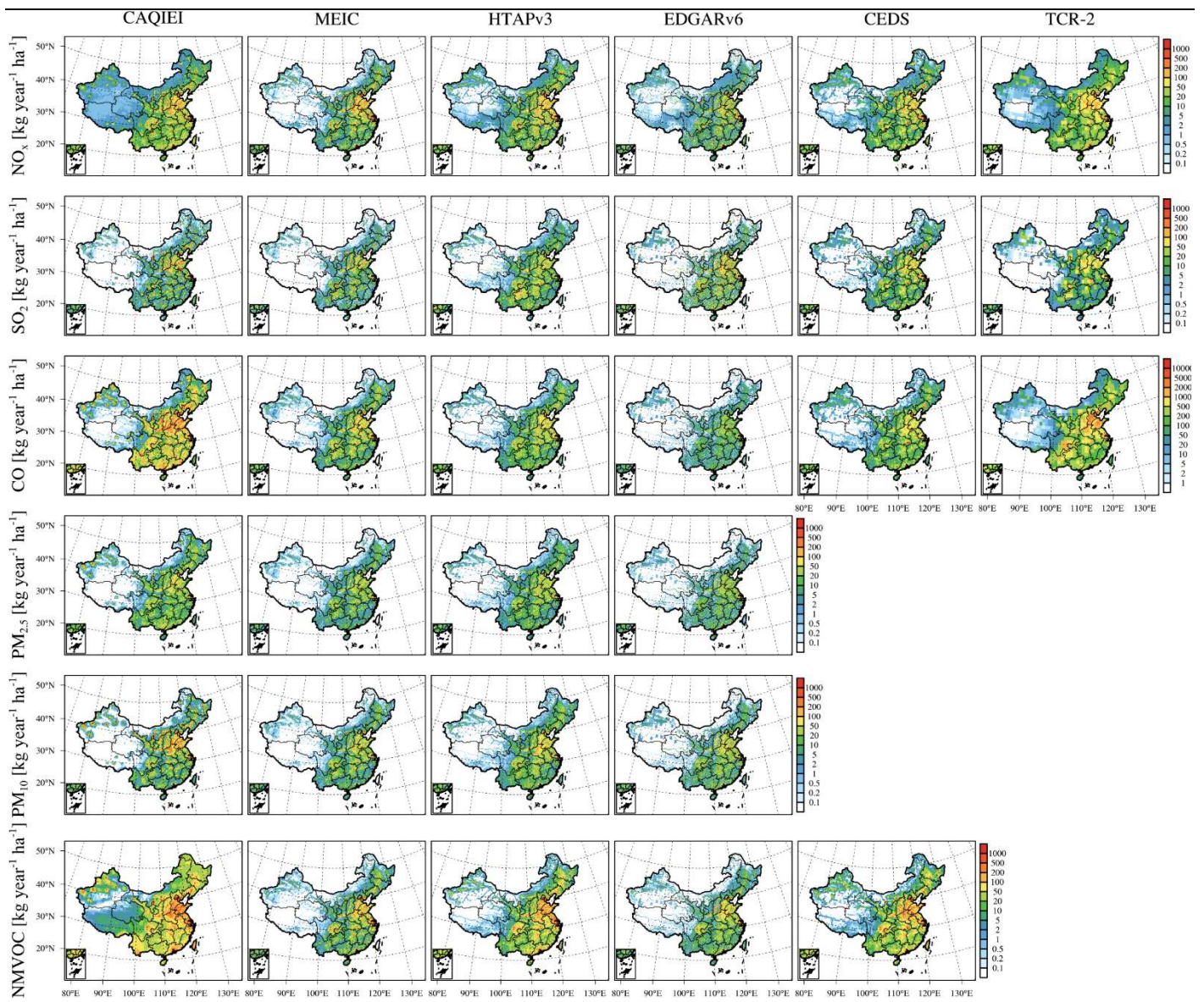
143
144 **Figure S9: Spatial distributions of the averaged emissions of different air pollutants in China during 2015–2018 obtained from CAQIEI,**

145 **MEIC, HTAPv3, EDGARv6, CEDS and TCR-2. Note the due to absence of gridded products of the ABaCAS inventory, we did not provide**

146 **its spatial distributions. Also, the natural sources were not added to the previous emission inventories in this figure because of the different**

147 **spatial resolutions among these inventories.**

148
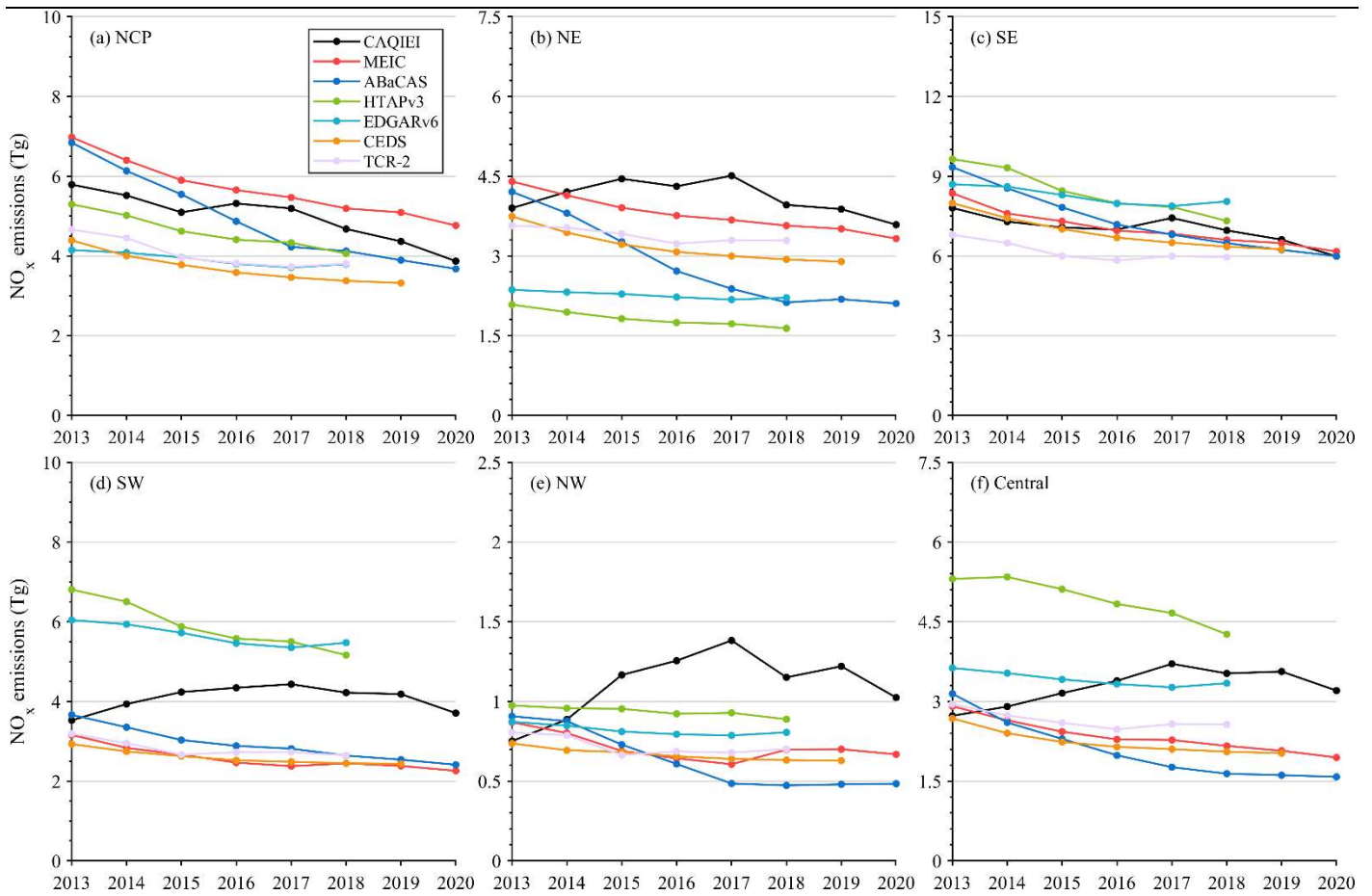
149
150 **Figure S10: Time series of annual NO$_x$ emissions over of different regions of China: (a) NCP, (b) NE, (c) SE, (d) SW, (e) NW and (f)**
151 **Central from 2013 to 2020 obtained from CAQIEI and previous inventories. Note that the natural sources were not included in the**
152 **previous inventories in this figure.**

153
154
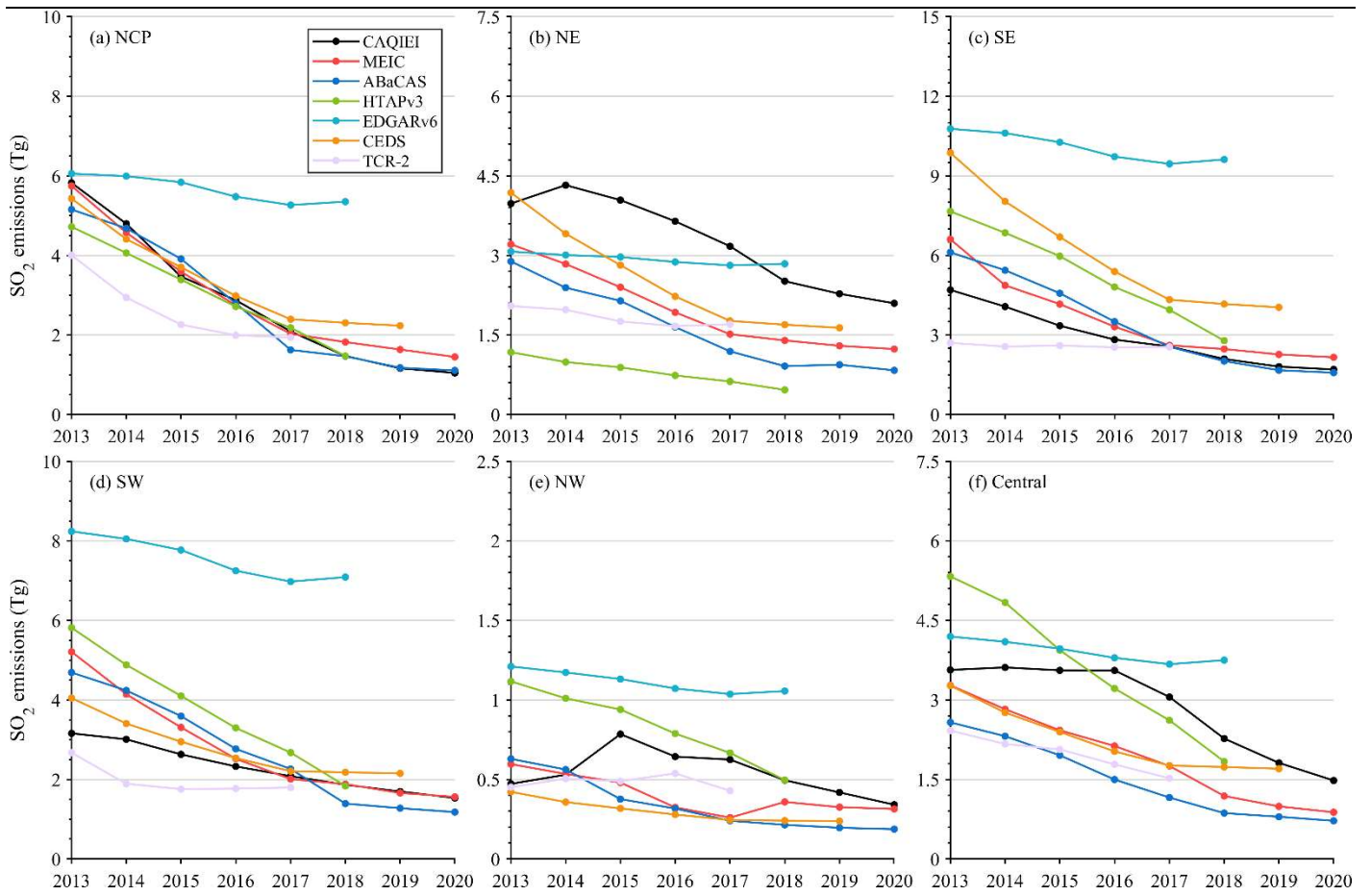
155
156   **Figure S11: Same as Fig. S10 but for SO₂.**

157
158
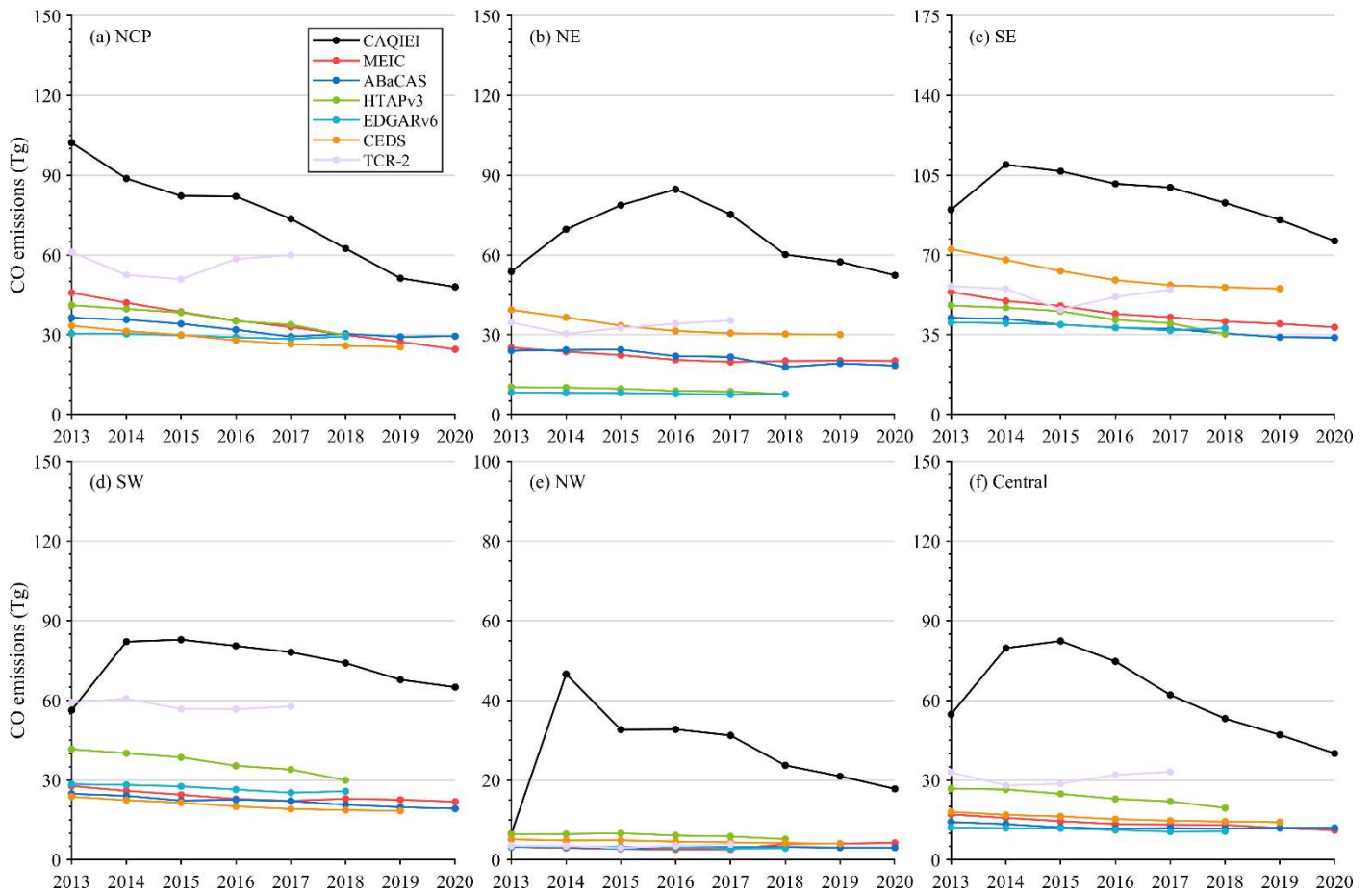
Figure S12: Same as Fig. S10 but for CO.
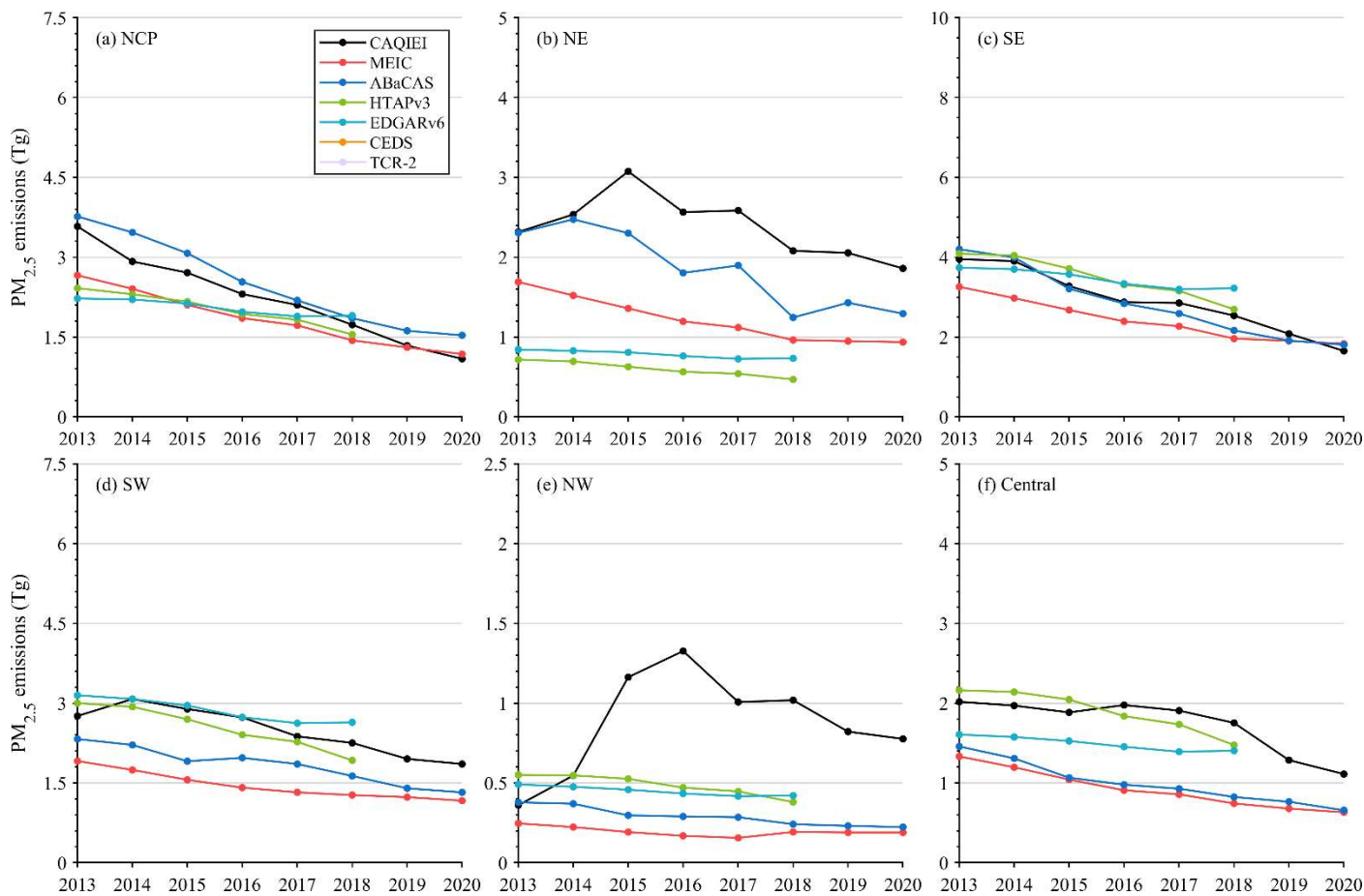
Figure S13: Same as Fig. S10 but for PM₂.₅.
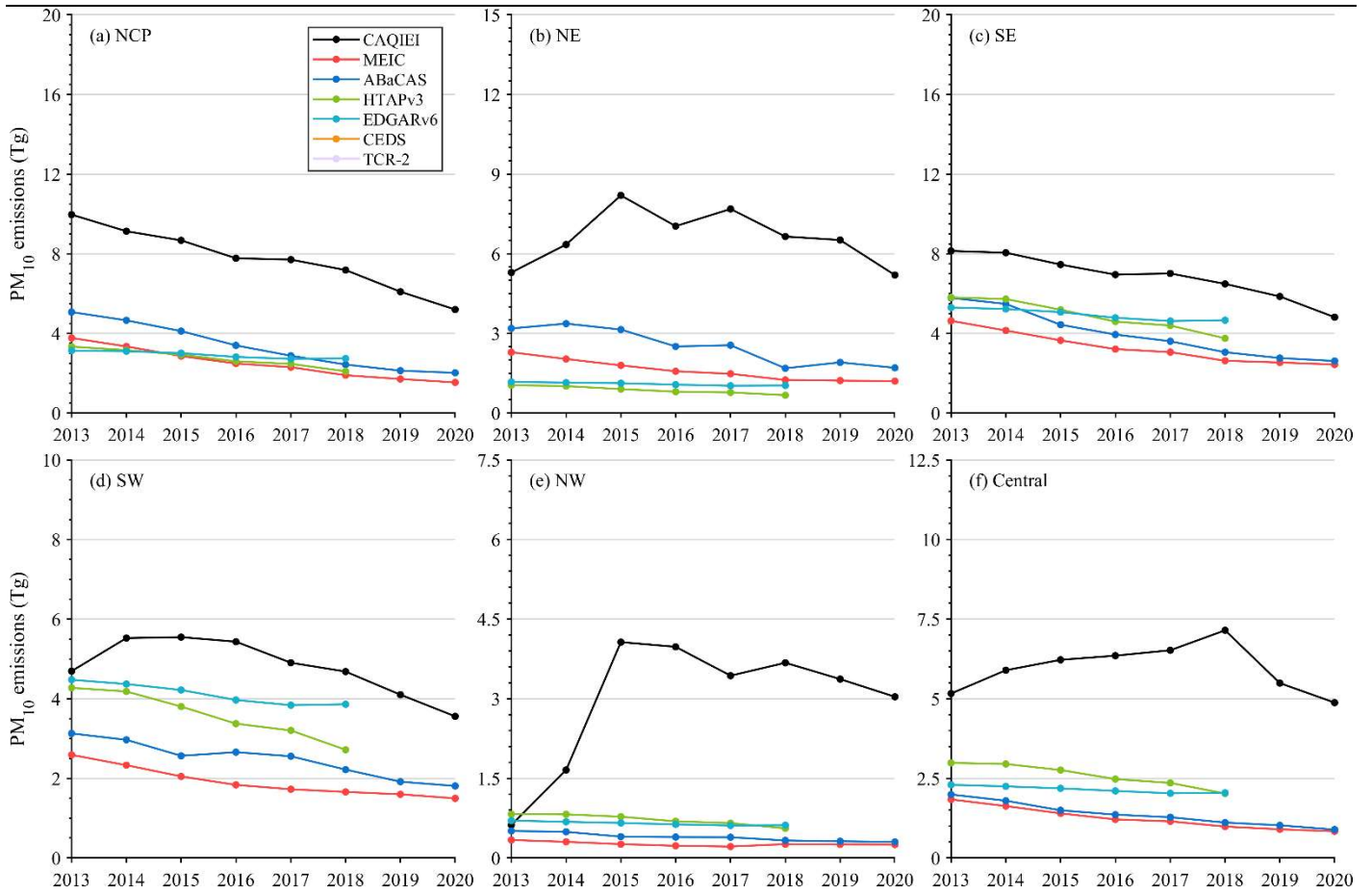
Figure S14: Same as Fig. S10 but for PM₁₀
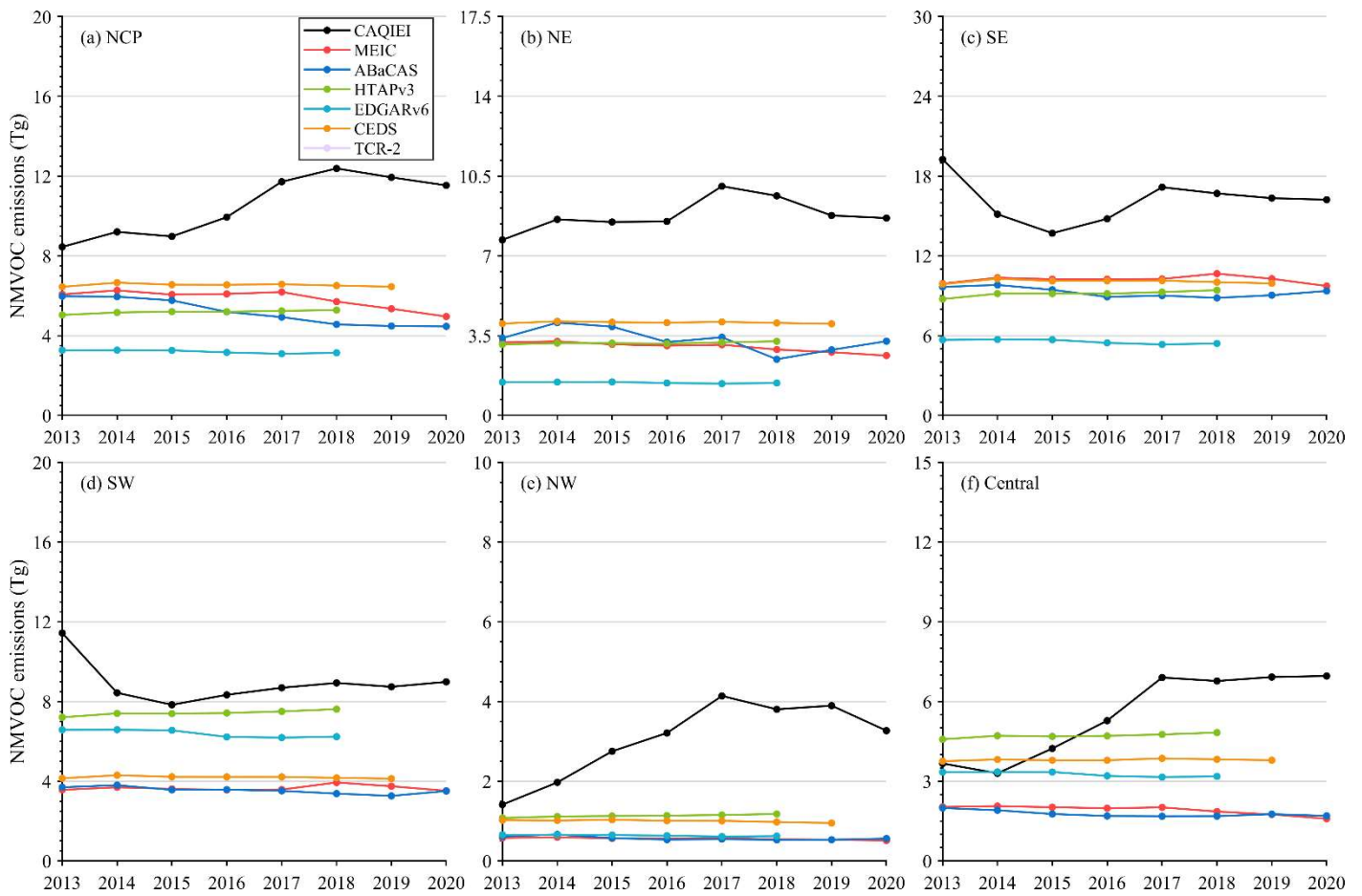
174
175 **Figure S15: Same as Fig. S10 but for NMVOC.**

176
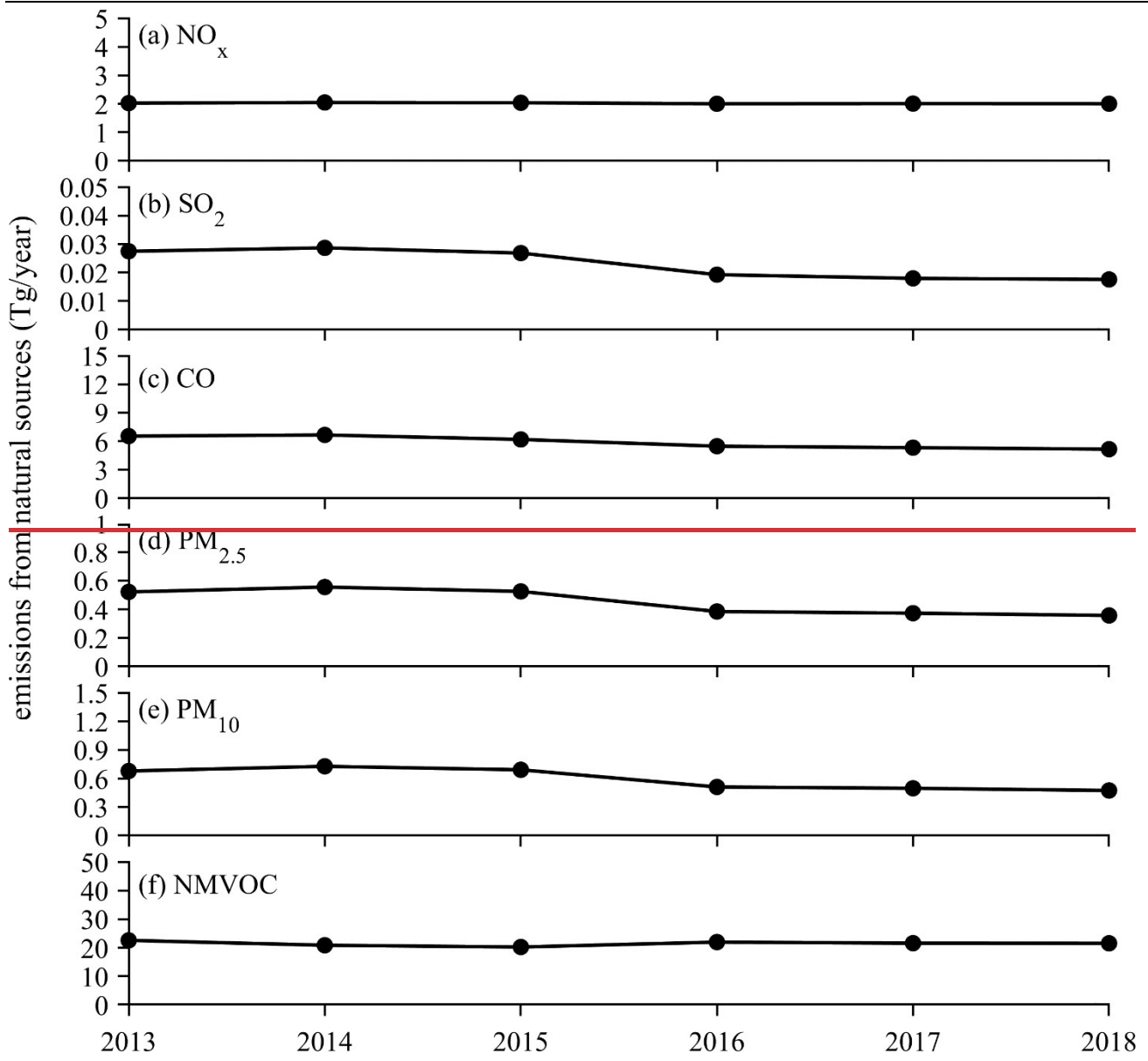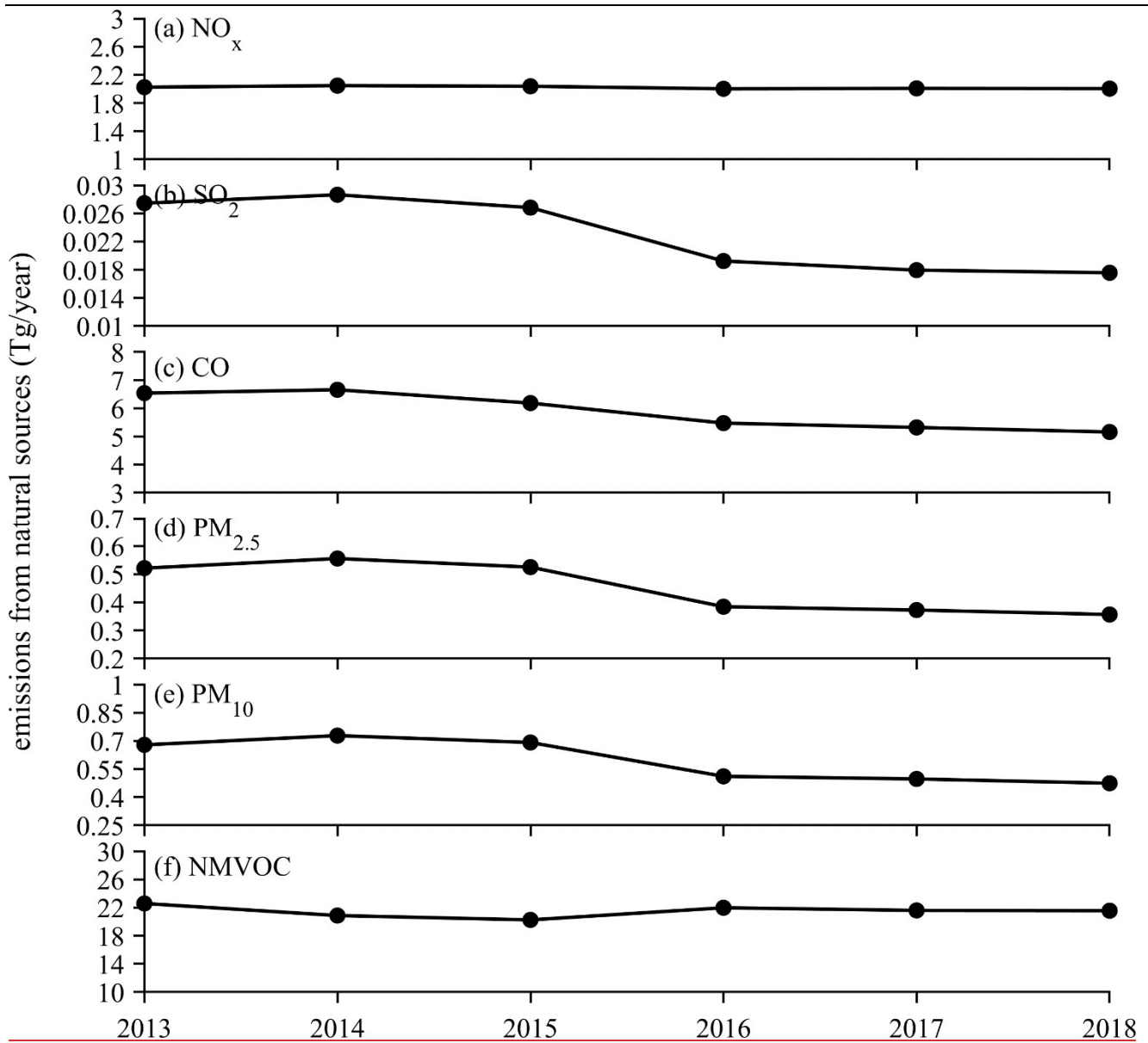
179 **Figure S16: Time series of annual natural emissions of (a) NO$_x$, (b) SO$_2$, (c) CO, (d) PM$_{2.5}$, (e) PM$_{10}$ and (f) NMVOC in China from 2013**

180 **to 2018. The considered natural sources includes the biogenic, biomass burning and soil emissions.**

178

181
182

183
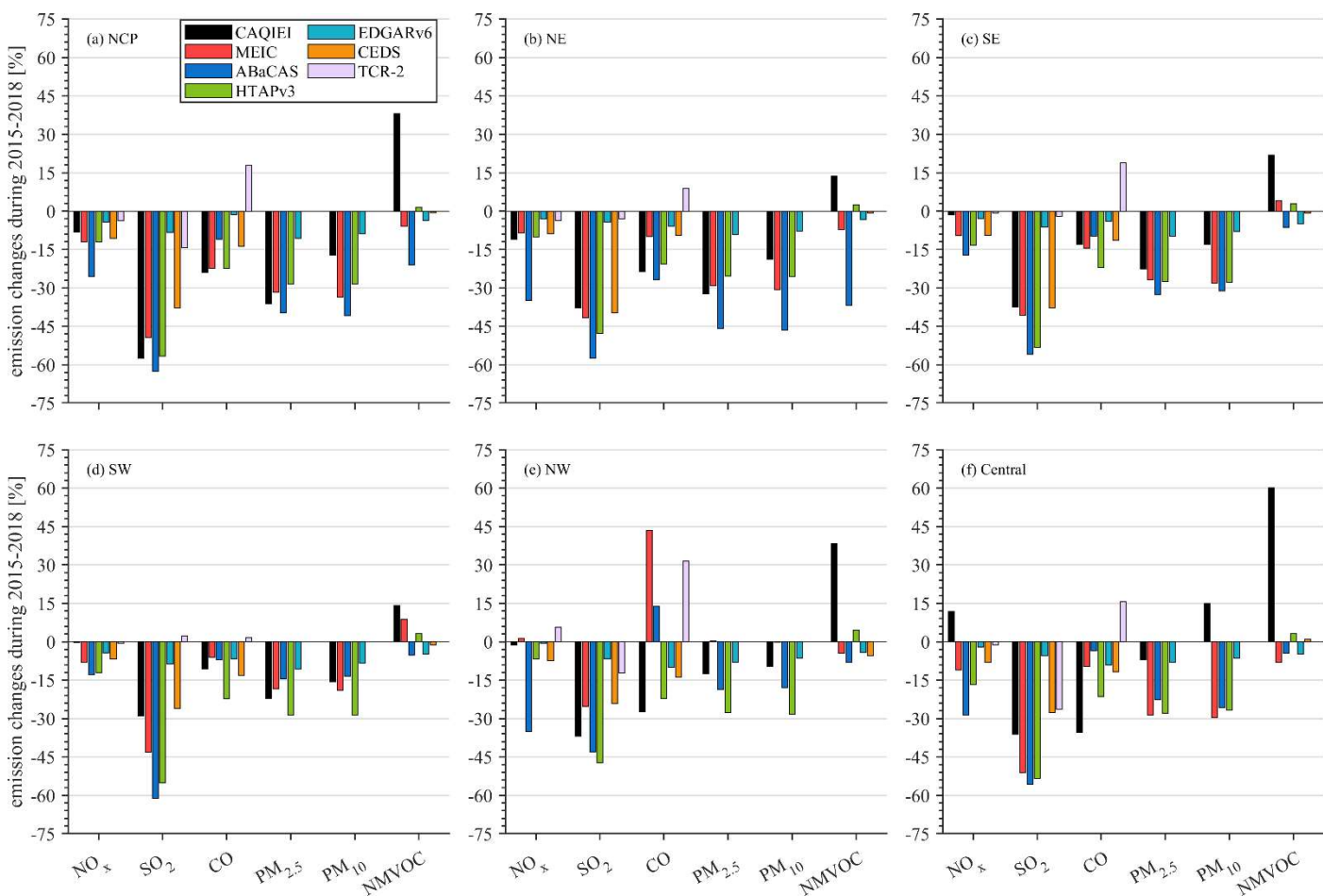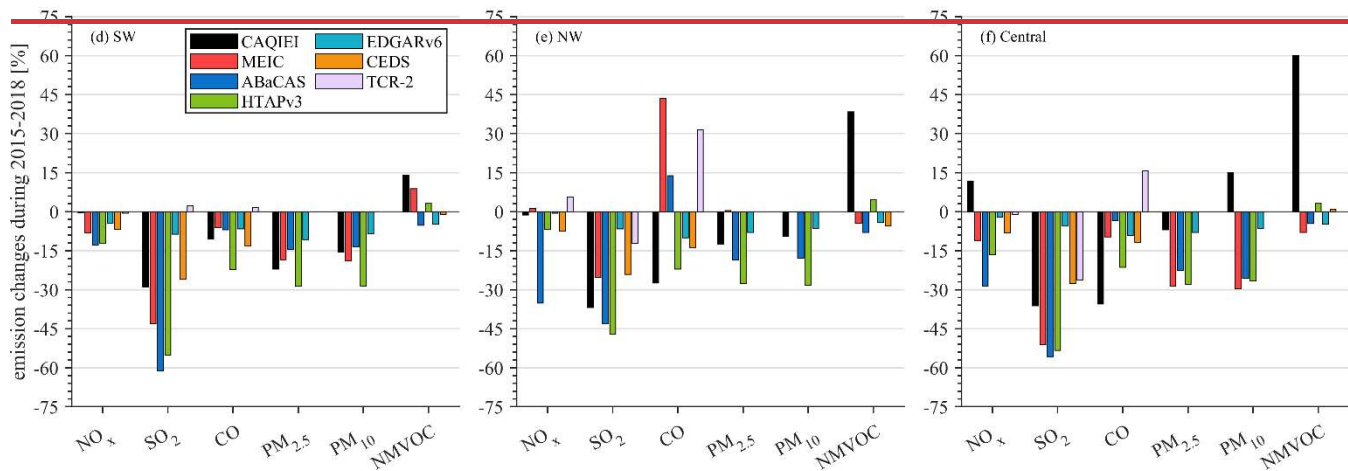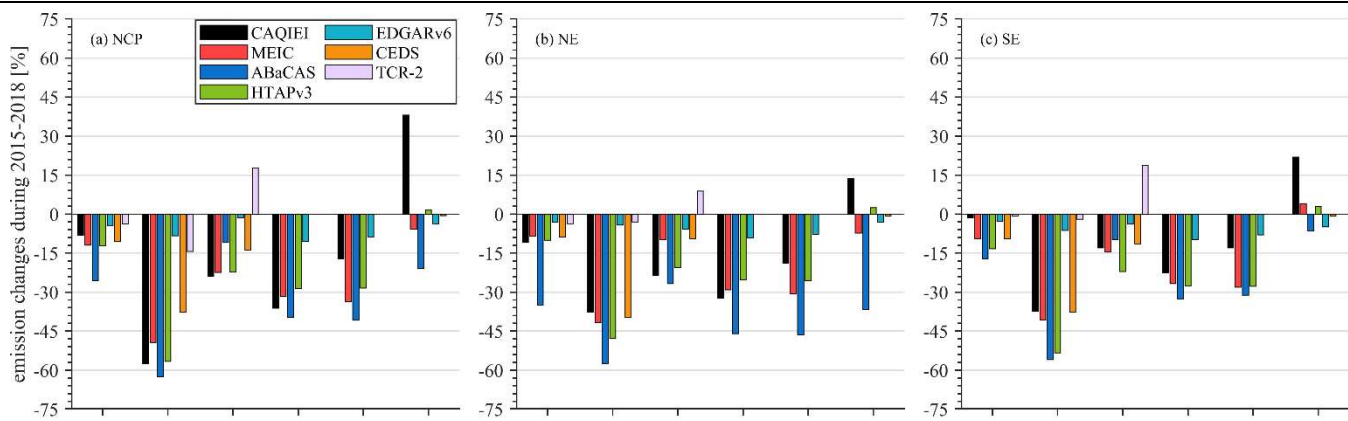
Figure S17: Comparisons of the calculated emission changes of ~~(a)~~ NOₓ, ~~(b)~~ SO₂, ~~(c)~~ CO, ~~(d)~~ PM2.5, ~~(e)~~ PM₁₀, and ~~(f)~~ NMVOCs over ~~different~~(a) NCP, (b) NE, (c) SE, (d) SW, (e) NW and (f) Central **regions of China from 2015 to 2018 between CAQIEI and previous inventories.**
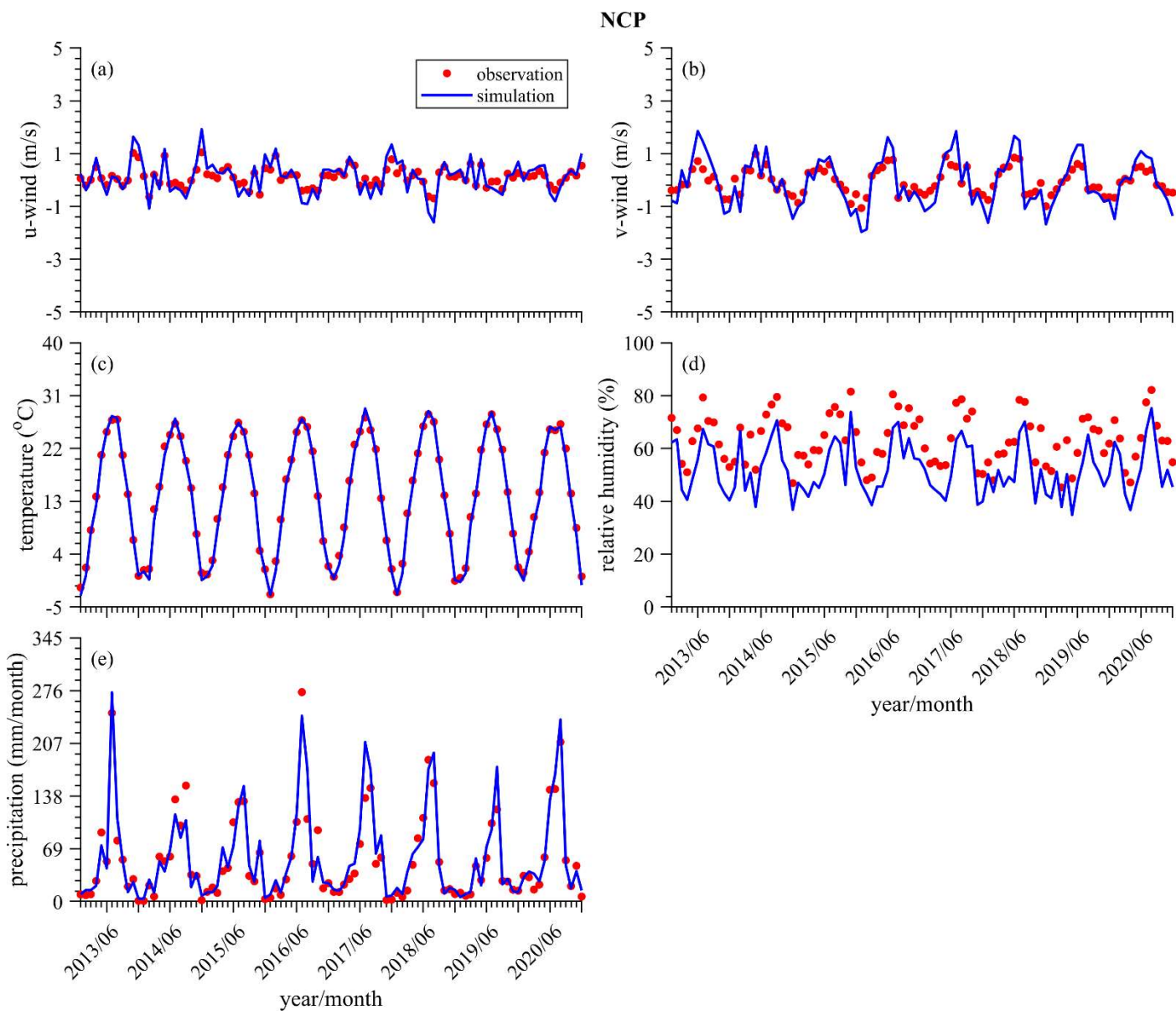
Figure S18: Timeseries of observed (red dots) and simulated (blue line) monthly values of (a) zonal wind, (b) meridional wind, (c) temperature, (d) relative humidity and (e) precipitation over NCP region from Jan 2013 to Dec 2020.
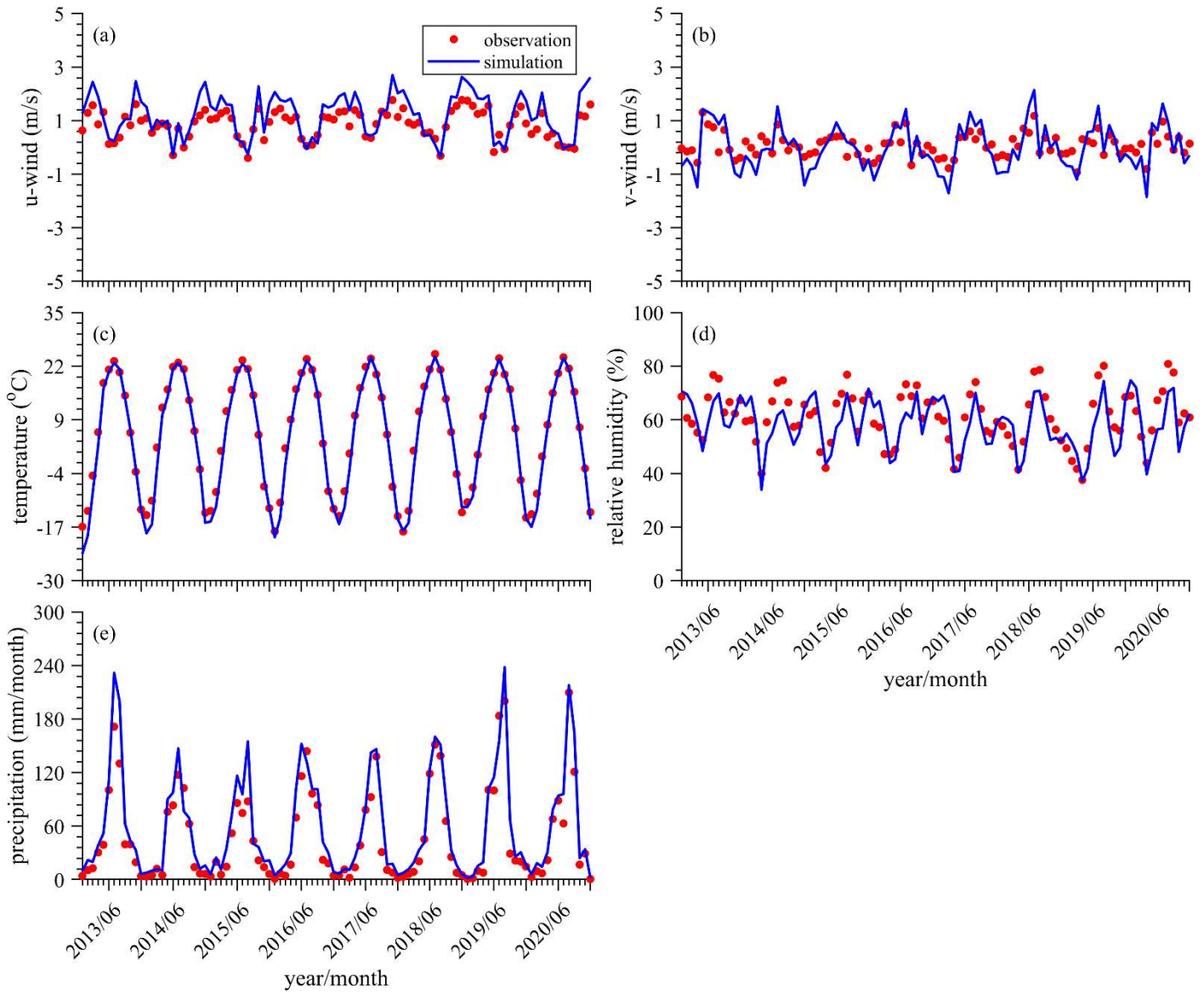
Figure S19: Same as in Figure S18 but over the NE region.

SE
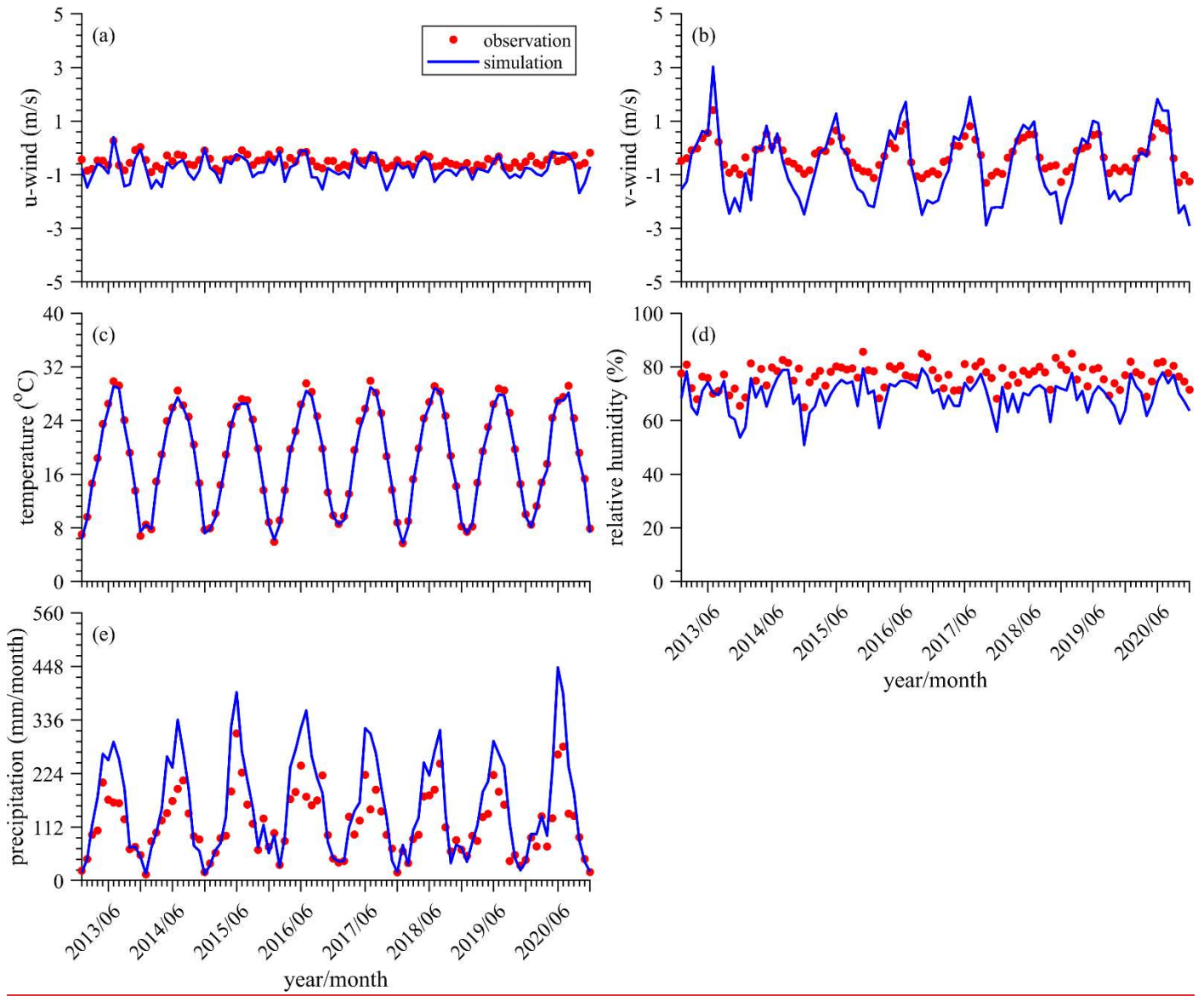
195
196 **Figure S20: Same as in Figure S18 but over the SE region.**

197

SW
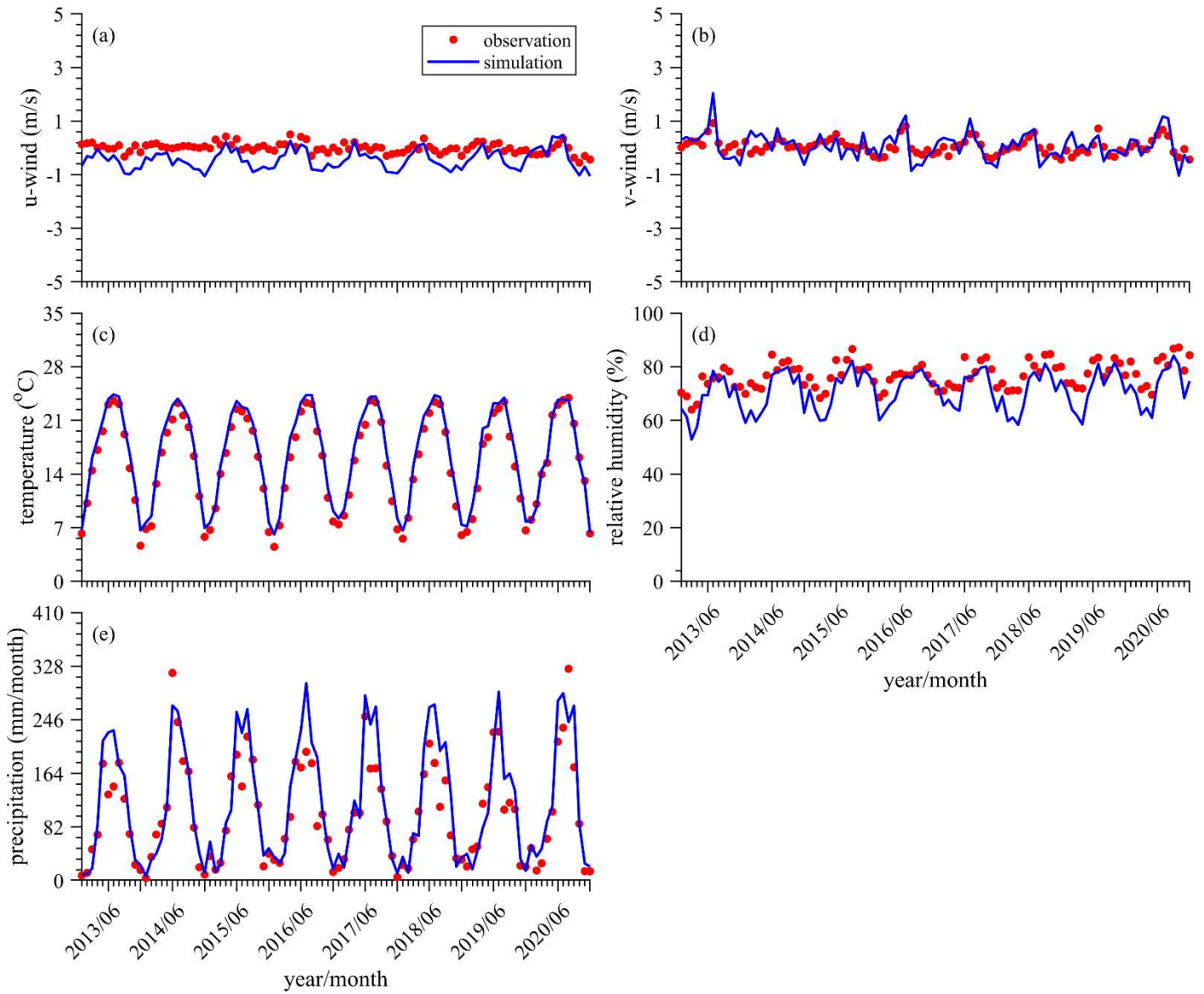
198
199 **Figure S21: Same as in Figure S18 but over the SW region.**

200
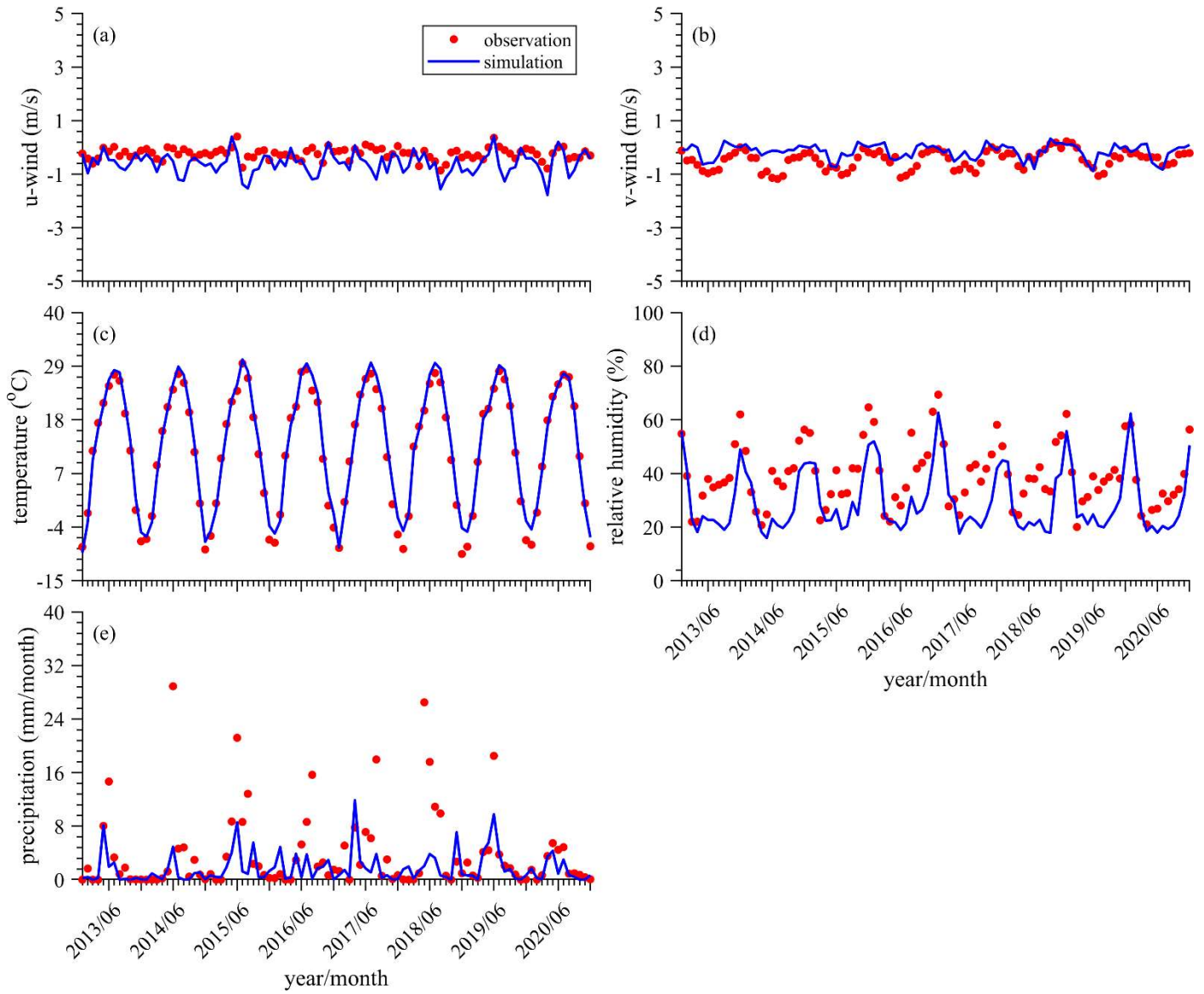
Figure S22: Same as in Figure S18 but over the NW region.
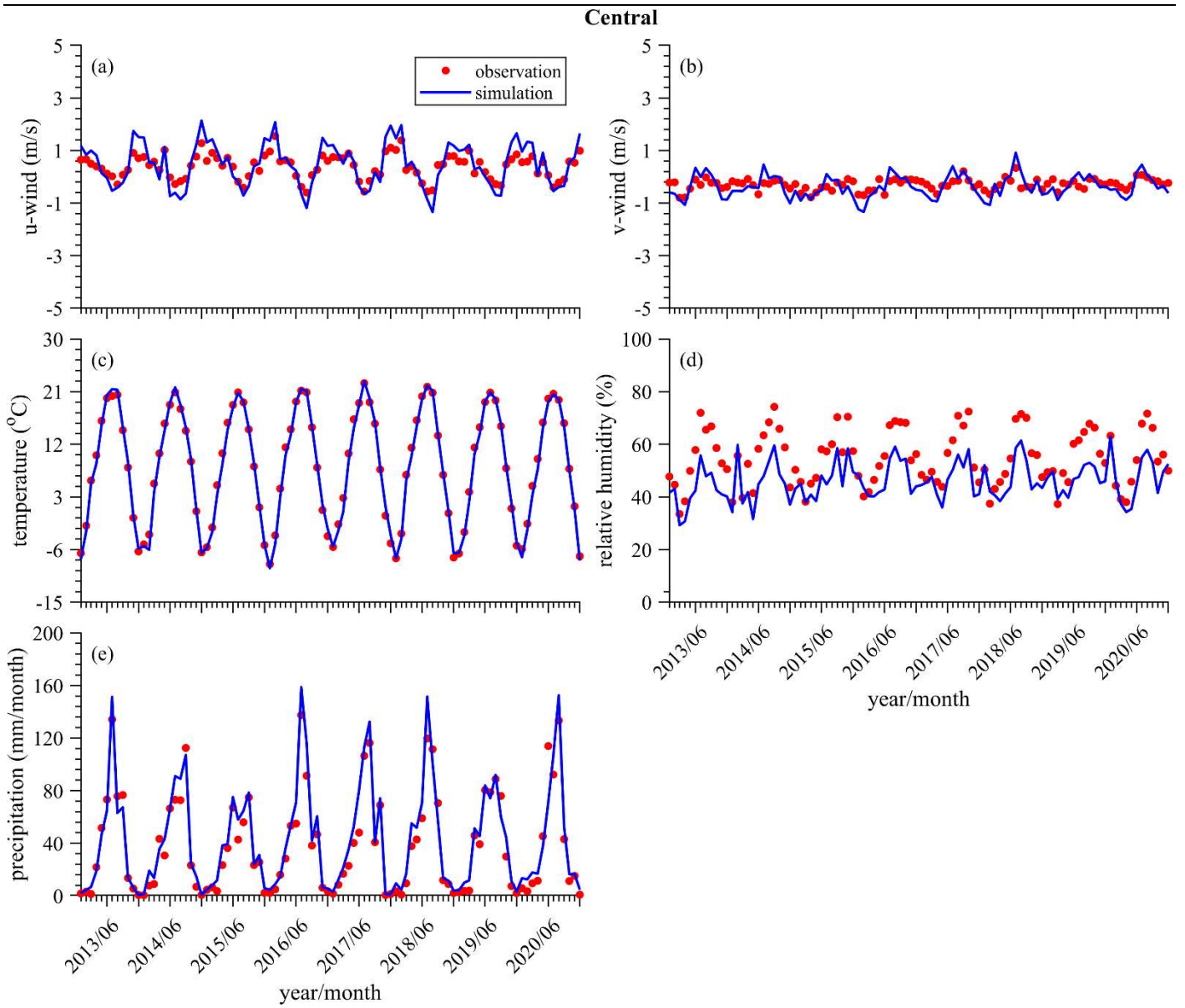
Central

Figure S23: Same as in Figure S18 but over the Central region.

207
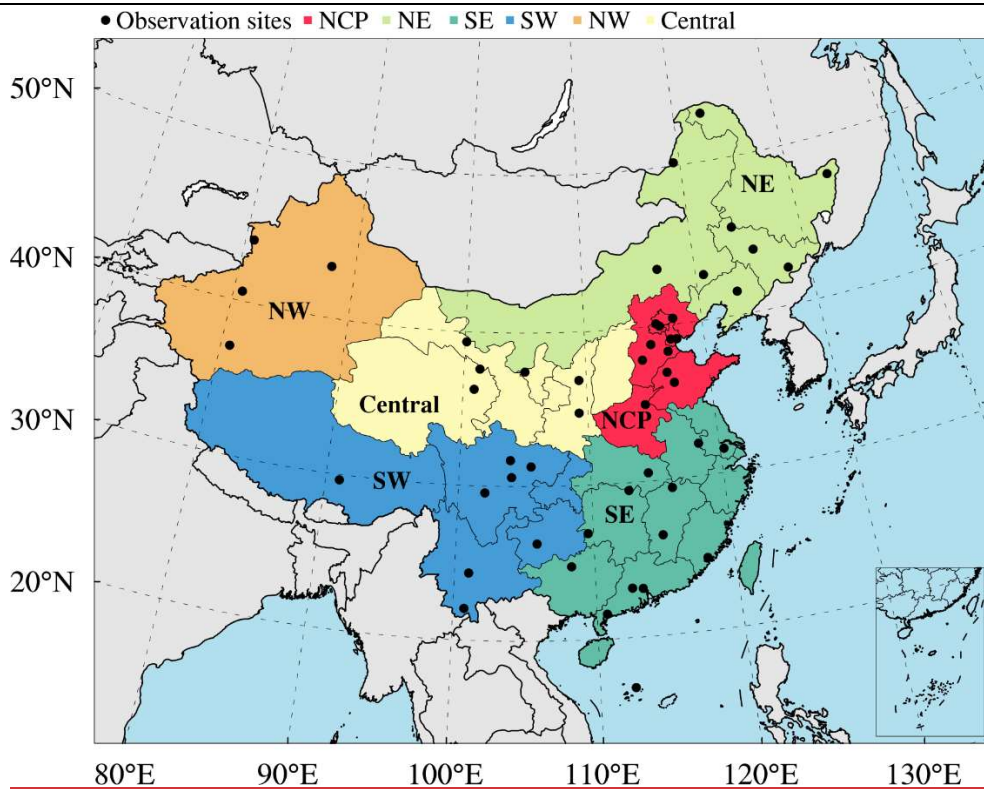
Figure S24: Spatial distribution of meteorological observation sites used in the evaluation of meteorology simulations over different regions of China

208

209

210
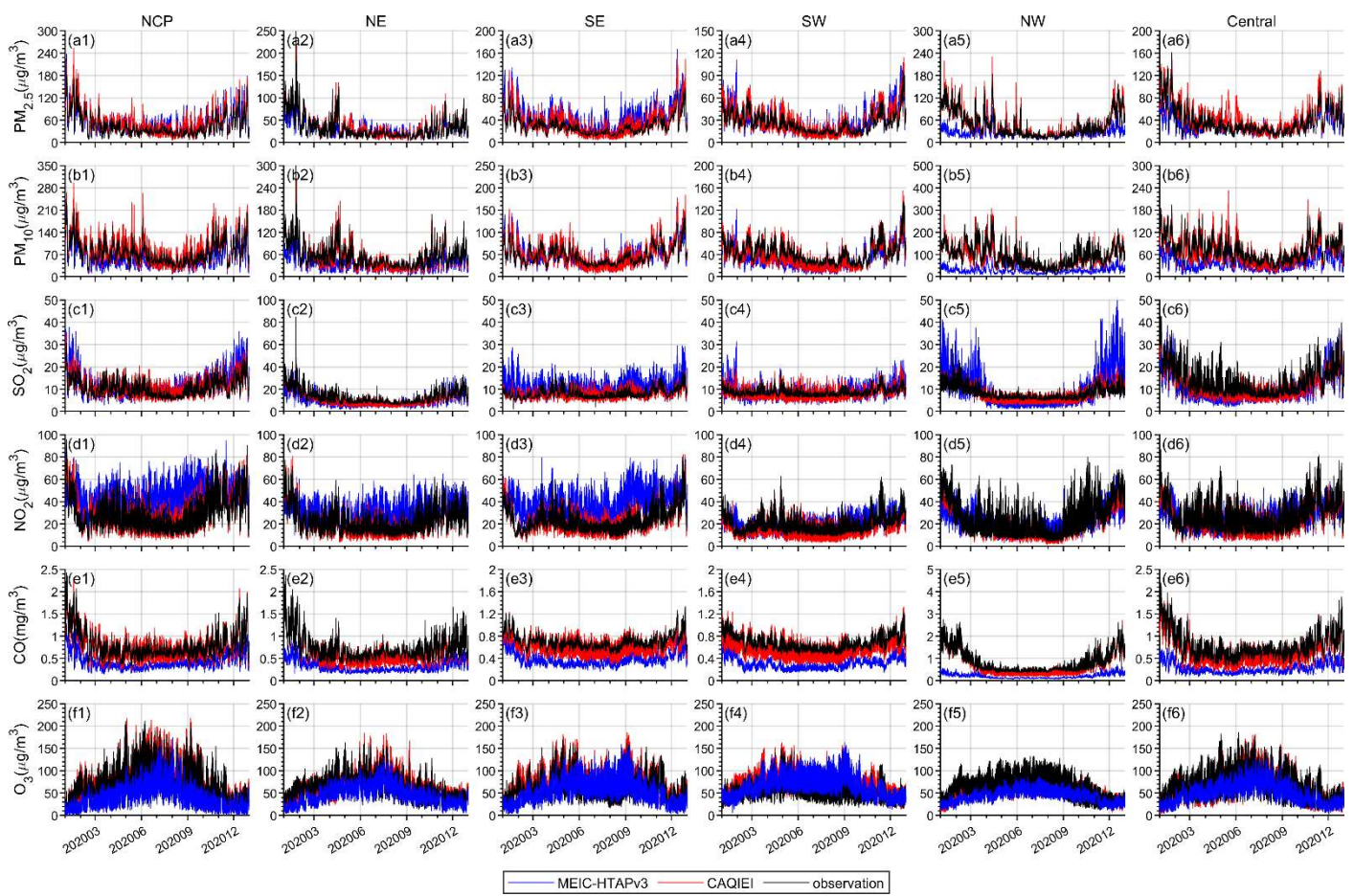
Figure S25: Timeseries of observed (black lines) and simulated concentrations of different air pollutants in China driven by CAQIEI (red lines) and MEIC-HTAPv3 (blue lines) over different regions of China.